

192 P

Damage Mechanisms and Controlled Crack Propagation in a Hot Pressed Silicon Nitride Ceramic

Anthony M. Calomino
Lewis Research Center
Cleveland, Ohio

(NASA-TM-106595) DAMAGE MECHANISMS
AND CONTROLLED CRACK PROPAGATION IN
A HOT PRESSED SILICON NITRIDE
CERAMIC Ph.D. Thesis - Northwestern
Univ., 1993 (NASA. Lewis Research
Center) 192 p

N94-34234

Unclass

G3/27 0010541

May 1994



National Aeronautics and
Space Administration

NORTHWESTERN UNIVERSITY

DAMAGE MECHANISMS AND CONTROLLED CRACK PROPAGATION
IN A HOT PRESSED SILICON NITRIDE CERAMIC

A DISSERTATION

SUBMITTED TO THE GRADUATE SCHOOL
IN PARTIAL FULFILLMENT OF THE REQUIREMENTS

for the degree

DOCTOR OF PHILOSOPHY

Field of Materials Science and Engineering

By

Anthony Martin Calomino

EVANSTON, ILLINOIS

December 1993

ABSTRACT

Damage Mechanisms and Controlled Crack Propagation in a Hot Pressed Silicon Nitride Ceramic

Anthony Martin Calomino

The subcritical growth of cracks from pre-existing flaws in ceramics can severely affect the structural reliability of a material. The ability to directly observe subcritical crack growth and rigorously analyze its influence on fracture behavior is important for an accurate assessment of material performance. A Mode I fracture specimen and loading method has been developed which permits the observation of stable, subcritical crack extension in monolithic and toughened ceramics. The test specimen and procedure has demonstrated its ability to generate and stably propagate sharp, through-thickness cracks in brittle high modulus materials. Crack growth for an aluminum oxide ceramic was observed to be continuously stable throughout testing. Conversely, the fracture behavior of a silicon nitride ceramic exhibited crack growth as a series of subcritical extensions which are interrupted by dynamic propagation. Dynamic initiation and arrest fracture resistance measurements for the silicon nitride averaged 67 and 48 J/m², respectively. The dynamic initiation event was observed to be sudden and explosive. Increments of subcritical crack growth contributed to an 40 percent increase in fracture

resistance before dynamic initiation. Subcritical crack growth visibly marked the fracture surface with an increase in surface roughness. Increments of subcritical crack growth loosen ceramic material near the fracture surface and the fracture debris is easily removed by a replication technique. Fracture debris is viewed as evidence that both crack bridging and subsurface microcracking may be some of the mechanisms contributing to the increase in fracture resistance. A Statistical Fracture Mechanics model specifically developed to address subcritical crack growth and fracture reliability is used together with a damaged zone of material at the crack tip to model experimental results. A Monte Carlo simulation of the actual experiments was used to establish a set of modeling input parameters. It was demonstrated that a single critical parameter does not characterize the conditions required for dynamic initiation. Experimental measurements for critical crack lengths, and the energy release rates exhibit significant scatter. The resulting output of the model produces good agreement with both the average values and scatter of experimental measurements.

ACKNOWLEDGEMENT

I gratefully acknowledge the contributions and support of those who made this thesis work possible. I am especially indebted to my advisors Dr. Johannes Weertman of Northwestern University and Dr. Alexander Chudnovsky of the University of Illinois at Chicago. Without their support and selfless donation of their time and advice, I would not have succeeded. Of particular importance was Dr. Chudnovsky's help in developing the guiding philosophy and structure for the study, and his patience, counsel, and encouragement during those times when the work snagged and my enthusiasm waned.

The friendship and technical support of my colleagues at the NASA Lewis Research Center and the University of Illinois are also gratefully acknowledged. David Brewer of NASA-Lewis shares equally with me in whatever credit this research and its results may warrant in future studies of brittle fracture. Dave's contributions to the development of the experimental techniques of this study were essential, and his enthusiasm and intellectual approach to the work was infectious. Equally if not more importantly, I am grateful for Dave's friendship. I am similarly indebted to Dr. Louis Ghosn of NASA-Lewis for transforming a unique idea into a useful engineering tool through his masterful analytical modeling of the experimental setup. He is a valued friend and able colleague, and I could not have succeeded without his thoughtful discussions and participation. I would like to thank the NASA Lewis Research Center for the funding, materials, and support necessary to fulfill the objectives of this program.

My supervisor, John Shannon, is especially appreciated for his personal support and interest in this work. At the University of Illinois, Michael Gorelik and Dr. Boris Kunin provided needed discussions and the interpretive model for the experimental results. Their support, too, was essential to the success of this work.

TABLE OF CONTENTS

CHAPTER I	Introduction	1
CHAPTER II	Literature Review	
	INTRODUCTION	7
	SUBCRITICAL CRACK GROWTH AND STRENGTH TESTING	
	Failure modeling	8
	Fractography and Strength Testing	17
	Fractography of Flaw Failure	18
	SUBCRITICAL CRACK GROWTH AND TOUGHNESS TESTING	33
	Inorganic Glass	34
	Polycrystalline Ceramics	35
	SUMMARY	39
CHAPTER III	Test Specimen and Procedure Development	
	INTRODUCTION	42
	STABLE CRACK EXTENSION	
	Elastic Instability	43
	Stable Crack Growth Specimens	45
	STABLE SPECIMEN DEVELOPMENT	
	Loading Configuration	48
	Stable Poisson Loaded Specimen	54
	NUMERICAL CALIBRATION	
	Model Configurations	56
	Load Transfer to Specimen	59
	Stress Intensity Factor	60
	EXPERIMENTAL EVALUATIONS	
	General Procedure	65
	Crack Length Measurements	68
	Original SPL Performance	71
	Modified SPL Performance	77
	SUMMARY	79

CHAPTER IV	Fracture Response of NC-132 Silicon Nitride	
INTRODUCTION		81
EXPERIMENTAL PROCEDURES		82
Material		82
Specimen Preparation		83
Test Procedure		83
EXPERIMENTAL RESULTS		
General Observations		88
Crack Driving Forces		90
FRACTOGRAPHY		
General Observations		96
Fracture Surface Debris		107
Fracture Surface Texture		119
SUMMARY		126
CHAPTER V	Modeling of Experimental Results	
INTRODUCTION		129
PROBABILITY THEORY FOR SUBCRITICAL CRACK GROWTH		
Single Path SFM Theory		130
Multiple Crack SFM Theory		135
Distribution Density for Arrest ERR		137
MONTE CARLO METHOD FOR SUBCRITICAL CRACK GROWTH		139
Model Development for Application of SFM		140
Modeling Parameters and Procedure		143
RESULTS AND DISCUSSION		146
CHAPTER VI	Conclusions	150
DOCUMENTATION		
References		153
Appendix A Crack Growth Kinetics		162
Appendix B Material Processing and Microstructure Information		164
Appendix C Stress Wave Interaction		169
Appendix D Replicated Fracture Surface for 3 mm Sample		171
Appendix E Effect of Interlocking Stress as Damage Zone Mechanism		175

LIST OF ILLUSTRATIONS

Chapter II

Figure 2.1	Infinite elastic solid with an imbedded crack of length $2a$ under arbitrary remote loading σ_{∞} .	11
Figure 2.2	Weibull plot displaying the failure probability for a hot pressed silicon nitride failed under pure tension and bending.	16
Figure 2.3	Graphic representation of the fracture mirror formations surrounding failure flaws observed for brittle materials.	19
Figure 2.4	Glassy carbon fracture surface showing multiple mist and hackle formations (Rice,1984A).	28
Figure 2.5	Fracture surface (MgF_2) with two flaws showing four mirror patterns A, B, C, and D (Healy,1984).	30
Figure 2.6	Log plot of failure stress versus outer mirror radius using data taken from Mecholsky (1974).	32

Chapter III

Figure 3.1	Stable crack growth specimen geometries: (a) chevron notched, (b) remote cyclic compression, and (c) single-edge precrack beam	46
Figure 3.2	Energy release rates for constant applied mouth opening force and displacement	49
Figure 3.3	Wedge opening displacement specimen with narrow geometry and curvilinear cracking, and wide geometry with rectilinear cracking.	50
Figure 3.4	Stability of wedge opening specimen showing the influence of energy stored at contact areas.	52

Chapter III (continued)

Figure 3.5	Modified Stable Poisson Loaded (SPL) specimen and loading configuration.	55
Figure 3.6	Finite Element Meshes used to analyze (a) the original SPL and (b) modified SPL specimen geometries.	57
Figure 3.7	Ratio of the load transferred to the specimen over the applied pin load (P_p/P_a) for modified SPL specimen.	59
Figure 3.8	Normalized stress intensity factors with respect to specimen force (P_p) as a function of crack length.	62
Figure 3.9	Normalized stress intensity factors with respect to CMOD (V_I) for: (a) the original, and (b) the modified SPL specimens.	63
Figure 3.10	Electrical potential drop technique for measuring crack length by sputter depositing a thin (100 Å) metallic film (chrome-nickel alloy).	70
Figure 3.11	Electron micrographs of bridged electrical contacts due to grain rotation of substrate and plastic deformation of metallic film.	72
Figure 3.12	Traveling microscope and load frame for the SPL test procedure.	73
Figure 3.13	Experimental measurement of pin load and crack mouth opening displacement versus crack length for the NC-132 material.	74
Figure 3.14	Original SPL test data revealing the measured decreasing fracture resistance produced by interface friction at the pin contact area.	75
Figure 3.15	Pin to specimen contact area showing the pin's expansion constraint for angles less than 45°.	77
Figure 3.16	Modified SPL test data revealing the minimized influence of interface friction at the pin contact area.	78

Chapter III (continued)

Figure 3.17	Optical contrast band generated on the fracture surface during increments of subcritical crack extension.	80
-------------	---	----

Chapter IV

Figure 4.1	Analog records for CMOD versus axial pin load with dashed lines displaying increments of dynamic crack growth.	84
Figure 4.2	Optical light contrast bands observed on the fracture surface for both (a) the 3 mm, and (b) 1 mm test case.	85
Figure 4.3	Comparison of optical crack length positions taken during testing to contrast band positions demonstrating the accuracy of optical tracking.	86
Figure 4.4	Calibration for generating continuous crack lengths from discrete measurements taken during testing.	87
Figure 4.5	Plot of time versus crack length for one SCG increment using digitized data records demonstrating a sharp, asymptotic, increase in velocity at dynamic initiation.	87
Figure 4.6	Plot of crack length versus CMOD for the entire test specimen taken from the digitized analog records.	91
Figure 4.7	Linear Elastic ERR evaluations taken from data given in figure 4.6. Also shown are the respective contrast bands relating to each SCG increment.	92
Figure 4.8	Plot of critical ERR at dynamic initiation and arrest with linear regression analysis results spuriously suggesting a decreasing trend in recorded values.	95

Chapter IV (continued)

Figure 4.9	Energy Release Rate (ERR) analysis using experimentally recorded critical CMOD values compared to values expected assuming constant ERR behavior.	97
Figure 4.10	Low magnification SEM micrographs of SCG increment 2 [920130_2] (a) secondary electron (SE) image, (b) SE image with specimen tilted 25°, (c) topography image of 25° tilt, and (d) YZ modulated image.	101
Figure 4.11	High magnification SEM images of fracture surface from 920130_2 showing surface texture (a) immediately after SCG initiation, (b) center of SCG increment, (c) end of SCG increment but before DCG, and (d) well after dynamic initiation.	103
Figure 4.12	Higher magnification SEM images similar to figure 4.11 (a) initiation of SCG, (b) center of SCG increment, (c) end of SCG increment but before DCG, and (d) DCG increment.	105
Figure 4.13	Transmitted light optical micrograph of acetate film taken within a SCG increment. Dark areas are ceramic debris removed during the replicating process.	108
Figure 4.14	Backscatter scanning electron micrograph of acetate film displaying the increased amount of ceramic particles obtained within regions of SCG. Note some influence of surface texture was present in this image.	108
Figure 4.15	SEM micrographs of fracture surface from a 1 mm sample taken (a) before replicating and (b) after replicating showing three areas examined at high magnification. Regions 1 and 2 are given in figures 4.16(a) through 4.16(c). Similar micrographs taken from the 3mm sample are given in Appendix D.	110

Chapter IV (continued)

Figure 4.16(a)	Fracture surface SEM micrographs taken from region 1 before and after replication exhibiting some characteristics of particles removed from the surface.	112
Figure 4.16(b)	Fracture surface SEM micrographs taken from Region 2 before and after replication.	113
Figure 4.16(c)	Fracture surface SEM micrographs taken from Region 3 before and after replication.	114
Figure 4.17	Low contrast backscatter electron images demonstrating that a portion of the ceramic debris removed from the surface involved agglomerates of many grains. Particles as large as 10 μm are observed at higher magnification in (b).	115
Figure 4.18	Digitized backscatter images used for debris particle counts and size estimations (920130_2). Image (a) was taken immediately before SCG and comparison with (b) taken immediately after shows the debris increase related with SCG.	118
Figure 4.19	Scanning laser microscope topography procedure used to obtain quantitative elevation information from fracture surface (920130_2).	121
Figure 4.20	Grey scaled topography image of fracture surface through SCG band.	122
Figure 4.21	Results from surface roughness measurements using the root mean square method and individual scan lines with a length of 50 μm . Scan lines both parallel and transverse to the direction of propagation examined.	123

Chapter V

Figure 5.1	Potential crack trajectories from point \underline{x} to \underline{X} having equal probabilities of occurrence.	131
------------	--	-----

Chapter V (continued)

Figure 5.2	Stepwise sequential failure of material in front of the crack tip meeting the failure condition $G_I(x) > 2\gamma(x)$.	132
Figure 5.3	Apparent energy release rate response normalized by the actual energy release rate for a crack tip propagating through an elastic inclusion.	136
Figure 5.4	Model of the apparent energy release rate for subcritical crack growth used in the Statistical Fracture Mechanics approach.	142
Figure 5.5	Monte Carlo simulation for increments of subcritical crack propagation leading to the overload of elastic energy required for dynamic initiation.	144
Figure 5.6	Plot of one computer <i>experiment</i> showing multiple increments of subcritical crack growth and dynamic initiation simulating experimental observations.	147

LIST OF TABLES

Chapter III

Table 3.1	Elastic Properties Assumed for Model	57
Table 3.2	Stress Intensity Factors Modified SPL Specimen	61
Table 3.3	Numerical Calibration of Modified SPL Specimen	64
Table 3.4	Curve Fits of SIF and COD for Modified SPL	66
Table 3.5	Physical Properties of Material	67
Table 3.6	Fracture Properties of NC-132	79

Chapter IV

Table 4.1	Summary of Experimental Results	89
Table 4.2	Summary of Linear Elastic Energy Release Rates	93
Table 4.3	Best-fit Energy Release Rates	98
Table 4.4	Surface Roughness Measurements	123

Chapter V

Table 5.1	Summary of Input Parameters	146
Table 5.2	Summary of Output Parameters	147

CHAPTER I

Introduction

The potential for ceramics to satisfy the requirements of structural materials for high temperature applications is the major driving force for improved methods of characterizing strength and durability. The attractive properties of most ceramics include a low density, a high material stiffness, and high strength. A leading barrier against widespread use of ceramics for structural components relates directly to the inherent brittleness of the material and its low damage tolerance. Although improved processing techniques have contributed to increases in strength, still absent for ceramic design is the reproducibility of material behavior commonly observed for most metals. The only available limiting measure for tensile strength is the fracture event which varies significantly. A central problem in structural design with ceramics is scaling the mean strength of test specimens to larger structural components. The increase in scale produces a decrease in mean strength. To make efficient use of ceramic material improvements, test scatter must be formally integrated into the design process in order to predict this scale effect. Although several failure theories have been developed to account for the inherent statistical variations in strength, it is often presumed that catastrophic failure results from a single material defect without a successive accumulation of damage or subcritical crack growth. It is proposed here that the defects within a polycrystalline ceramic evolve before catastrophic loads are reached, and that the presence of this subcritical growth influences the conditions governing catastrophic

fracture.

Selecting the appropriate method to account for test scatter and scale effect is crucial as it directly affects the reliability assessment of structural components. Observations of scale effect in strength measurements was recorded as early as the fifteenth century when Leonardo da Vinci noticed that the strength of a rope decreased with increasing length. Of course a formal treatment for scale effect was not accomplished until four hundred years later when Pierce (1921) considered similar behavior in cotton yarns and proposed that the random chance of a continuous length of yarn having a weakness increased with its length. Over a decade later Weibull (1939) extended the concept of scale effect to three dimensional solids using the maximum principle stress as the strength measure. Weibull is best known because he introduced the weakest link (WL) theory to the structural engineering community. He established the appropriate mathematical expression for the principle of the weakest link to describe size effect in solids. Later (1951) he demonstrated that his formalism worked well where, in general terms, "the occurrence of an event in any part of a body is said to be the same as the occurrence in the body as a whole." Weibull's theory was generally accepted for uniaxial stress state failures, but difficulties followed when failure resulted from more complex stress states. Attempts to modify Weibull's approach included assuming that, for polyaxial stress states, the total probability of an occurrence was the product of the individual probabilities for each positive principal stress, but discrepancies between experiment and theory persisted.

It was finally argued that WL theory was deficient because it did not address the

true nature of failure. It was known that failure in brittle solids resulted from sharp defects, and there were established procedures for handling such problems using principles from fracture mechanics. Batdorf (1974) re-formulated the WL theory using concepts from fracture mechanics. He proposed that variations in strength and size effect could be accounted for by characterizing the variations in critical flaw size. Batdorf's approach remained essentially a strength based formalism, however, now the characteristics of material defects could be dealt with separately. His treatment is limited to a population of pre-existing flaws which are assumed to be at their critical size in the unstressed material. No provision is made in his approach for the subcritical evolution of defects and the effects of growth on model predictions remain unresolved. Specific attention to both Weibull's and Batdorf's approach are given in the next section where experimental evidence supporting the suggestion that the flaws evolve under load is presented.

The main limitation of strength based WL theories is that they ignore the stress redistribution which can occur when local failure does not produce global failure. Extension of WL fracture theories to include subcritical effects are primarily accomplished through computer modeling, but the governing conditions for crack extension and stress redistribution are not well established. Nearly coincident with Batdorf's development, Chudnovsky (1973) introduced a Statistical Fracture Mechanics (SFM) model which specifically addressed the physics of solid failure when, in similar terms used by Weibull, the occurrence of an event in any part of a body is not the same as the occurrence in the whole body. He accomplished this by formulating the

theoretical conditions for global failure in terms of the available fracture energy along the numerous fracture paths available for extension. It is proposed that the realized fracture surface energy along each potential path will follow the same minimal distribution used by Weibull. The concept of a crack propagator is introduced as the main building block for estimating failure probabilities together with specific parameters that directly relate to material microstructure. Detailed discussion of the SFM theory is given in the section devoted to modeling the experimental results of this research. The SFM approach has lead to a new failure theory which provides the physical foundation necessary to assess the influence of subcritical failure prior to catastrophic (dynamic) crack extension.

The deficiency of a generally applicable failure theory for fracture may indicate that available weakest link theories do not accurately model the realities of ceramic failure. Due to a low damage tolerance, crack propagation in ceramics is very sensitive to microstructural fluctuations, yet most failure theories treat the material as homogeneous. Nearly every feature of material microstructure influences strength measurements including grain size (Rice, Frieman and Becher,1981; Claussen,1975; Faber,1983) inclusions (Evans,1974) and porosity (Godfrey,1973; Shetty,1983). Crack extension is a discontinuous, non-coplanar, direction-changing process and the effects of each must be addressed in existing models for accurate failure predictions (Boulet,1988).

The fracture resistance of a ceramic is greatly influenced by the size of the crack relative to the dominate size of the microstructure (Wiederhorn,1983), and it is generally accepted that the events leading to fracture occur at a scale commensurate with dominate

microstructural features. At this scale, material heterogeneity is significant and the microstructure can be no longer viewed as homogeneous. Instead it is a highly redundant structure of interlocked grains, and as a result, it is unlikely that the number of interlocked grains required to cause fracture will reach their full load bearing capacity simultaneously. It is almost natural to assume that failure occurs after an accumulation of 'subcritical' events which produces a redistribution of stresses as weaker and critically stressed grains fail and less stressed grains acquire more load. Load redistribution will give rise to an evolution of cracks from failure nucleating flaws. The appropriate failure theory for brittle fracture must include the possibility that subcritical crack evolution will occur. Ideally, development of a fracture model must follow the behavior of the material. Unfortunately, the physics for crack initiation, coalescence, stress interaction and subcritical propagation is not included in most stress based fast fracture models.

A partial reason subcritical processes have not been considered results from the limitations of current experimental techniques. Very few provide the experimentalist the opportunity to observe the starting details of the fracture event. Such test procedures provide researchers an invaluable means of identifying the important microstructural mechanisms involved and the insight necessary for developing fracture models. The first major subject of this research is the development of a test procedure which can be used to examine in detail the process of crack growth and instability in polycrystalline ceramics. A crack growth specimen, termed the Stable Poisson Loaded (SPL) specimen, has demonstrated its unique ability to initiate sharp through-thickness cracks in ceramic plates and propagate these cracks in a controlled and stable manner. The SPL fracture

specimen, its supporting stress analysis, and test procedure were created to provide a means of quantitatively investigating the fracture response of very brittle, high modulus materials. Prior to the development of the SPL specimen, the ability to study subcritical crack growth in these materials was severely limited. Other available specimen geometries and testing techniques for fracture studies were considered too restrictive. They either could not provide direct observation of the fracture process, or lacked the rigorous analytical treatment needed for model development.

The second major topic discussed in this research is application of the SPL specimen to study the fracture behavior of a common monolithic ceramic considered representative of the ceramic materials which may be used for advanced engine technology. The material selected was Norton Corporations NC-132 silicon nitride. This is a commercially available, hot, isostatically pressed silicon nitride material which has been tested extensively in the past decade. The results generated from these studies reveal that NC-132 possess a fracture response which heretofore has not been reported in the literature. These studies will demonstrate the invaluable use of controlled crack growth testing for ceramic materials and importance of the SPL specimen as a future research tool.

CHAPTER II

Literature Review

INTRODUCTION

It was suggested that catastrophic fracture of polycrystalline ceramics will succeed from events of small scale subcritical failure. The amplification of stress near sharp defects produces a process in which microstructural forces are redistributed as weak elements fail and stronger elements bear more load until, finally, material resistance is exhausted. If events of subcritical failure do precede fracture then it is expected that they will leave evidence of their presence. Examination of current fracture research for ceramics can be used to demonstrate that subcritical failure occurs routinely and that it leads to measurable amounts of subcritical crack growth (SCG) in both fracture toughness and strength tests. The following is a discussion of several experimental studies where subcritical crack growth has affected the performance of a brittle material and the appearance of a fracture surface. Two major test techniques considered in this discussion are strength and toughness testing. Although these tests differ in that the crack size is unknown for strength tests but is generally known for fracture tests, both are affected by the response of the ceramic material to a sharp discontinuity. In addition to the failure behavior of polycrystalline ceramics, some attention is given to the failure response of inorganic glass. The microstructure of each material is significantly different, but both are brittle and since glass is easier to test it has provided much to the present

understanding how ceramics fail.

SUBCRITICAL CRACK GROWTH AND STRENGTH TESTING

Failure Modeling

Most strength prediction models utilize probabilistic based approaches involving the WL theory to account for inherent scatter in test data. Strength of the bulk specimen is assumed to be controlled by the local strength of the weakest element, and the strength of each volume element is independent of its neighboring elements. These approaches are referred to collectively as a fast fracture theories and nearly all incorporate the following assumptions:

- (1) Flaws of varying severity are homogeneously distributed throughout a component.
- (2) Structural component failure is determined by the weakest link failure of independent single elements.
- (3) The failure characteristics of defects within each element are independent of applied loading.

An individual element can be small provided it contains a representative population of material defects. Material performance is characterized through extremal statistic which is used to model either the critical fracture stress (Weibull,1939), the failure nucleating flaw population (Batdorf,1974), or the effective fracture surface energy (Chudnovsky,1987). Weibull stated that the probability of achieving a critical stress within a body increased exponentially with volume size. To account for this scale effect he proposed a volume integral approach given as

$$P(\sigma_{eff}) = 1 - \exp \left[- \int_V \left(\frac{\sigma_{eff} - \sigma_{min}}{\sigma_o} \right)^m dV \right] \quad 2.1$$

The value σ_{eff} is the maximum principal stress, σ_o is a scaling parameter and σ_{min} the stress level below which fracture will not occur. The parameter m is commonly referred to as the 'risk of rupture' or the Weibull modulus. His volume integral approach was established using experimental data from uniaxial stress tests and it provides accurate results such setups. When employed with more complex loading configurations Weibull's approach proved to be less than successful (Weill,1964;Johnson,1985;Swank, 1981). It was argued that Weibull's approach was deficient for polyaxial loadings because a failure probability exists in any direction with a net positive stress (Freudenthal,1969;Margetson,1976). Consequently, the actual failure direction may not coincide with the maximum principal stress direction. Proposed modifications to account for complex stress states included assuming that each positive principal stress independently contributed to the total risk of failure, therefore the total probability of failure should be related to the product of the individual probabilities. Unfortunately, such an extension of Weibull's original approach was arbitrary, as there was no physical reason why one should only consider the principal stress components.

Batdorf and Crose (1974) argued that treating each positive principal stress independently was inappropriate in that the combination of two or more principal stresses

may cause failure where the independent action of each may not. They recognized that the complexities of fracture for a brittle solid could not be captured using the purely phenomenological model proposed by Weibull. The primary weakness was that Weibull's treatment did not contain the essential mechanics required to account for complex stress states. It was known from fracture mechanics that material defects disrupt stress patterns and lead to cracking, and such a process had to be addressed separately.

To account for the influence of material defects Batdorf (1978) proposed a model which incorporated conventional fracture mechanics concepts. Although Batdorf also uses a stress-based criterion for failure, his approach differs from Weibull's in that information concerning the character of flaws producing failure can be extracted from laboratory tests and used to assess the influence of more complex loadings. A flaw's shape is an invariant property of the material, and the flaws that produce failure in simple laboratory tests are expected to be the same as those which will produce failure in a larger component. The fracture toughness of the material is assumed constant and failure nucleating flaws are treated as a cracks.

The advantage of a fracture mechanics approach is that a Griffith (1921) or Irwin (1948) failure criterion can be used to relate remotely applied stress to the probabilistic size and orientation of a material flaw. The functional relationship between applied stress and a critical flaw size is expressed through stress intensity factors, K_I and K_{II} , which describe the asymptotic behavior of stresses near a crack tip. The values K_I and K_{II} , referred to as the Mode I and Mode II stress intensity factors, account for the crack-

plane normal and transverse components of stress, σ_{nm} and τ_{nm} , respectively. For a crack in an infinite two-dimensional medium, as shown in Figure 2.1, these stress intensity factors, K_I and K_{II} , are expressed as

$$K_I = \sigma_{nm} \sqrt{\pi a} \quad 2.2(a)$$

$$K_{II} = \tau_{nm} \sqrt{\pi a} \quad 2.2(b)$$

where E is the elastic modulus of the solid and 'a' the crack length. Instability is marked by the dynamic extension of a crack front and occurs when the combination of these two factors reaches a critical value. The critical value is related to the effective fracture surface energy, which is Griffith's energy, γ , as

$$G = G_I + G_{II} = \frac{K_I^2 + K_{II}^2}{E} = 2\gamma \quad 2.3$$

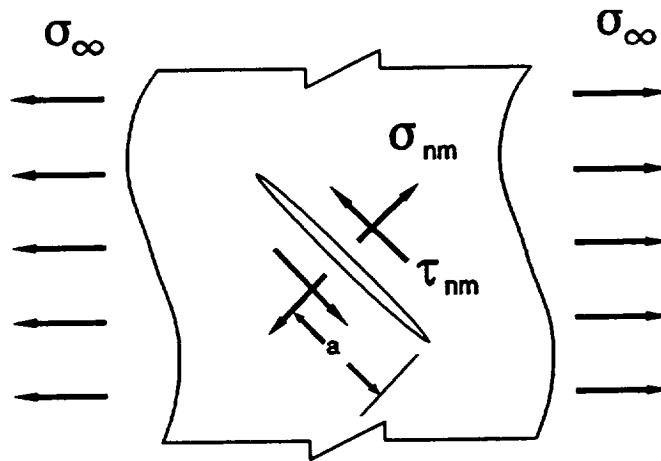


Figure 2.1: Infinite elastic solid with an imbedded crack of length $2a$ under arbitrary remote loading, σ_{∞} .

The value G is termed the strain energy release rate and at crack instability the strain energy release rate is twice the Griffith energy. The fracture surface energy is often assumed to be constant valued and is used to characterize the material response. In some cases higher energy release rates are observed under combined Mode I and Mode II loading and it is sometimes suggested that a modified surface energy may be utilized to account for mixed mode loading.

Coupling fracture mechanics concepts with WL theory allows the pre-existing population of material flaws to be directly incorporated into a design process. Since the stress state is often considered to be deterministic, a statistical description of the critical flaw population can be used to generate a probabilistic prediction of component behavior. The Batdorf model accomplishes this by defining a function, $N(\sigma_{cr})$, as the number of flaws per unit volume having a severity greater than some specified value relating to the applied stress. As proposed by Batdorf, the function $N(\sigma_{cr})$ represents the 'active' volume, or surface, density of flaws having a critical stress less than or equal to σ_{cr} . Term active is used to indicate the possibility that more than one flaw population may be present in the material. The functional relationship $N(\sigma_{cr})$ is assumed to be independent of applied stress implying that flaws do not evolve during loading. A general expression for the probability of failure is provided as

$$P_f^i = P_1 \times P_2 \quad 2.4$$

where P_1 is the probability that a flaw with a critical stress between σ_{cr} and $\sigma_{cr} + d\sigma_{cr}$

exists within an elemental volume, dV , and P_2 represents the probability that the flaw is critically oriented. The probability P_1 is related to the crack density function, $N(\sigma_{cr})$, and the probability P_2 is expressed as the solid angle, Ω , containing the normals of cracks for which $\sigma_{eff} \geq \sigma_{cr}$. The value of σ_{eff} is evaluated from the applied stress using some specified fracture criterion. The value 4π is the surface area of a unit sphere which ensures that the maximum value of P_2 will be unity. Batdorf's WL theory provides a generalized expression for the total probability of failure as

$$P_f(V) = 1 - \exp \left\{ - \int_V \left[\left(\frac{\Omega}{4\pi} \right) \frac{dN(\sigma_{cr})}{d\sigma_{cr}} d\sigma_{cr} \right] dV \right\} \quad 2.5$$

for a volume, V .

Once $N(\sigma_{cr})$ is defined, the only quantity required to calculate the failure probability is Ω which is a function of the applied stresses and a chosen fracture criterion. The function $N(\sigma_{cr})$ characterizes a particular material, it can be determined experimentally from failure load versus frequency results and fractographic studies. The detailed procedure for determining fracture properties from experiments is clearly outlined by Gyekenyesi (1986) who has codified Batdorf's theory as a finite element post-processor.

Batdorf's approach outlined above is currently the most popular model used to predict the strength of brittle materials. A material's performance is incorporated into the model by characterizing the variability of its failure strength using a statistical

distribution. The distribution are established by conducting several laboratory tests on specimens failed in simple uniaxial tension. The distribution of laboratory strengths is often approximated using the Weibull distribution given in equation 2.1, and the resulting Weibull modulus characterizes strength variability for a material. Materials with poor strength and large scatter will have a low Weibull modulus and higher strengths and a more narrow strength distribution yields higher a modulus. If the strength distribution is coupled with a failure criterion, flaw size distribution can be approximated, however, the underlying distribution remains constant.

Still there a lack of agreement between Batdorf's theory and experiment when failure occurs under more complex loading. Quite often experimental results reveal a reduced scale effect compared to that predicted from theory if only the normal stress component is considered. In order to account this discrepancy several fast fracture criteria have been proposed which include some contribution from shear, but the precise measure of a shear influence is not known (Batdorf and Heinisch, 1978). Today several criterion have been proposed which include both the normal and shear stress components but a clearly superior one that bridges the gap between experiment and theory has not been established. Boulet (1988) provides a comprehensive review of several fracture criterion which have been examined for ceramics and discusses the merits of those commonly used. Quite often energy-based criteria, for example the strain energy density or strain energy release rate, provide the best agreement with experimental observation of reduced scale effect. Discrepancies still remain and Batdorf suggests that some of the differences can be resolved if flaw planes are preferentially oriented, but this may imply

that flaw's evolve under load which counters a building assumption of the model.

The accuracy of Batdorf's WL model relies on whether test specimen material has the same flaw shapes and size distributions as structural component material. If a single Weibull modulus approximates strength variability well, then only one flaw population, or family of defects, is assumed to be present. However, if more than one modulus is required to characterize the variability of strength, the existence of multiple flaw populations is reasoned (Quinn, 1990). A simple example of two distinctly different flaw populations are surface and volume defects. Even though both types can cause failure, severe surface flaws often include sharp machining defects which are obviously not contained in volume flaws. Figure 2.2 demonstrates the change in Weibull slope, or active flaw population, created by testing the same hot pressed silicon nitride in tension and flexure.

Unfortunately most polycrystalline ceramics exhibit the failure behavior associated with two or more flaw populations (Easler, 1981; Helms, 1984; Amar, 1989) and this has seriously complicated relating specimen strength to component strength. Quinn (1983, 1990, 1991) has conducted numerous studies related to multiple flaw populations and its affect on modeling. In their 1991 review article on flexural testing, Quinn and Morrell conclude that multiple flaw populations restrict the range of sizes test data can be used to predict component reliability. They further recommend that strength data should be only extrapolated over a narrow size range which is comparable with the test specimen size. These authors believe that failed attempts to relate laboratory specimen strength to component strength may be due to the presence of multiple flaw populations.

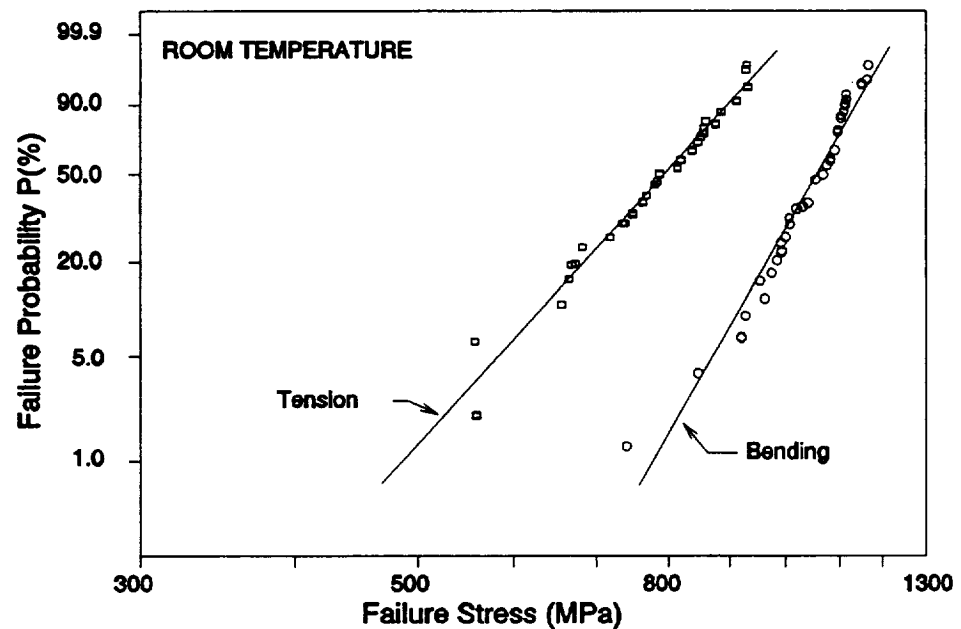


Figure 2.2: Weibull plot displaying the failure probability for a hot pressed silicon nitride failed under pure tension and bending.

Although more than one flaw population has an unknown influence on scaling, it is often argued that the current WL models adequately describe the failure of brittle materials. AN argued weakness of Batdorf's WL model is the lack of detailed information on the size, shape and location of failure nucleating flaws. For this reason Quinn (1991) highly recommends the use of fractography in 100 percent of all test specimens in order to identify common families of defects which precipitate failure. No attention is given to the possibility that changes in the Weibull moduli are caused by subcritical changes in flaw character prior to failure, even though this can have the same affect as multiple flaw populations. The criteria used to measure the conditions necessary for failure are determined from the applied stress, and statistical variations are imposed by the flaw population which is assumed to be invariant under load. If flaws

reach their critical size during loading their final shape and size, and subsequently their failure conditions, can depend on loading history. Therefore, one can argue that the changes in strength variability observed for ceramic materials is the result of changes in the subcritical evolution of flaws. The proof that flaws evolve prior to failure in strength tests can be found in the fractography patterns observed around failure nucleating flaws.

Fractography and Strength Testing

For many materials the process of brittle failure generates unique surface features which can be related to pre-failure conditions. Post-failure examination of the fracture surface of strength specimens has contributed much to the present understanding of brittle failure. Several studies have been used to establish a parametric relationship between surface patterns observed around failure nucleating flaws and the fracture process (Johnson,1966;Mecholsky,1976; Chao,1991). These relationships treat surface patterns as artifacts of the fracture process which are formed after critical fracture loads are reached. However, this is an assumption which has unnecessarily restricted quantitative analysis of fracture patterns and has lead to some inconsistent explanations of experimental results.

It is proposed in this discussion that subcritical crack growth plays a major role in the development of fracture patterns near failure nucleating flaws, and that some surface features thought to be created after reaching the critical load may be formed at lower loads. Examination of fractography results from both fast fracture strength testing and delayed failure testing reveal that subcritical growth is a natural failure event which

does not require stress corrosion arguments. Nevertheless, subcritical crack growth is traditionally treated as a stress corrosion related problem because it is often assumed that mechanisms contributing to damage tolerance are absent for most ceramics and glasses. The assumption that subcritical growth is stress corrosion activated is so dominant that results from delayed failure tests and strain-rate sensitivity tests are often interrelated without proof that such treatment is valid (Gee,1986). Yet, in many cases the existence of subcritical crack growth and its influence on test results is not well explained by stress corrosion arguments.

Fractography of Flaw Failure

The surface features relating to the brittle fracture from flaws have been classified as the stages of mirror, mist, hackle, and crack branching. These patterns have been identified on failure surfaces for inorganic glasses (Abdel-Latif,1977), single crystal and polycrystalline ceramics (Mecholsky,1981A) and metals (Rice,1984A) and they have been studied extensively. Mist and hackle could be described as a subtle rippling of the fracture surface. They are most easily observed in brittle amorphous materials because the microstructural heterogeneity is small scaled. Although the larger scale heterogeneity of single crystal and polycrystalline materials often mask a clear identification, these materials also exhibit mist, and hackle formations near failure nucleating flaws. For this discussion the formations of mirror, mist and hackle are referred to collectively as Mirror patterns. The fracture sequence of these patterns is displayed in figure 2.3. The three separate boundaries for mirror-mist, mist-hackle, and hackle-crack branching are

identified by the radial dimensions r_m , r_h , and r_{cb} from the origin of a failure-nucleating flaw. The mirror is a flat shiny region immediately surrounding the flaw. At a distance r_m a formation of small radial ridges occurs which is called the mist, and at a distance r_h mist evolves into a third formation of rougher ridges known as hackle. Quite often hackle formations are bound at a distance r_{cb} by a fourth region termed crack branching wherein large scale fracture ridges are formed.

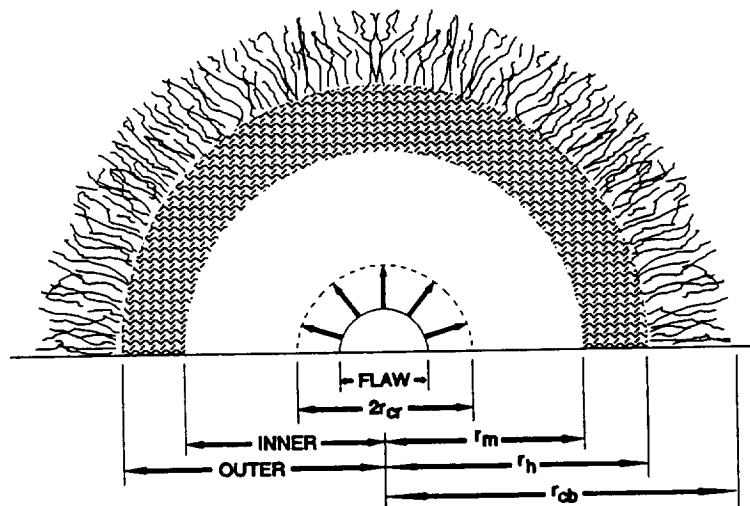


Figure 2.3: Graphic representation of the fracture mirror formations surrounding failure flaws observed for brittle materials.

All four regions of mirror, mist, hackle and crack branching are nearly always visible around flaws precipitating failure in strength tests of inorganic glasses and ceramics. In some cases crack branching may not occur, particularly for small specimens or materials with low strengths. There is strong evidence that crack branching pattern are influence by strain energy density and are generated after critical fracture are therefore not the subject of this discussion. The Mirror patterns displayed in single

crystals are similar to polycrystals except that individual characteristics are greatly influenced by energetically favorable cleavage planes (Abdel-Latif,1977;Becher,1978). Although the shape of failure-nucleating flaws is generally irregular, Mirror patterns usually possess an elliptical symmetry. Under uniform tension interior flaws develop nearly circular mirror-mist and mist-hackle boundaries, and semi-elliptical boundaries form around flaw failures near traction free surfaces. Mirror patterns can be often used to identify the flaws which precipitate failure in a component. The apparent universal presence of these patterns for brittle fracture in many materials suggests a common failure process which is independent of material microstructure.

Qualitatively the fracture process is believed to begin when the flaw propagates within the mirror as a sharp crack and its velocity increasing with increased crack length. Crack velocities increase monotonically with crack length up to the critical flaw size at which crack velocities are assumed to have reached a terminal value. The terminal velocity is the dynamic propagation rate which has been measured to be approximately 60 percent of the shear wave speed (Field,1971). Formation of mist, hackle and crack branching originate after the critical crack position when the additional strain energy released by the lengthening crack can no longer increase its velocity.

Since most ceramics and glasses are assumed to behave as ideally brittle materials the critical crack position, r_{cr} , shown in figure 2.3 can be evaluated using an approach based on a linear elastic fracture mechanics (LEFM). The absolute size of the fracture mirror at which crack propagation velocities reach dynamic speeds can be calculated from the measured fracture toughness, K_{Ic} , of a particular material, the specimen failure

stress, and an appropriate stress intensity solution similar to equation 2.6.

$$r_{cr} = \frac{\phi^2 K_{Ic}^2}{1.2 \pi \sigma_f^2} \quad 2.6$$

This stress intensity solution is given for an elliptical crack in an elastic solid, where σ_f is critical fracture stress, ϕ is a geometric correction factor for mirror shape, and K_{Ic} is the material's critical stress intensity factor. The crack shape correction factor, ϕ , has an estimated range of 1.4 to 1.6 (Mecholsky,1981B) and, because crack extension is often self similar, ϕ remains essentially constant for each Mirror boundary. Calculations of the critical flaw size using solutions similar to equation 2.6 yield r_{cr} values which are always less than the smooth mirror radius, r_m . For most glasses the ratio of the smooth mirror radius, referred to as the inner mirror, to critical radius is approximately 10:1 and for most ceramics a smaller ratio averaging 6:1 is found (Rice,1979). A second ratio defined as the outer mirror ratio uses the hackle radius, r_h , to critical radius and this value averages approximately 13:1 for both glasses and ceramics. Since $r_{cr} < r_m$ the transition from slow to dynamic crack growth occurs within the mirror formation and leaves no distinctive mark for the critical position. The formations of mist, hackle and crack branching occur after crack velocities have reached a terminal value.

The first attempt to quantitatively relate Mirror boundaries to remotely applied stresses was accomplished by Johnson and Holloway in 1966 when they demonstrated that the product of the failure stress and the square root of the distance from the center

of the fracture origin to the inner and outer Mirror boundaries was essentially constant for a given material. This empirical relationship is expressed in equation 2.7

$$\sigma_f \sqrt{L} = A \quad 2.7$$

and the value A is often referred to as the mirror constant. Fracture mirror radii have been studied extensively in attempts to either prove or disprove universal application of equation 2.7. This debate has endured for over two decades and although several researchers are firmly convinced of its universality (Rice, 1984A; Mecholsky, 1979, 1981B; Kirchner, 1974) the results of other researchers (Shetty, 1980; Abdel, 1977, 1981; Krohn, 1971) suggest Johnson and Holloway's empirical relationship is not widely applicable. The interested reader is referred to Rice (1984A) who provides an excellent historical review of observations relating to surface patterns and fracture stress. Although the debate continues, the common agreement has been that both mist and hackle are formed after the crack reaches its critical size and crack velocity reaches its terminal value.

Actual crack velocity versus crack position measurements have not been made, however, and although it is generally agreed that mist and hackle form after the critical crack size, there are reasons to argue that these patterns form during subcritical crack growth. In doing so much of the controversy surrounding application of Johnson and Holloway's expression can be understood. If the inner and outer Mirror boundaries form subcritically, then the functional relationship between fracture stress and crack length observed by Johnson and Holloway is naturally explained by LEFM since critical fracture criteria are related to the product of critical stress and the square root of the crack length.

One might well argue, as discussed later, that empirical Mirror constants are actually experimental measurements of the critical stress intensity factor which has not been corrected for crack shape and size, or specimen geometry. Distortions to Mirror patterns and anomalous Mirror constants which cannot be explained by the simple formulation proposed in Johnson and Holloway's expression are in many cases easily explained in terms of static stress intensity factors.

Consider the influence of strain gradients which is often cited as the principal source of distortions to mirror patterns (Rice,1984A). Whereas stress intensity solutions can account for remotely applied strain gradients, equation 2.7 cannot without an arbitrary treatment. Mirror pattern distortions were noted by Abdel-Latif, Bradt, and Tressler (1977) when they studied the effect of stress state. They found that mirror constants consistently increased from uniaxial tension to four point bending and finally three point bending. The authors conclude that the general criterion for mirror formation given in equation 2.7 cannot be used and strain gradients need to be addressed. Similar affects of strain gradients have been observed by other investigators (Johnson,1966;Chao,1991).

Johnson and Holloway (1966) were able to show that the distortions in mirror patterns observed when strain gradients are present can be accounted for in equation 2.7 if σ_f is adjusted at each point along the Mirror boundary. Such a technique for averaging out the influence of a strain gradient is crude and leads to inconsistencies when compared to compared to the actual stresses determined by more rigorous stress intensity solutions. Kirchner (1979) and Bahat (1982) were able to show that the boundaries for mist and

hackle patterns could be related to stress intensities. Shetty (1980) demonstrated that the adjustments proposed by Johnson and Holloway to account for flexural strain gradients yield mirror boundaries which do not correlate with contours of constant stress intensity. The inconsistency Shetty exposed is that if, as generally believed, cracks propagate at constant levels of stress intensity then Mirror boundaries do not mark instantaneous positions of the crack front provided Johnson and Holloways approach is accurate. Since it is difficult to accept that mirror boundaries are not formed simultaneously, as is suggested by Rice (1984A), Johnson and Holloways expression is left without physical support.

Mirror constants are also influenced by the shape of failure nucleating flaws. Rice (1977,1984B) found that Mirror radii forming from pore failures in a dense glass are smaller than those produced from sharper flaws of the same size. They attributed the smaller mirror radii to pore bluntness and account for its influence by introducing a stress correction factor into equation 2.7. Rice's approach provided better estimates of mirror constants, but it did not produce the expected agreement with normal mirror ratios (Rice,1984A). The unresolved difference may be the result of an unsuitable treatment for stress singularities near pores. Accounting for pore bluntness by modifying the stress is not consistent with stress intensity solutions for cracks emanating from pores (Tada,1985). Such a configuration does have a reduced singularity if compared to a sharp elliptical crack with an equivalent total length which includes the pore size. However, stresses are actually amplified near a pore and the reduced singularity results from the change in measuring crack length, not reduced stresses. If mist and hackle do

form at constant stress intensity factors, one expects Mirror boundaries to form at larger distances from the fracture origin which is contrary to Rice's observation. Interestingly, re-examination of Rice's (1984B) results reveal that one internal pore failure had a Mirror to pore size ratio of 18:1. This ratio produces a mirror constant in very good agreement with sharp flaw failures if it is assumed that the outer Mirror is formed at a constant stress intensity level. However, even the early formation of mist and hackle from pores may be consistent with constant stress intensity arguments. If the pore is smooth and a small crack does not exist then a sharp crack may need to be 'popped-in' by overloading. Once created, the shielding effect of the pore is already offset by the high pre-existing stress state prematurely produces mist and hackle. This affect would be similar to dynamic loading rates where quite often mirror patterns form prematurely, and in some cases for very high loading rates are absent as pointed out by Rice (1984A).

Other support for a subcritical interaction between applied stress and mirror patterns can be found in the delayed failure behavior of glasses and some ceramics. Mecholsky (1979) showed that sustained lower loads in soda-lime glass produced larger mirror sizes, however, the stress intensity level at which the inner and outer Mirror boundaries formed remained constant compared to rapid fracture tests. He found that specimen survival time correlated better with the increased size of the outer Mirror boundaries than the critical flaw size estimated using equation 2.6. Mecholsky suggests that improved correlation occurs because mirror patterns inherently contain aspects involving subcritical crack growth and are less affected by the irregularity and non-perpendicularity of the nucleating flaw. The implied relationship between mirror size

and subcritical crack growth, and the fact that mirror constants determined from delayed failure tests agree with rapid test values are easily rationalized if mirror boundaries are formed subcritically.

It is worth noting here that the usual power law for crack growth used by Mecholsky is derived empirically from other tests and there is no proof that the relationship is valid for all applications (Gee,1986). Typically, for room temperature tests the power exponent is very large (sometimes greater than 30) and it can be shown (see Appendix A) that measurement errors expand rapidly. Considering the sensitivity of the crack growth model to small fluctuations when exponents are large one might question its utility for life prediction. The suggested relationship between lifetime (subcritical crack growth) and mirror size determined by Mecholsky may be explored in better detail provided more appropriate crack growth models can be established.

Finally, Batdorf and Heinisch (1978) suggest that experimental observations of a reduced scale effect can be explained if flaws are preferentially oriented (by the applied stress), and there is overwhelming evidence of such a bias for Mirror planes. However, the bias in Mirror orientation can only affect strength measurements if they are formed subcritically. In their mixed-mode studies, Freiman, Gonzalez, and Mecholsky (1979) placed indent induced flaws at controlled angles to the maximum principal stress direction. They noted that mirror planes quickly formed normal to the principal stress direction. After failure, the authors noted that two asymmetrical Mirrors had formed, one at each tip of the induced crack. Quite often one Mirror pattern dominated and the plane of the dominating mirror was usually perpendicular to the direction of principal

stress. Freiman found that, even under remotely applied mixed-mode loading, the radii of the dominate Mirror pattern compared well with those produced in pure Mode I loading.

Preferred mirror orientations are also exhibited in the multi-axial stress tests of hot-pressed silicon nitride conducted by Chao and Shetty (1991). The preferred plane normal orientation occurs so frequently in their studies that Chao and Shetty advise that a delta function may best approximate the sensitivity of fracture on flaw orientation in weak link calculations. To explain the preferred orientations of fracture Mirrors the authors suggest that cracks may be 'nucleated' under the influence of applied stress. Although Chao and Shetty do not specifically discuss the nucleation event, they conclude there exists a subcritical interaction between crack growth and applied load. Furthermore, this interaction will affect existing predictive techniques in a manner not currently addressed.

Finally the elliptical shape of Mirror boundaries and the self-similar nature in which they form as a continuous crack front, driven by fracture forces, provides strong evidence that mist and possible hackle are formed subcritically. The best examples of this self-similarity can be found where two flaws interact to produce failure, yet each, is surrounded by Mirror formations centered on a flaw origin. Figure 2.4 is a fracture surface micrograph of a glassy carbon specimen taken from the studies of Rice (1984A). Two fracture mirror formations can be seen in the figure: a dominate mirror which originated at the beveled edge, and a minor fracture mirror with its origin along the extreme fiber edge. The author proposes that only one fracture origin at A is present and

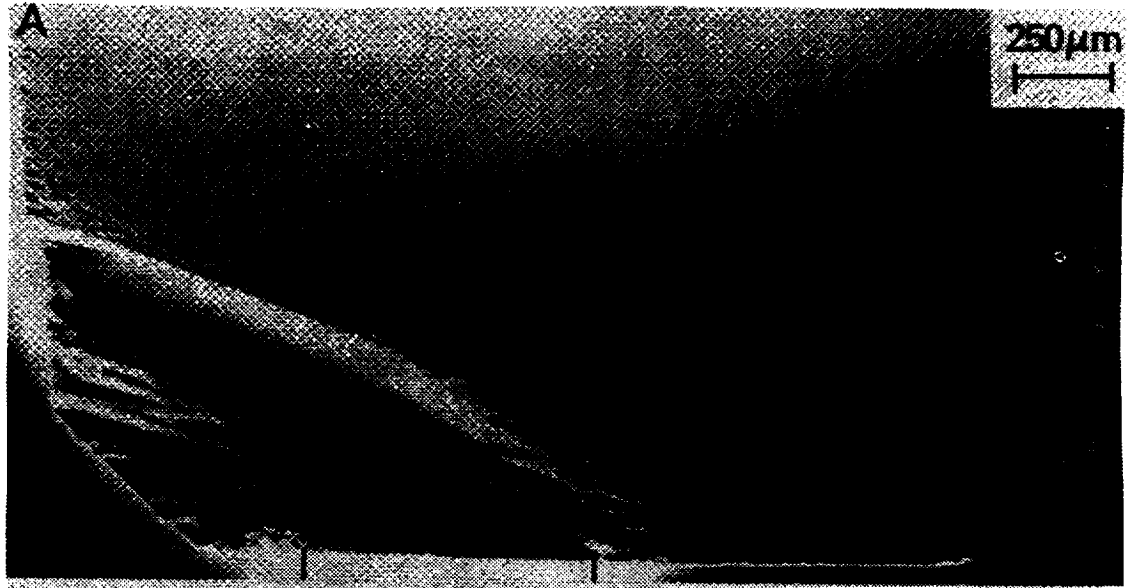


Figure 2.4: Glassey carbon fracture surface showing multiple mist and hackle formations (Rice, 1984A). Multiple patterns are taken to suggest SCG precedes final failure.

the minor mist area was actually produced by the main crack front as it propagated out from the beveled edge at terminal velocities. This explanation seems unlikely as it neglects the semi-elliptical shape of the minor mirror which is centered on a surface flaw located at B. It is more likely that the minor mirror evolved independently from the second flaw at subcritical loads. The minor fracture mirror did not reach criticality before the larger mirror and it was eventually overcome by the dominate crack front. This micrograph is very useful as it provides a snapshot of the extent, nearly 200 μm , of subcritical crack growth possible without creating failure.

Figure 2.5 is also an excellent example of multiple flaw interaction during

subcritical crack growth studies of MgF_2 (Healy, 1984). The two crack fronts originated from co-planar flaws induced in a flexural beam by a hardness indenter. The figure shows five distinct regions of fracture topography. The first, region A, is a transgranular crack branching zone generated by the indenter. The second zone, region B, most likely occurred rapidly as the two crack fronts joined during the initial stages of loading. Regions C and D are generated by subcritical crack growth conditions and the boundary between regions D and E is likely the position of the crack front at critical fracture. Here as much as 300 μm of subcritical crack growth occurred prior to final failure. Also, the distinct change in surface contrast between regions C and D suggests a change in the fracture process during subcritical growth.

Although two, and sometimes three distinct boundaries can be identified in Mirror patterns it is surprising that none are associated with the critical crack size. Particularly since the larger scale fracture studies discussed next demonstrate clear indications on the fracture surfaces of critical crack positions (Salem, 1987; Wiederhorn, 1973). Mecholsky (1981A) has performed several fractography studies of failure in both glasses and ceramics and he states that the reason there is no observable critical flaw boundary is that "the transition from stable to unstable crack growth is continuous and smooth..." and occurs without a known inflection. He references earlier work of Field (1971) to support the assumption of a smooth and continuous transition, yet, Field's crack velocity measurements were not able to capture the earliest stages of crack initiation. The lowest velocity measurement obtained by Field was 300 m/sec and the crack length was already more than 1 mm long. Thus, if subcritical crack extension is only a few hundred

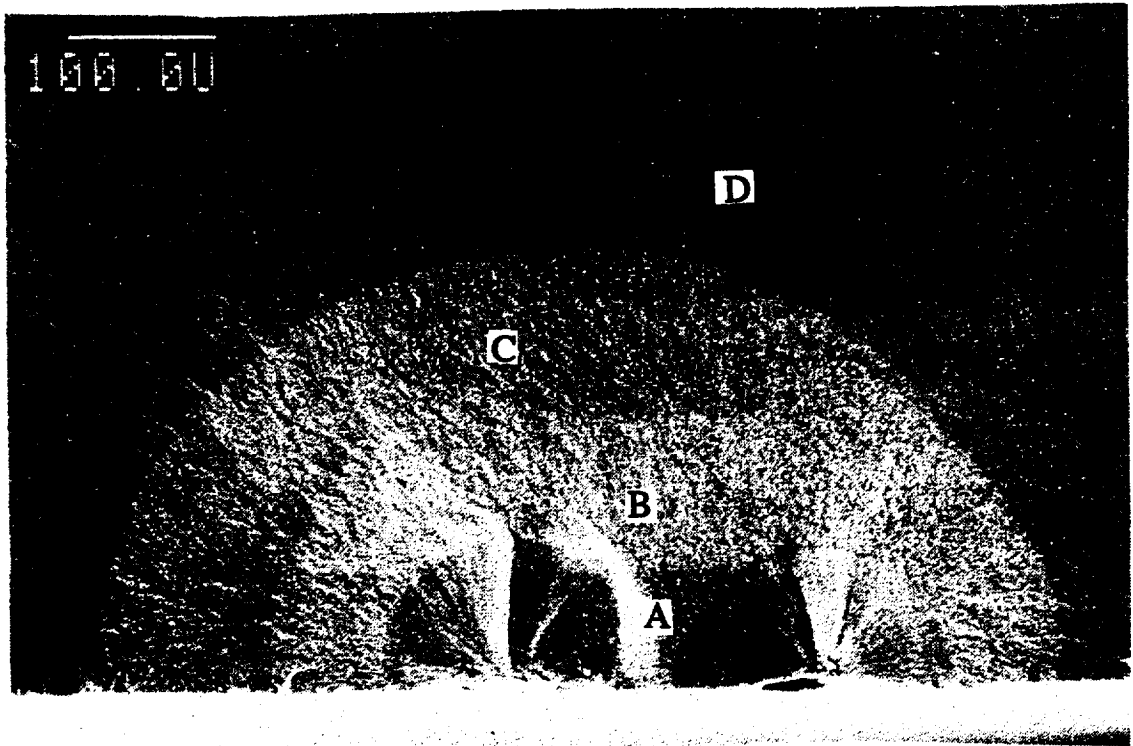


Figure 2.5: Fracture surface (MgF_2) with two flaws showing four mirror patterns A, B, C, and D. (Healey, 1984).

micrometers long, the events preceding dynamic initiation had already been missed. Apart from Field's work, there is a general lack of physical measurements for the crack velocity behavior during the earliest stages of crack initiation which supports the assumption of a continuous and smooth transition. Furthermore, it is reasonable to expect that an inflection does exist if crack velocities increase monotonically during the early stages of crack growth, yet later reach a terminal value. Once again the lack of understanding relates to the inadequacies of existing test techniques which are incapable of providing the refined experimental measurements needed to characterize incipient nature of the fracture event.

Perhaps the most limiting restriction against assigning either the inner or outer

mirror boundary as the critical flaw size are unrealistic estimations for the critical stress intensity. The inner and outer mirror radii yield critical stress intensities which are slightly more than 3 times greater than those measured in large scale tests. Therefore, without modification, LEFM solutions leave no basis for claiming that subcritical growth could extend beyond the smooth mirror. Still it is natural to argue that the critical fracture position will leave its trace on the surface and, therefore, either the inner or outer Mirror boundary is a measure of the critical crack size. Larger subcritical crack lengths could be explained if the non-linear elastic effects such as increased surface roughness for glasses, or inelastic effects such as crack bridging for ceramics significantly alters solutions for the crack driving forces when crack lengths are small. The presence of these mechanisms had already been established in the previous studies of Wiederhorn (1973) where 'tear' marks on the fracture surface were associated with a 20% increase in fracture resistance.

Although the exact influence of non-linear mechanisms on stress solutions for small cracks is not known, there is experimental support to suggest that the LEFM solution given in equation 2.6 overestimates the crack driving force for small crack lengths. Mecholsky, Rice and Freiman (1974) conducted fracture mirror studies on several glasses and the results of these studies are re-plotted in figure 2.6. The data was used as evidence that there is a $1/\sqrt{r}$ functional relationship between Mirror size and failure stress, but a linear regression analysis of their results reveals a reduced response in the crack length versus failure stress relationship. Although large scatter exists, the

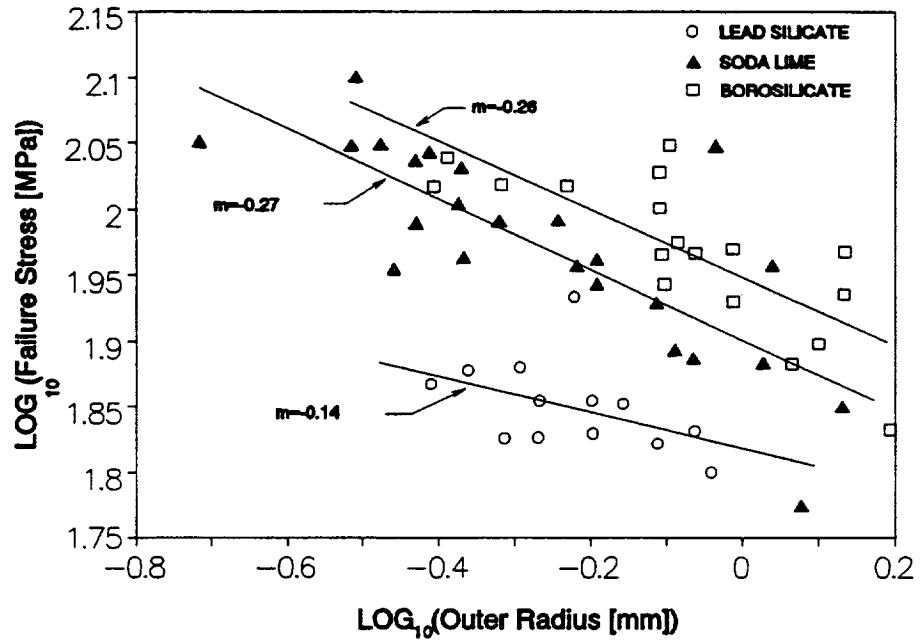


Figure 2.6: Plot of failure stress, σ_f , versus outer mirror radius, r_b , for several inorganic glasses (Mecholsky, 1974) with linear regression analysis slopes.

data presented for both the lead silicate and borosilicate glasses reveal distinct trends which do not agree with a $1/\sqrt{r}$ functional relationship. Linear regression analysis of the data presented in figure 2.6 yield radial exponents of $-1/10$ for the lead silicate and $-1/5$ for the borosilicate material which are significantly greater than the predicted $-1/2$ used by the authors¹. Although discrepancies between experimental results and the expected $1/\sqrt{r}$ functional relationship are often excused as scatter, several other studies involving ceramics and glasses (Kirchner, 1974; Bansal, 1977; Govila, 1981; Lewis, 1981;) reveal slopes which are often greater than $-1/2$ and only approach $-1/2$ at longer crack lengths. For ceramics, these reduced slopes would be consistent with the presence of

1 This author was not able to confirm the $-1/2$ slope of solid line plotted in the reference.

interlocking mechanisms capable of reducing stress singularities at the crack tip.

Quantitative results concerning interlocking forces were obtained by Mutoh, Takahashi, and Kanagawa (1992) when they specifically addressed the influence of crack bridging mechanisms on small cracks. They established that for small semi-elliptical cracks of less than 300 μm crack bridging forces may reduce crack tip stress intensity factors by a factor of 1/3 compared to solutions where bridging forces are not considered. Therefore if crack bridging forces are developed during mist or hackle formation in ceramics, actual crack tip stress intensities evaluated using the outer mirror boundary would be in good agreement with those measured in larger scale fracture tests. The analytical results presented by Mutoh, Takahashi and Kanagawa also demonstrated that the dependency of failure stress, or actual crack driving forces, on crack length for small size cracks was not \sqrt{r} when crack bridging forces were included in the analysis.

SUBCRITICAL CRACK GROWTH AND TOUGHNESS TESTING

Subcritical crack growth studies employing conventional fracture specimen geometries and analytical treatments are limited for ceramics because sharp, through-thickness cracks have been difficult to obtain. However there is a small variety of fracture tests which have been used successfully and these include the chevron notch (CN) specimen, the double-cantilever beam (DCB) and double torsion (DT) specimens, and the recently introduced single-edge-precracked-beam (SEPB) specimen. The results of other research presented here demonstrates that subcritical crack growth occurs in the

absence of corrosive environments, and that such growth has an influence on the fracture behavior of brittle materials.

Inorganic Glass Materials

Amorphous inorganic glasses demonstrate a high sensitivity to stress corrosion cracking and quite often subcritical cracking occurs because the crack growth resistance of the material is degraded. Although highly sensitive to stress corrosion, fracture tests of glasses have exhibited subcritical crack growth behavior which is inconsistent with stress corrosion arguments. Wiederhorn, Evans and Roberts (1974A) used the DCB specimen to perform fracture studies on several glasses at high vacuum for a NASA Skylab project. Six types of glass were tested and the authors reported that, even at high vacuum, all exhibited a sensitivity to strain-rate during fracture with measurable amounts of subcritical growth occurred before failure. For the Skylab project crack propagation rates were examined as a function of applied stress intensity and in these tests a borosilicate glass in water saturated air demonstrated a distinct change in its functional relationship at low compared to high crack velocities which suggested a change in the fracture process. At high velocities, crack growth had a reduced sensitivity to increases in load if compared to the response at lower velocities. The change in crack growth behavior represents a common response where subcritical crack growth is stress corrosion insensitive. In a separate discussion on subcritical crack growth in brittle materials, Wiederhorn (1974B) states that the active mechanism for subcritical crack growth when stress corrosion is not active may be crack blunting. Maugis (1986)

suggests that subcritical crack growth is a normal mode of propagation in brittle materials without any influence from stress corrosion, and provides an analytical treatment for other possible mechanisms.

Crack growth resistant mechanisms in inorganic glass may be mechanical as evidenced by another experiment conducted by Wiederhorn (1973) using DCB tests and borosilicate glass. Wiederhorn noted here that crack propagation ceased abruptly when small decreases in load occurred and a considerable overload was required to re-initiate crack extension. Approximately 20% higher applied loads were required to re-initiate crack growth when compared to pre-arrest conditions. After motion was re-initiated, crack velocities were observed to be significantly higher than pre-arrest conditions and the fracture surface at the arrest point exhibited 'tear' marks. Similar fracture surface features were noted in organic glass test conducted by Kim and Chudnovsky (1991). They found that after crack arrest, the early stages re-initiating crack growth 'rippled' the fracture surface and they termed these ripples deltoids. They also found that re-initiation required higher fracture loads and were able to correlate increased loading with the number of surface deltoids.

Polycrystalline Ceramic Materials

The DCB and DT specimens were some of the first conventional fracture geometries used to generate crack growth data for ceramics materials because sharp precracks could be introduced with relative ease. Stress corrosion cracking in these test configurations should produce a smooth and continuous crack growth behavior

(Evans,1974;Wiederhorn,1974B) and this has been demonstrated for glasses, and ceramics with a high glass content for example Al_2O_3 , and MgF_2 . However, observations of erratic and discontinuous crack growth behavior using the DCB and DT specimens are not explained by stress corrosion arguments and have been used to suggest that other mechanism might be active. Slow crack growth tests were performed by McKinney, Bender and Rice (1991) using the DCB and DT specimens on various types of silicon nitride, Si_3N_4 , having different levels of oxide additives and compared their results to strength tests performed at different strain rates. Although they observed evidence of room temperature subcritical crack growth from natural flaws in strength testing and suspected it to be stress corrosion related, the same materials tested using the DT and modified DCB specimens did not exhibit fracture behavior consistent with stress corrosion arguments. Rather than the continuous crack extension expected for stress corrosion cracking, the Si_3N_4 materials exhibited erratic and discontinuous crack extension with several increments of arrest and dynamic initiation.

McKinney concludes that the grain boundary's oxide phase and its character sufficiently pins macroscopic crack fronts in the DCB tests, but the smaller crack fronts of natural flaws allows subcritical growth. He proposes that the number of well pinned grain boundaries determines behavior and the greater number encountered by the macroscopic crack front restricted slow growth. However, this reasoning is not convincing since the distribution of pinned grain boundaries along both crack fronts will be the same and, if the pinning force is modeled as a distributed stress, the resulting pinning stress at the crack tip should be equivalent for both fronts. A more detailed

fracture mechanics analysis would be required for both cases to make a definitive statement concerning the relative affect of pinned boundaries.

Similar erratic crack extension behavior has been observed by Salem and Shannon (1987) during fracture toughness tests of the NC-132 silicon nitride material. Using the CN short bar specimen, the authors found that macroscopic crack growth occurred as alternating increments of subcritical growth which were interrupted by 'bursts' of unstable dynamic extension. Fractographic studies revealed that increments of subcritical crack growth were marked by changes in surface texture. Changes in surface texture produced contrast bands on the fracture surface which correlated with positions of arrest and initiation of dynamic extension. Salem was able to use the fracture surface markings to estimate stress intensity factors at arrest and dynamic initiation and calculated average values of 4.70 and 4.96 $\text{MPa}\sqrt{\text{m}}$, respectively. Although the authors concluded that NC-132 has a constant valued crack growth resistance at room temperature, they neglect to provide reasons for the interrupted subcritical growth and the resulting changes in fracture surface morphology.

The erratic crack growth observed by Salem is not only inconsistent with stress corrosion arguments, it is not consistent with the expected performance of the CN configuration. The increasing crack front of the CN specimen has the affect of reducing the driving force as the crack extension continues and this reduction is specimen geometry dependent. The reduction continues up to a critical point where the driving force begins to increase with crack extension and only then dynamic growth rates expected (Munz, 1982). If a material has a constant valued fracture resistance, the CN

geometry should yield continuous subcritical growth up to the critical position of dynamic initiation. The presence of discontinuous growth at crack lengths less than the critical value cannot be explained unless the material is capable of increasing its resistance during growth. Increased resistance could produce the overloading capable of triggering dynamic initiation. Since an increase in fracture resistance is necessary to explain Salem's observations stress corrosion arguments will not explain the erratic growth behavior. Although Salem and Shannon conclude that stress intensities at arrest and dynamic initiation are equivalent given the error in their measurements, the arrest toughness is less than the dynamic toughness. It is important to note this difference may be larger if the NC-132 material does have an increasing material resistance. The chevron-notched geometry, its stress solution, and the critical crack length for instability are strictly established for flat crack growth resistant materials (Munz, 1982), and the presence of increasing crack resistance complicates an assessment of true fracture properties.

Finally, some interesting results have been recently obtained by Choi (1992) from back-face strain gage measurements of SEPB specimens loaded in four-point bending. Using displacement controlled loading, compliance measurements of applied bending moment versus strain reveal increasing strain readings at constant load immediately prior to failure. This compliance behavior was observed in all test specimens of two separate hot pressed silicon nitride materials. Although their results are preliminary, the compliance behavior reveals evidence that subcritical crack growth occurs prior to catastrophic failure. Moreover, this subcritical growth occurs at constant load in the four

point-bending specimen implies that fracture resistance increases. The SEPB precracked beam is becoming one of the most widely used specimens for measuring the fracture toughness of monolithic ceramics. Yet, Choi's back-face strain measurements indicate that a material thought to possess a constant valued toughness may exhibit an increasing resistance when more detailed measurements are taken. It will be interesting to know how other ceramics perform when similarly tested.

SUMMARY

Experimental evidence discussed above suggests that catastrophic fracture in brittle materials does not occur without precursor events. The strength of inorganic glass is influenced by subcritical crack growth in every test environment considered. Room temperature fracture tests of several polycrystalline ceramics demonstrates a stick-slip fracture behavior relating to subcritical crack growth behavior which is inconsistent with stress corrosion arguments. Salem (1987) found that each stick-slip event produced distinct changes in the appearance of the fracture surface. And compliance measurements of Choi taken from the back face of flexural fracture specimens suggests that crack growth resistance may increase before fracture for some Si_3N_4 materials.

Subcritical crack growth also affects strength testing as evidenced by changes in the Weibull modulus for a material and the fractography of failed surfaces. The surface patterns for mist and hackle always develop self-similarly and imitate the propagation of a crack front driven by fracture forces. Mist and hackle patterns are found in both amorphous glasses and polycrystalline ceramics which suggests that there is a common

mode for brittle fracture which is independent of microstructure. At the end of the review by Rice (1984A) Cina comments:

"Is it not surprising that fractographic features such as mirror, mist, and hackle are observed both in amorphous materials such as glass and in crystalline materials such as alumina, magnesia, calcium fluoride, and graphite?

If there is a mode of fracture common to all these materials, does this not imply that it is one which cannot not be explained by one of our conventional crystallographic mechanisms and therefore we should seek a new mechanism?

Furthermore, if crystalline material can fail in a non-crystalline manner, need the phenomenon be confined to ceramic materials. Could it be that some of the problematic features sometimes associated with brittle fractures in metals are caused by such new fracture mechanism or mechanisms?"

Directly relating mist and hackle formations to the product of remotely applied stresses and the square root of its distance from the fracture origin has no physical basis. Remotely applied stresses are not present in the vicinity of a crack front. The evaluation of actual stresses must include the possibility that resistance mechanisms other than the breaking of atomic bonds are being activated by the fracture process. For glasses these new mechanisms may be the rippling of the fracture surface noted by Wiederhorn (1973) and Kim (1991), and for ceramics they may include crack bridging or microcracking. Mutoh (1992) demonstrated that neglecting these mechanisms can result in significant over estimations of the fracture force for small cracks. It was shown that the size of the outer mirror is far less sensitive to failure stress than proposed by Johnson and Holloway's expression which also suggests that fracture forces are less than predicted for small cracks, and the extent of subcritical crack growth may be more.

Whatever the cause, there is strong evidence that subcritical crack growth is a common mode of failure prior to catastrophic fracture for brittle materials. Its existence implies an interdependence between the load history of a sample and the shape, size, and

orientation of a crack front. Many of the current models used to predict the failure behavior of ceramics are very sensitive to the strength fluctuations caused by subcritical growth. If little is known about the interdependence between applied stress and subcritical crack growth, much will be left unknown in the performance of ceramic components. Assessing the performance of a ceramic material requires an understanding of its behavior. For fracture this means identifying failure mechanisms and predicting how they influence the conditions governing catastrophic fracture. This requires the development of test procedures which allow researchers to observe and record the effects of subcritical failure events.

CHAPTER III

Test Specimen and Procedure Development

INTRODUCTION

Observing crack growth behavior and measuring fracture resistance properties of ceramics has been hindered by an inability to produce sharp, through-thickness cracks and to control the propagation rate. Establishing stable crack growth in ceramics is complicated by the material's inherent low damage tolerance and relatively high stiffness. The obstacles associated with producing controlled crack growth in a brittle, high modulus material for experimental studies are discussed in this chapter. This is accomplished by demonstrating that a single parameter, for example the critical fracture toughness K_{Ic} or G_{Ic} , does not adequately describe the conditions for propagation instability. A key to modeling the fracture behavior of ceramics relies on an understanding of the theoretical conditions governing stability and how they are influenced by experimental procedures.

One major product of this research is the development of a specimen design and loading technique which enables controlled, pure Mode I crack growth studies to be performed with monolithic ceramic and other high modulus brittle materials. The specimen configuration, termed the Stable Poisson Loaded (SPL) specimen, is very similar to a testing standard already adopted by the American Standards and Test Methods community (ASTM E561,1992). The technique approximates a fixed-displacement controlled test by achieving a low load system compliance. The problem

of gripping and grip alignment, inherent in brittle material testing, is addressed with a novel loading method. Loads are applied to the specimen through the Poisson expansion displacement of a compressively loaded cylindrical pin. It will be shown that the SPL specimen and loading technique possess those qualities required, from both theoretical and experimental viewpoints, to produce sharp, through-thickness cracks and promote controlled crack growth in ceramic materials.

STABLE CRACK EXTENSION

Elastic Instability

During the course of these studies, it was found that the primary factor controlling crack stability was the amount of energy available for sustaining propagation within the elastic system. A review of the required conditions for dynamic crack extension provided the basis for developing the SPL specimen. The theoretical conditions governing fracture stability were considered in terms of the total free energy of an elastic solid with a traction free crack of length 'a' as shown in figure 2.1 without shear forces. This was accomplished by writing Gibb's potential, Ψ , for an elastic solid with a crack as

$$\Psi = \Pi + 2\gamma a \quad 3.1$$

where Π is the elastic potential energy and γ is Griffith's fracture surface energy. The elastic potential energy for the solid, without body forces, can be expressed as

$$\Pi = \int_V \frac{1}{2} \bar{\epsilon} \bar{E} \bar{\epsilon} dV + \int_S \bar{\sigma} \bar{n} \bar{u} dS \quad 3.2$$

where $\bar{\epsilon}$ is the strain tensor and \bar{E} the elastic properties of the solid, $\bar{\sigma}$ the stress tensor, \bar{n}

the vector normal, and \bar{u} the displacement vector. The first term of equation 3.2 is the strain energy density of the elastic solid with the crack and the second term accounts for the work done by the traction forces along the boundary S. The surface integral can be transformed to a volume integral using the divergence theorem such that the elastic potential becomes

$$\Pi = \int_V \left(\frac{1}{2} \bar{\epsilon} \bar{E} \bar{\epsilon} - \bar{u} \operatorname{div} \bar{\sigma} - \bar{\sigma} \nabla \bar{u} \right) dV \quad 3.3$$

Since $\operatorname{div} \bar{\sigma}$ are the equilibrium forces, the second term on the right is zero. The $\nabla \bar{u}$ is equal to the strain tensor, $\bar{\epsilon}$, and since $\bar{\sigma} = \bar{\epsilon} \bar{E}$, the potential energy can be written as

$$\Pi = - \int_V \frac{1}{2} \bar{\epsilon} \bar{E} \bar{\epsilon} dV \quad 3.4$$

The stability conditions can be evaluated by minimizing Gibb's potential with respect to crack extension such that

$$\frac{\partial \Psi}{\partial a} = \frac{\partial}{\partial a} \left(- \int_V \frac{1}{2} \bar{\epsilon} \bar{E} \bar{\epsilon} \right) + 2\gamma(x)_{|_{x=a}} = 0 \quad 3.5$$

Equation 3.5 is simply a restatement of Griffith's criteria for fracture where the first term on the right is the elastic energy release rate (ERR), $G(a)$, and the second term is Griffith's fracture surface energy, $\gamma(a)$. Equation 3.5 can be then written as

$$G(a) = 2\gamma(a) \quad 3.6$$

It is important to note if Griffith's criteria is achieved it does not guaranty that a catastrophic fracture will occur. Griffith's criteria can be viewed as an energy barrier which must be reached at the crack tip before propagation is possible. Once the energy barrier is exceeded slightly, catastrophic fracture will occur only if the supply of elastic

energy exceeds the dissipation rate. Sufficient conditions for catastrophic fracture, or dynamic crack extension, are established by the second derivative of Gibb's potential with respect to crack length:

$$\frac{\partial G}{\partial a} > 0 \quad \text{unstable} \quad 3.7(a)$$

$$\frac{\partial G}{\partial a} < 0 \quad \text{stable} \quad 3.7(b)$$

If equation 3.7(b) is true, sufficient energy is not available to sustain fracture and crack extension will be self-arresting, or subcritical. If $\gamma(a)$ is constant the conditions required for self-arrest will be a function of the material's elastic properties, the geometry of the test specimen, and the circumstances surrounding external traction forces.

Test configurations which are capable of generating stable crack growth provide the best opportunity for observing and modelling the fracture process. Well established test procedures for studying controlled fracture of ceramic materials are limited. Quite often these limitations relate to the inability of reliably quantifying experimental results. A completed review of available procedures revealed liabilities associated with each technique which unacceptably limited a detailed investigation of the fracture event.

Stable Crack Growth Specimens

Chevron notched specimens (Newman, 1984; Munz, 1982) displayed in figure 3.1(a) are some of the first stable test geometries introduced for fracture studies. Stable crack growth for these specimens is provided by virtue of an increasing crack front width with

crack extension. Chevron notched specimens were originally employed to evaluate the work of fracture in glass and ceramics (Nakayama, 1965; Tattersol, 1966) and it was later shown that, for materials exhibiting a constant fracture resistance, the plain strain fracture toughness could be evaluated knowing only the maximum failure load. Unfortunately, chevron notched specimens suffer several disadvantages for materials displaying a fracture resistance which increases with crack extension. The expanding crack front of the chevron notched geometry incorporates virgin material into the fracture process which is exposed to a different load history. The influence of load history is not easily quantified from recorded data (Newman, 1984).

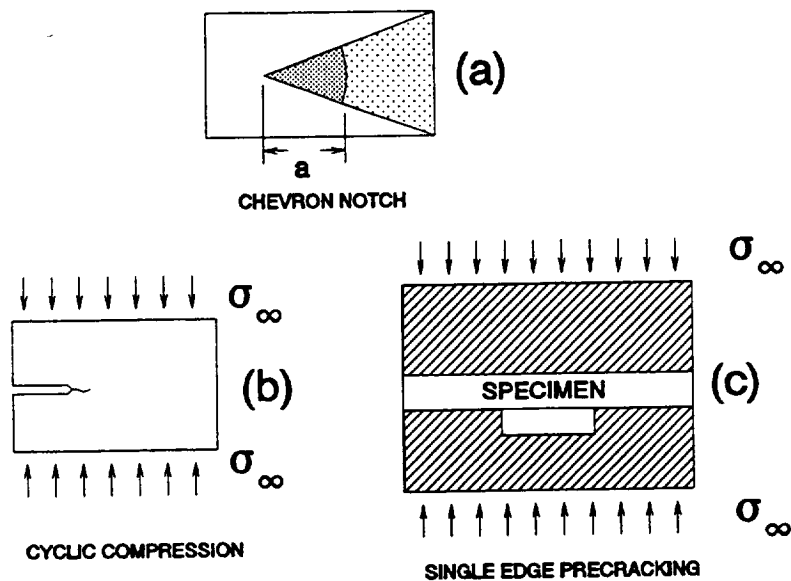


Figure 3.1: Stable crack growth specimen geometries: (a) chevron notched, (b) remote cyclic compression, and (c) single-edge precrack beam

Stable crack propagation has also been obtained by Suresh (1988) and co-workers by means of far-field cyclic compression loading of double cantilever beam type fracture specimens as shown in figure 3.1(b). Suresh has been able to stably propagate fatigue

cracks 1 to 2 millimeters in monolithic and whisker reinforced ceramics. It is suggested that crack propagation results from residual tensile stresses generated during unloading. Unfortunately, little is known about the crack growth mechanisms generated by compressive loading, and it is not known how these mechanism may relate to Mode I fracture properties. Although far field cyclic compression is an effective method for generating sharp through-thickness cracks, material near the crack tip is severely damaged in the process. Damaged material near a crack tip can strongly influence the conditions for fracture.

Nose and Fujii (1988) have developed an interesting technique for initiating sharp cracks in ceramics which they term the Single Edge Pre-cracked Beam (SEPB) method. The SEPB method shown in figure 3.1(c) is adapted to standard bend strength specimens pre-cracked with a Vicker's hardness indenter. The unique characteristic of the SEPB crack initiation technique is a stiff loading fixture which imposes a fixed curvature on the beam along the gage section (Ghosn, 1990). The nearly rigid curvature limits amount of strain energy released during extension. Once sharp through thickness cracks have been generated specimens are loaded more conventionally under three- or four-point bending for evaluation of the fracture toughness. Nose and Fujii's SEPB method has been used on several ceramic materials and has proved to be a very useful for assessing fracture toughness. The SEPB test is one of the best methods available today for measuring the critical fracture toughness of ceramic materials. However, the bend test is an inherently unstable configuration as the condition given in equation 3.7(a) is realized for all crack lengths under constant load. Thus, in the absence of increased material resistance, the only condition required for catastrophic fracture is Griffith's criteria.

STABLE SPECIMEN DEVELOPMENT

Loading Configuration

The review of available test techniques discussed above illustrated the need for developing an adequate test procedure for these studies. A displacement controlled loading system in conjunction with a specimen that had a energy release rate which decreased with crack extension, $\partial G(a)/\partial a < 0$, was considered the optimum solution for the research. With a stable specimen geometry several initiation and arrest events could be recorded for one sample which would maximize the amount of information generated. Establishing controlled crack growth could only be accomplished if the test specimen and loading configuration complied with the condition given in equation 3.7(b).

Development of a stable specimen for ceramic testing resulted in several specimen designs and loading configurations. One requirement of the loading scheme was a high degree of displacement control. This was based on an estimated 20 micrometer crack mouth opening needed to conduct a fracture test. Considering the unpredictable and sensitive nature of crack growth in brittle materials, the desired resolution for testing was two to three orders of magnitude less than the expected range. A resolution range of 0.2 to 0.02 micrometers is difficult to achieve using standard closed-loop testing machines. However, such a level of control could be obtained with a conventional test machine if a wedge loading concept was used whereby larger machine displacements would generate only small specimen displacements.

The second requirement of the loading system related to load train compliance. Machine compliance had to be low to minimize the transfer of energy to the fracture specimen during crack extension. Relying on the interaction of a closed-loop controller

to promote stability was not possible. Dynamic crack propagation rates in ceramic materials are on the order of 7 to 8 kilometers/second (km/s). The time required to fail a laboratory sized specimen with an uncracked ligament of 20 millimeters is no the order of 2 to 3 microseconds. The reaction time of conventional machine circuitry is measured in milliseconds, obviously too slow to arrest dynamic extension by unloading. Therefore, the applied displacement of a loading ram is essentially fixed during dynamic extension, although localized displacements at fixture contact points can relax and transfer energy to the specimen.

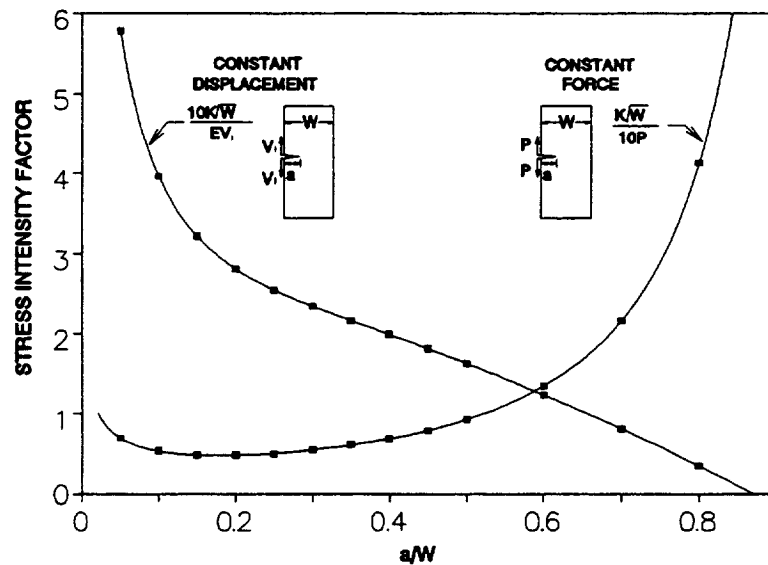


Figure 3.2: Energy release rates for constant applied mouth opening force and displacement.

It was decided that loading near the crack face would best promote stable conditions and could satisfy the practical requirements of testing. Figure 3.2 exhibits the self-arresting nature of the energy release rate function for constant force loading at the crack face. Unfortunately, the stable region is small and, at longer crack lengths, the influence of the back-face boundary produces a positively sloped ERR curve. Influence

from the back-face boundary can be minimized if the crack face is loaded as a theoretically constant displacement. The ERR solution for a constant applied displacement is also given in figure 3.2. The advantage of a constant displacement test is that, ideally, additional work is not done by external forces during crack extension when specimen compliance increases. Although fixed displacement loading improves fracture stability from a theoretical viewpoint, it will be shown that it is difficult to achieve in practice.

Controlled mouth opening displacements were applied to the first specimen configuration investigated in this study through a wedge and roller assembly as illustrated in figure 3.3. Preliminary tests were performed using a common soda-lime glass cut to the shown dimensions. Although controlled crack growth was obtained using glass and this specimen geometry, the first problem encountered was the curved crack path

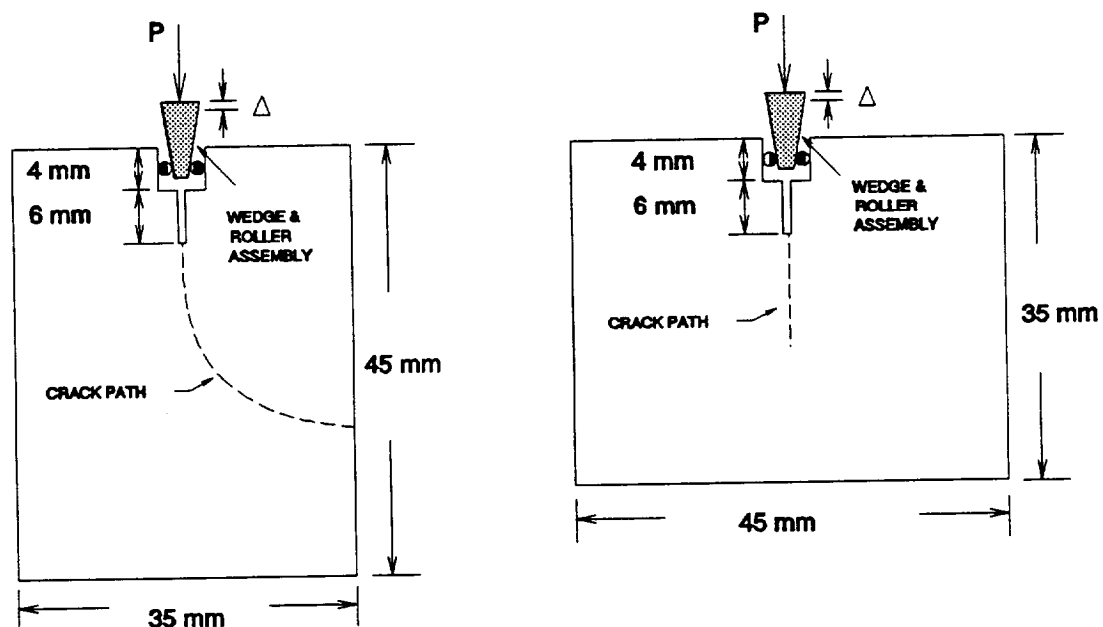


Figure 3.3: Wedge opening displacement specimen with narrow geometry and curvilinear cracking, and wide geometry with rectilinear cracking.

exhibited by the dashed line. Since side grooving has suspect influence on fracture, it had been rejected before starting the investigation, other means of forcing straight cracks, including tailoring the specimen sides and applying transverse compressive loading were attempted without success. After several unsuccessful efforts, it was argued that curved crack paths resulted from the close proximity of the specimen's side edges adjacent the crack plane. Straight propagation would occur if these side edges were farther removed such that the sample was wider. A wider sample was easily obtained by rotating the loading direction 90 degrees and keeping the overall dimension constant. A simple change in the width to height ratio of the specimen produced the straight crack path desired and it was thought that the test configuration was ready for a ceramic material.

The ceramic material selected was a commercially available Al_2O_3 excessed from other studies. The Al_2O_3 material was selected because it is easily machined and was readily available. Although stable crack growth was obtained for the glass material using the configuration shown in figure 3.3, unstable propagation was always noted for the ceramic material. Since it was assumed that crack mouth displacements were approximately fixed, reasons for unstable conditions for the ceramic were not obvious. Several changes were attempted to promote stability but none were successful. Eventually, it was thought that the loading rate was too high and a reduction may produce stable fracture. Unfortunately, unstable conditions prevailed even at crack mouth opening rates as low as $1 \mu\text{m/hr}$, it simply required more time to reach catastrophic loads.

Finally it was decided that some additional source of energy was available for fracturing the ceramic material which had been absent for the glass. The only possible

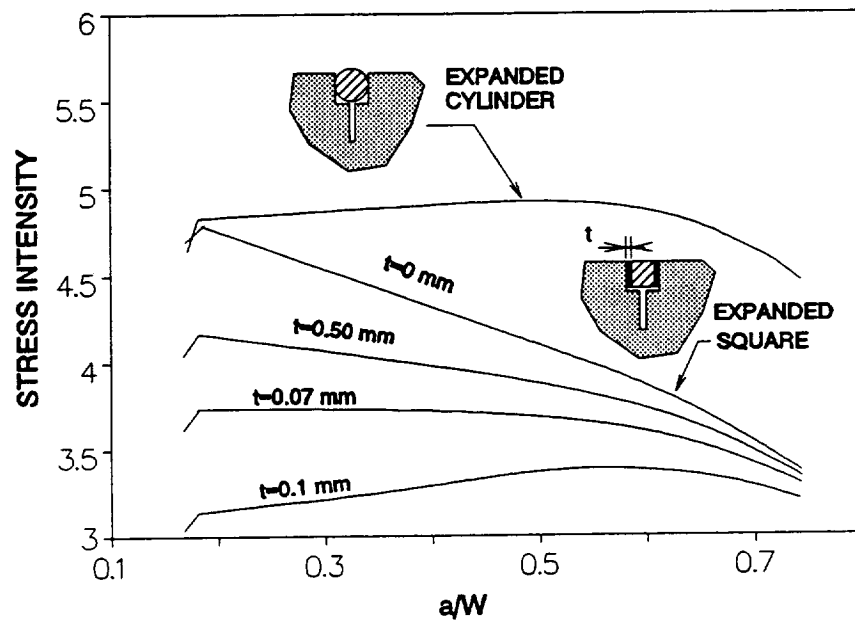


Figure 3.4: Stability of wedge opening specimen showing the influence of energy stored at contact areas. Value t is thickness of an elastic layer with modulus $E=70$ GPa.

source for additional energy capable of influencing stability would relate to the wedge and roller assembly. A re-examination of the stress solution for the entire loading configuration, including possible energy input from the roller assembly is shown in figure 3.4. These solutions revealed the very strong influence from contact compliance when testing a ceramic material. Three contact conditions were considered: a round cylinder contacting both flat surfaces of the crack mouth, a square section with its conformed surface in contact with the crack mouth, and the same square section interfaced to the crack mouth with a compliant layer. The compliant layer was used to qualitatively modeled the effects of imperfect surface conformity and the possibility of a softened response from surface asperity. A fixed isometric expansion for both the round and square solid section was used for evaluation. The elastic properties of steel were used for both solid sections and the change in their energy with crack extension was included in the ERR calculations.

Figure 3.4 demonstrates the unexpected influence contact compliance had on ERR values for the real test configuration. Although it was known that contact compliance would influence fracture behavior, its influence was particularly strong for the ceramic because the material is very stiff, its plastic deformation is minimal, and failure displacements are small. The non-linear contact compliance of the roller nearly flattens the ERR slope such that much of the benefits from fixed displacement loading at the crack mouth are removed. The modeled influence of the contact rollers on the ERR solution is conservative. In reality the load system shown in figure 3.3 has two smaller rollers, each having a softer response than one large roller. Furthermore, the two smaller rollers have four round-to-flat contact points, each having a softened response. The accentuated influence from the softer response of the real loading arrangement explains why unstable fracture conditions persisted for the ceramic material. It was learned that, although fixed displacements applied to the crack mouth optimize stability, the contact displacement at the rollers was not constant during fracture. The ERR associated with the two rollers and the steel wedge eliminated the stable condition provided by wedge loading.

The stability analysis for the first specimen was not only explanatory, it provided the insight for developing a more suitable test configuration. It was realized that the concept of isometrically expanding a solid section inside the crack mouth could produce the desired self-arresting stress field in front of an advancing crack. This expansion could be easily achieved by utilizing the Poisson displacements of a properly fitted pin when axially compressed. The ERR solution for the square section without a compliant layer in figure 3.4 best demonstrated that the transfer of external energy was minimized if the geometry of the solid section conformed to the specimen. However, the associated

compliant-layer solutions modeling surface asperity and imperfect conformity show a reduced benefit if tight machining tolerances are not maintained. For example, a negatively sloped ERR is lost if the softened response of the interface is comparable to only 50 micrometers of interface material.

Stable Poisson Loaded Specimen

Although useful for the stability analysis above, a compressed square section was not considered attractive for experiment. High machining tolerances would be necessary and the economy of conducting a fracture test was of practical concern. In addition, the Poisson expansion of a compressed square pin is not isometric, and mid-point bulging of the face would contribute to fracture instability. The problems of machinability and conformity were solved by considering a cylindrical pin axially compressed as shown in figure 3.5 for the SPL specimen. A circular loading pin and a round receiver hole in the specimen could be machined to high tolerances without significantly impacting test costs. In addition, a compressed circular pin expands isometrically and provides a self-alignment of the test specimen. Another benefit of a conformed loading pin is that contact loads are spread over a relatively large area minimizing the probability of load point failure.

The SPL loading configuration was unique in that the specimen would be attached as a secondary component to the load train. The primary component of the load train was the axially compressed section of material. The Poisson-expansion loading of a cylindrical pin also appeared to satisfy the test requirements for load system compliance and displacement control. Typical loading configurations for fracture testing link the

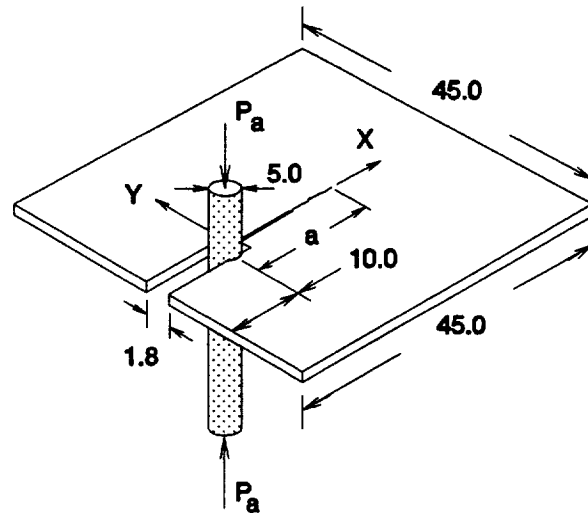


Figure 3.5: Modified Stable Poisson Loaded (SPL) specimen and loading configuration.

specimen and load train as springs in series. In such a configuration, the link with the greatest compliance, usually the test specimen, contains the greatest portion of the strain energy. A redistribution of strain energy occurs as the specimen's compliance increases with crack extension. The specimen absorbs most of the redistributed energy which can eliminate crack propagation stability. Coupling the fracture specimen in parallel with a stiff spring, i.e., an axially compressed pin, minimizes the damaging affect of redistributed energy during crack extension. For a parallel system, the component with the greatest compliance contains the least strain energy. Although an increase in specimen compliance causes an increase in the effective compliance of the parallel components, the resulting change in the distribution of strain energy is minimal compared to that for the series loading scheme. In addition, of the amount of energy that is redistributed to the parallel components, a decreasingly small amount is apportioned to the fracture specimen, as most of the energy is absorbed by further axial compression of the pin.

Another benefit of a parallel loading scheme is a high degree of control on the displacements applied to the fracture specimen. High displacement control would be realized because large changes in axial stress were needed to generate small changes in transverse displacement. Axial stresses on the pin could be controlled to less than 0.5 percent of the maximum allowable level which translated to a displacement of 50 nanometers.

NUMERICAL CALIBRATION

Model Configurations

Utilizing a parallel loading scheme also had its disadvantages, one of which related to need for calibrating experimental results. The unknown interfacial fixity (friction effects) between the load pin and the specimen complicated computational analyses and experimental evaluations. The Three-dimensional finite element analysis were performed (Ghosn,1992) to numerically calibrate experimental results. From the initial moment of considering the SPL test configuration, it was suspected that frictional forces at the pin-to-specimen interface could influence experimental evaluations. For this reason care was given to include possible frictional effects in the numerical treatment. Finite element analyses were conducted for a steel pin and a ceramic specimen. The assumed elastic properties for both materials are shown in table 3.1. A uniform axial compressive pressure was applied to the pin's cross sectional area. The stress intensity factors (SIF) and the crack mouth opening displacements (CMOD) were determined for normalized crack lengths, a/W , ranging from 0.25 to 0.90.

The three-dimensional finite element meshes used to analyze both SPL geometries

Table 3.1 Elastic Properties Assumed for Model

Model Component	Modulus, E Gpa	Poisson Ratio ν
Brittle specimen	350	0.25
Loading pin	207	0.30

are shown in figures 3.6(a), and 3.6(b). For the original configuration, the notched width was infinitely small which modeled the real 0.5 millimeter machined notch. Due to geometrical symmetry of both geometries, only half of the specimen was meshed and one element through the specimen thickness was considered. The finite element analysis utilized 20-noded isoparametric elements since they allow parabolic displacements and usually provide good solutions for both stresses and displacements (Barsoum, 1976). Mesh density near the crack tip was very high in order to accurately capture the stress singularity.

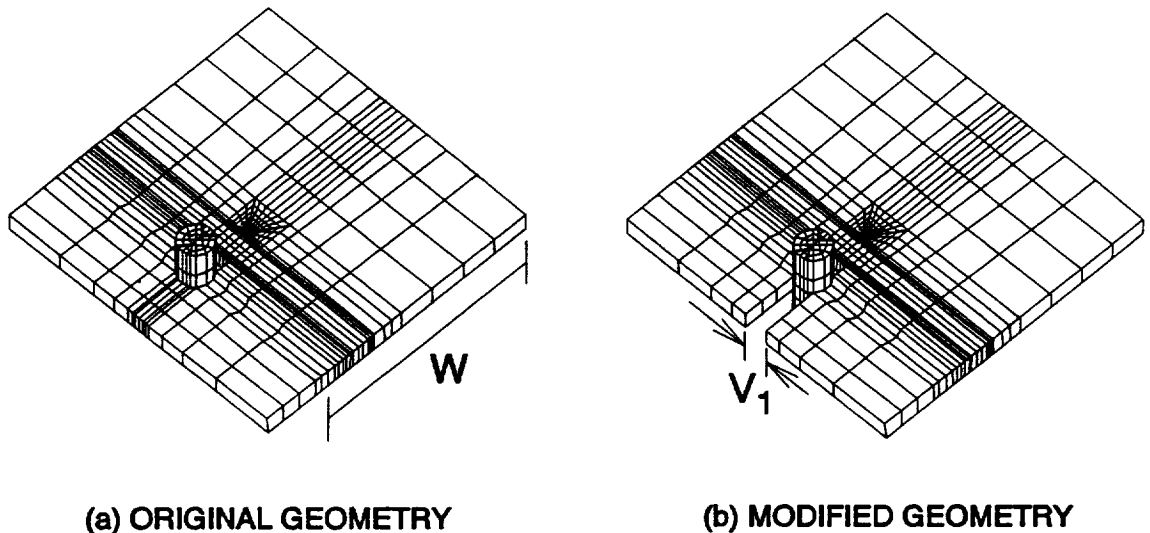


Figure 3.6: Finite element meshes used to analyze (a) the original SPL and (b) modified SPL specimen geometries.

Due to the uncertainty of the contact condition between the steel pin and the specimen, the stress analysis was conducted with different sets of constraints imposed along the interface of the two materials. To facilitate implementation of different boundary conditions, nodes along the contacting interface were duplicated: one set of nodes was associated with specimen elements, and a second matching set was associated with pin elements. These duplicate sets of nodes permitted sliding at the pin-to-specimen boundary such that interfacial friction effects could be estimated. The MARC (MARC,1990) general purpose finite element program used provided a gap-link element which modelled separation or contact between the two bodies depending on the resulting forces. If the force was tensile, the link provided for separation of the two bodies and no force was transmitted. If the force was compressive the gap closed and a frictional shear would be present. Only Coulomb frictional effects were considered where the magnitude of the shear force is linearly proportional to the normal force through a friction coefficient, μ .

Contact between the specimen and pin was modeled with several different specimen-to-pin boundary conditions and three of them, termed free, fixed and friction, will be discussed. The 'free' case was the simplest analysis where only one node at the center of the pin-to-specimen interface was connected. The 'fixed' results were generated when a radial tying boundary condition was implemented where only the radial degree of freedom for each pair of nodes along the pin-to-specimen interface were joined. The gap-link elements were used for the friction analysis with and without a Coulomb coefficient ($\mu=0.4$). Since totally fixed or free interface conditions are not realistic, the friction solution was used to evaluate experimental data. The magnitude of the Coulomb

coefficient was selected as the best measure of real contact conditions between the ceramic specimen and the steel pin. Other details of the FEM analysis for both the original and modified SPL geometry were reported by Ghosn, Calomino and Brewer (1992).

Load Transfer to Specimen

The load transferred to the specimen from the pin's radial expansion was calculated by summing nodal reaction forces in the Y-direction along the symmetry plane of the pin (the $Y=0$ plane of the pin in figure 3.6). The ratio of the load transferred to the specimen, P_{sp} , to the applied pin load, P_a , is shown in figure 3.7 as a function of the normalized crack length for each contact boundary condition. The data displayed is

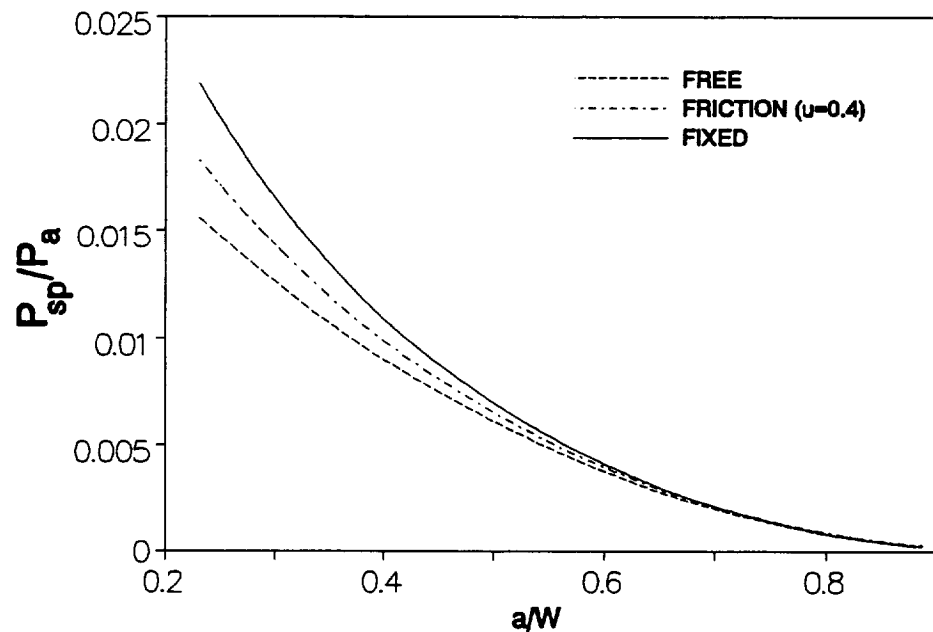


Figure 3.7: Ratio of the load transferred to the specimen over the applied pin load (P_{sp}/P_a) for modified SPL specimen.

limited to the modified SPL specimen as this represents the more practical test geometry. All contact conditions reveal decreasing transferred loads with increasing crack length for a given applied compressive load demonstrating the fracture stability of the SPL concept. The decreasing trend in transferred load was consistent with increasing specimen compliance.

Stress Intensity Factor

The stress intensity factors for the modified specimen for the free contact case are given in table 3.2 as a function of crack length. Listed in table 3.2 are the results of three techniques used to calculate SIF values: the J-integral method, the crack opening displacement in the singular element immediately adjacent to the crack tip, and finally the compliance method. The SIF determined by the J-integral approach were calculated from the change in strain energy due to a small perturbation of the nodes around the crack tip. The compliance method for calculating SIF values used the change in work done by the external force with increasing crack length.

As seen in table 3.2, the variation in the normalized SIF between the J-integral and the displacement methods was less than 4 percent for a normalized crack length ranging from 0.4 to 0.9. For the shorter crack lengths the difference increased to 9.7 percent. Comparing the J-integral approach to the compliance method, the difference in the SIF was less than 4% for a/W ratios between 0.30 to 0.80. At a larger crack length, $a/W=0.85$, the difference increased to 9.6 percent. These results are presented to show that the variation between the numerically determined SIF values from three different methods was within 6% for a/W values ranging from 0.3 to 0.8 which demonstrated a

Table 3.2 Stress Intensity Factors Modified SPL Specimen

Normalized crack length	Stress Intensity Factor (friction)				
	a/W	J-Integral	Displacement	Compliance	
0.25		5.351	4.833	-9.7%*	-
0.30		5.905	5.565	-5.7%	5.749
0.35		6.579	6.202	-5.7%	6.411
0.40		7.412	7.181	-3.7%	7.233
0.45		8.460	8.327	-1.6%	8.269
0.50		9.807	9.744	-0.6%	9.605
0.55		11.577	11.565	-0.1%	11.372
0.60		13.973	13.998	0.2%	13.777
0.65		17.320	17.367	0.3%	17.350
0.70		22.201	22.238	0.2%	22.190
0.75		29.737	29.693	-0.1%	30.017
0.80		42.370	42.036	-0.8%	43.977
0.85		66.461	65.141	-2.0%	72.825
0.90		123.978	119.415	-3.7%	-

confidence in the calibration results for this range. Discrepancies at longer and shorter crack lengths were attributed to sharp displacement gradients and free edge effects, respectively. Since the J-integral method has proven to be highly accurate even with a coarse mesh (MARC,1990), it was the preferred method for computing the SIF values for both SPL geometries and contact conditions. These reported SIF values plotted in figure 3.8 are normalized with respect to the load transferred to the specimen P_{π} and only evaluated from the J-integral approach. Also shown in the figure is the SIF results for the compact tension specimen (ASTM E399, 1992). The comparison is appropriate since the present specimen is very similar to the compact tension specimen. The

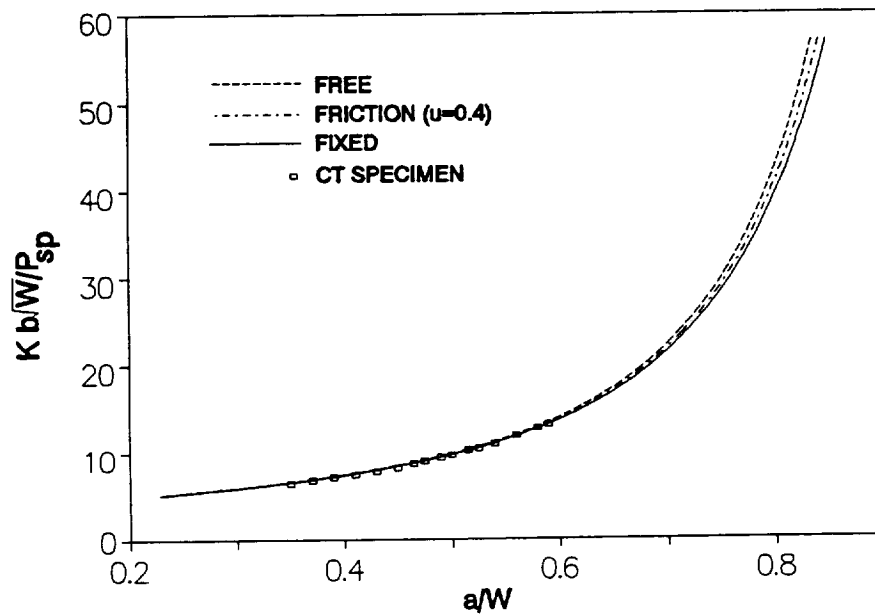


Figure 3.8: Normalized stress intensity factors with respect to specimen force (P_{sp}) as a function of crack length.

excellent agreement between the present analysis and the compact tension specimen gave a greater confidence of the numerical results.

Since the load transferred to the specimen from the pin cannot be measured experimentally, the SIF were normalized with respect to the specimen modulus E_c and the CMOD, V_1 , and plotted again in figures 3.9(a) and 3.9(b) for the modified and the original SPL specimen, respectively. Under constant applied pin load, stress intensity factors dropped off sharply with increasing crack lengths for both specimen geometries.

In the test range of $a/W=0.3$ to 0.8 stress intensity factors reduced nearly 75 percent making the SPL specimen geometry attractive for fracture toughness testing of high elastic modulus materials. The variation in the SIF evaluated for the three contact cases considered was much smaller for the modified SPL geometry than the original geometry

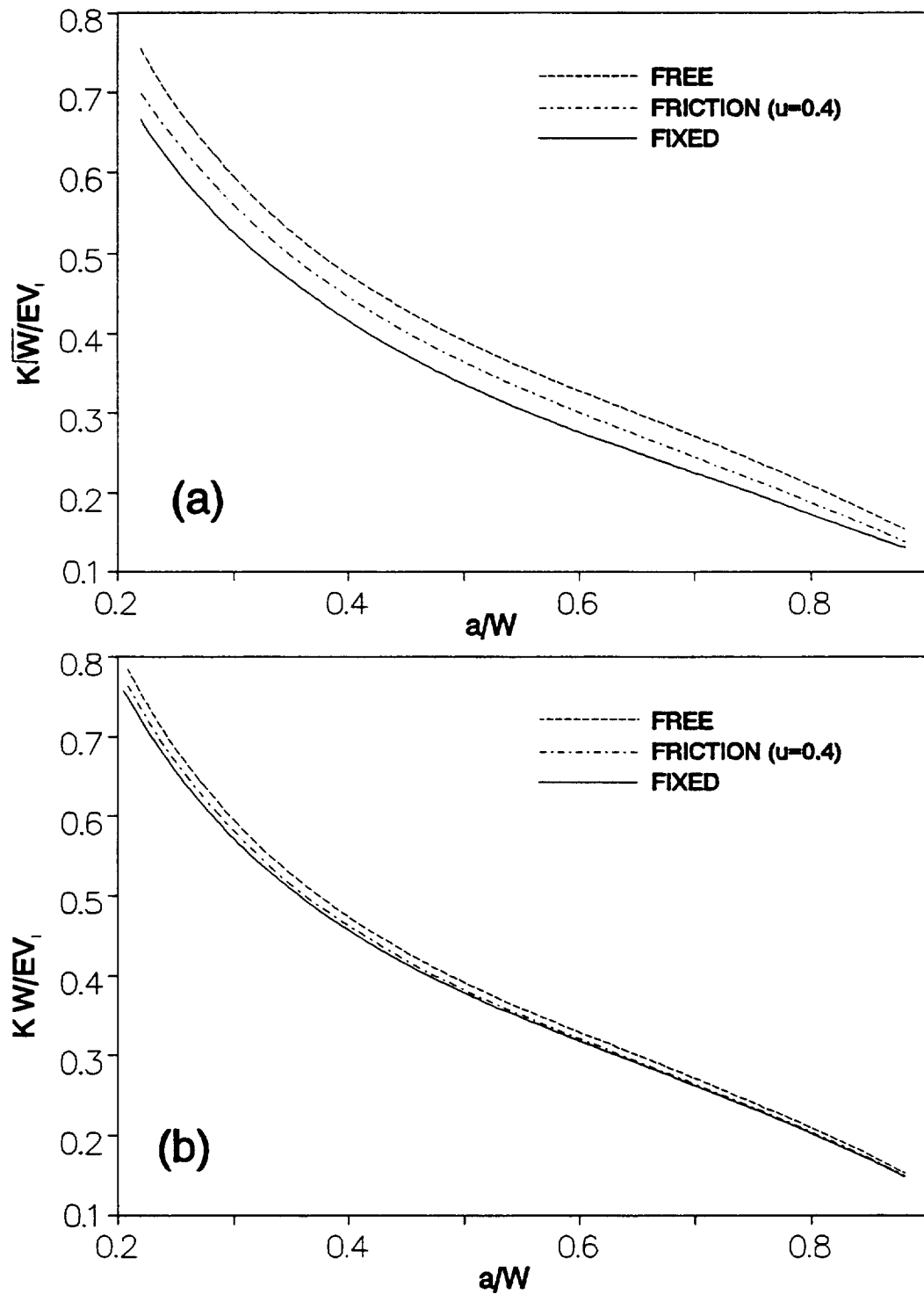


Figure 3.9: Normalized stress intensity factors with respect to the CMOD (V_1) for (a) the original, and (b) the modified SPL specimen.

particularly at smaller crack lengths. When the notched width was small, the specimen introduced additional constraints at the pin-to-specimen interface. These constraints have their largest effect at smaller crack lengths because of the close proximity of the crack tip and loading pin. Variation of SIF values for the original specimen between fixed and free conditions was attributed to the unexpected variation in experimental fracture toughness measurements discussed below.

Table 3.3 Numerical Calibration of Modified SPL specimen
(coulomb friction $\mu=0.4$)

$\frac{a}{W}$	$\frac{V_1}{V_2}$	$\frac{P_{sp}}{P_a}$	$\frac{E_c V_1 b}{2P_{sp}}$	$\frac{E_c V_2 b}{2P_{sp}}$	$\frac{K_I b \sqrt{W}}{P_{sp}}$	$\frac{K_{II} \sqrt{W}}{2E_c V_1}$
0.25	4.082	1.17E-2	7.98	1.96	5.334	0.6684
0.30	3.128	1.43E-2	10.12	3.23	5.881	0.5814
0.35	2.727	1.19E-2	11.49	4.21	5.916	0.5148
0.40	2.491	9.85E-2	15.93	6.40	7.359	0.4619
0.45	2.329	8.06E-3	20.03	8.60	8.382	0.1485
0.50	2.206	6.51E-3	25.38	11.51	9.690	0.3817
0.55	2.108	5.15E-3	32.62	15.48	11.403	0.3495
0.60	2.026	3.98E-3	42.81	21.13	13.702	0.3201
0.65	1.956	2.97E-3	57.82	29.56	16.883	0.2920
0.70	1.896	2.13E-3	81.23	42.84	21.444	0.2640
0.75	1.844	1.44E-3	120.35	65.27	28.299	0.2351
0.80	1.798	9.07E-3	191.84	106.67	39.251	0.2046
0.85	1.759	5.13E-3	338.92	192.71	58.208	0.1717
0.90	1.724	2.50E-3	693.26	402.14	93.892	0.1354

The modified specimen with a larger machined notch width and, hence, a smaller contacting area gave more consistent fracture toughness results both experimentally and analytically. In addition the analytical results for the modified SPL geometry revealed little influence from pin constraint provided the crack mouth opening displacements were

used to calculate fracture toughness values. The analytical results needed for treatment of experimental data using the modified geometry of the SPL specimen are given in table 3.3. These are presented for the Coulomb friction case ($\mu=0.4$) using the gap-element option of MARC. The friction solution was considered the most realistic simulation of the actual contacting condition. Considering the small change of analytical SIF values from fixed to total free conditions, any small variation in the actual contact condition at the pin-to-specimen interface would have little influence on fracture toughness evaluations. Table 3.4 provides best fit equations for the results presented in table 3.3 and can be used for experimental applications.

EXPERIMENTAL EVALUATIONS

General Procedure

The detailed influence of the contact compliance on fracture conditions was not predictable analytically, thus stability needed to be confirmed experimentally. The overall dimensions of the specimen were limited by the size of available bulk ceramic material which was 40 mm wide, 50 mm long and 10 mm thick. Specimens were to be loaded through displacements applied to the crack mouth from an axially compressed cylindrical pin. The initial SPL geometry shown in figure 3.5 was selected because it had advantages for both machining cost and numerical treatment. It was later found that friction at the pin-to-specimen interface influenced fracture toughness measurements and the modified geometry's wider crack mouth was necessary to minimize friction effects.

Two types of monolithic, hot pressed ceramic materials were tested: Norton NC-132 silicon nitride, Si_3N_4 , and Coors' AD-995 aluminum oxide, Al_2O_3 . Both materials

Table 3.4 Curve Fits of SIF and COD for Modified SPL
(coulomb friction, $\mu=0.4$)

$\frac{V_1}{V_2} = \frac{2.9225 - 16.0472\left(\frac{a}{W}\right) - 18.8965\left(\frac{a}{W}\right)^2}{1 - 1.5373\left(\frac{a}{W}\right) - 18.7505\left(\frac{a}{W}\right)^2}$
$\frac{P_{sp}}{P_a} = \frac{0.01722 - 0.04368\left(\frac{a}{W}\right) + 0.02391\left(\frac{a}{W}\right)^2}{+ 0.002821\left(\frac{a}{W}\right) - 0.0001230\left(\frac{a}{W}\right)^2}$
$\frac{E_c V_1 b}{2P_{sp}} = \frac{1.7782 + 12.0723\left(\frac{a}{W}\right) - 7.0620\left(\frac{a}{W}\right)^2}{1. - 2.0439\left(\frac{a}{W}\right) + 1.0488\left(\frac{a}{W}\right)^2}$
$\frac{E_c V_2 b}{2P_{sp}} = \frac{-1.3638 + 11.4968\left(\frac{a}{W}\right) - 6.75930\left(\frac{a}{W}\right)^2}{1. - 2.0674\left(\frac{a}{W}\right) + 1.0733\left(\frac{a}{W}\right)^2}$
$\frac{K_I b \sqrt{W}}{P_{sp}} = -3.1674 - 9.2761 \sqrt{\left(\frac{a}{W}\right)} \ln\left(\frac{a}{W}\right) - 11.2990 \frac{\left(\frac{a}{W}\right)}{\ln\left(\frac{a}{W}\right)}$
$\frac{K_{II} \sqrt{W}}{2E_c V_1} = \frac{1.5012 - 5.2140\left(\frac{a}{W}\right) + 9.4063\left(\frac{a}{W}\right)^2}{- 8.2054\left(\frac{a}{W}\right)^3 + 2.5760\left(\frac{a}{W}\right)^4}$

are commercially available and have an extensive history of experimental testing. Specific material properties, obtained from the manufacturers can be found in table 3.5.

Table 3.5 Physical Properties of Material

MATERIAL	ELASTIC MODULUS	POISSON'S RATIO	AVERAGE GRAIN SIZE
AD-995	370 GPa	0.20	2.0 μm
NC-132	320 GPa	0.28	1.0 μm

Both the original and modified SPL geometries were machined from a bulk billet such that the direction of crack propagation would be perpendicular to the direction of hot pressing. The load pin contact area was machined with a diamond coring bit and surfaced with diamond grinding mandrel. Significant attention was devoted to establishing the perpendicularity and cylindricity of the hole. A chevron notch was cut in the specimen with a diamond wafering saw to create a pre-cracking notch. Specimens were polished to a 1 micrometer microstructural finish. This level of finish was necessary to accurately track the crack propagation optically. A succession of diamond slurry abrasive was used with a free abrasive lapping type machine to polish the specimens.

Displacement controlled testing was achieved by loading a hardened steel pin in compression. Load pins are sized for each test case because of variations in machining tolerance of the receiver hole. The proper sized load pin was selected from a set of pins, each diamond ground to step size increments of 2.5 micrometers. The maximum

allowable axial pin stress was 110 MPa, which produced an available maximum displacement of 8.0 micrometers. Since this maximum displacement is not sufficient to propagate a crack, slightly oversized pins were chosen to apply approximately a 5.0 micrometer initial offset displacement prior to testing.

The loading pins were pressed into the specimens manually with the aide of a simple alignment jig and press. The pin size was selected such that no cracking occurred prior to loading. Crack mouth opening displacements were monitored with a extensometer during the pin installation to obtain an accurate opening offset prior to testing. Since CMOD is used to calculate fracture properties accurate offset opening measurements were necessary for computations.

All tests were conducted at room temperature in an ambient environment. Testing was accomplished by monotonically loading the pins in compression. Loading was increased monotonically regardless of the observed rate of crack extension. CMOD measurements were made with a small commercial extensometer with a gage length of 6.35 millimeters. Axial pin load and CMOD measurements were recorded on an X-Y plotter, as well as on an analog FM tape recorder together with a voice record.

Crack Length Measurements

Developing a method of continuously measuring the crack length as it stably propagates through the material was an additional requirement for the testing technique. At first, optical methods of monitoring crack length were not considered attractive because they were cumbersome, the equipment needed was not available, and results were subject to the observer's talents. Although widely used for conventional fracture

studies, compliance calculations using crack mouth force, P_m , and displacement, V_1 , could not be used to estimate crack length since the force could not be measured. Other compliance based methods, including strain gaging and double compliance techniques were considered. Unfortunately, strain gaging each test specimen added to the cost and complexity of the test procedure. Using a double compliance technique similar to the E-561 standard (ASTM E561, 1992) were tried but the second displacement measurement, V_2 , in front of the load pin was spurious and results were not consistent. Inaccurate measurements for the second displacement related to inadequate instrumentation. Commercially available displacement gages were not well suited for obtaining the second displacement reading and developing an acceptable gage exceeded the scope of these studies.

Significant research time was given to developing the electrical potential drop (EDP) technique. The EDP method is a commonly accepted and very accurate approach for measuring crack growth in metals, and it has been used for ceramics (Dauskardt, 1987). The EDP method takes advantage of the equi-potential flow patterns generated when a current is passed through a conductor with a discontinuity, usually a fracture specimen. If the applied current is constant, the voltage drop between two points on either side of a crack can be accurately correlated with crack length. Since this technique requires some measure of electrical conductivity, a thin metallic film is adhered to the specimen surface for most ceramics.

Application of the EDP technique with the SPL specimen produced poor results. The coating material and technique used were based on the work of Dauskardt (1987) and involved sputter deposition of a 500-angstrom thick film of a chrome-nickel alloy on

the smooth polished surface of the specimen. Using the same alloy and sputtering conditions, a conductive grid system shown in figure 3.10 was placed on the opposite

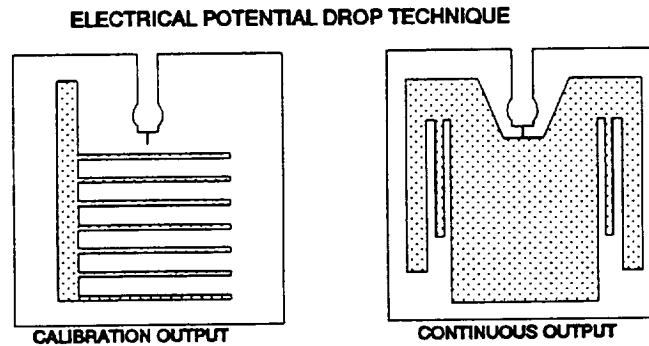


Figure 3.10: Electrical potential drop technique for measuring crack length by sputter depositing a thin (100 Å) metallic film (chrome-nickel alloy).

side for calibration. It was thought that the loss of electrical resistance in each grid would mark the position of the crack tip. Unfortunately experimental results were very inconsistent as quite often some grids would continue to carry current even though optical techniques revealed that the crack had passed their position. It was even noted that the optical crack tip position could be 2 millimeters ahead of a conductive grid before its conductivity was lost. In other cases it was observed that grids closer to the optical crack tip had lost their continuity while those farther away, or earlier broken, continued to carry a voltage. Since the loss in grid conductivity was spurious, no attempt was made to quantify results. The continuous film results were equally peculiar. Although overall voltage increased with crack length, there were points in the record where the measured voltage suddenly decreased which could not be explained by fluctuations in the controlling current. Such results could be interpreted as 'crack healing' but this would be an incorrect conclusion because crack opening displacements increased monotonically.

Modifications of the EPD technique included smaller grid widths, thinner film

thicknesses, and lower currents, however, results remained suspect. Finally, scanning electron microscopy of fractured grids which still conducted provided a reason for the poor performance of the EDP technique. The SEM micrograph shown in figure 3.11 demonstrates that grain bridging, or other similar mechanisms, provide a unbroken link for the conductive film. Since grain bridging occurs randomly along the crack path, it is not surprising that grids near the crack tip lost their conductivity while grids farther away continued to conduct. These conductive links also explain results for the continuous film where a 'crack healing' behavior was observed since rotation of a grain along the crack face could reconnect a conductive bridge.

After much time and effort, the EDP technique was abandoned and replaced with an optical technique which had become mature enough to be used. Crack lengths could be optically measured during the test with a traveling microscope shown in figure 3.12. Optical data was also recorded on VHS format video tape for later analysis and calibration.

Data recorded on analog tape was digitized during playback after the tests. The rate of digitization varied from 2 to 40 hertz. Digitization was conducted on a laboratory PC and data files stored magnetically. The digital data was correlated with optical crack length measurements from voice records. Representative experimental applied pin load and CMOD measurements versus crack length are shown in figure 3.13.

Original SPL Performance

Typical fracture properties, computed from the stress analysis of the original SPL specimen, are shown in figure 3.14 for both the Coors' AD-995 Al_2O_3 and Norton NC-

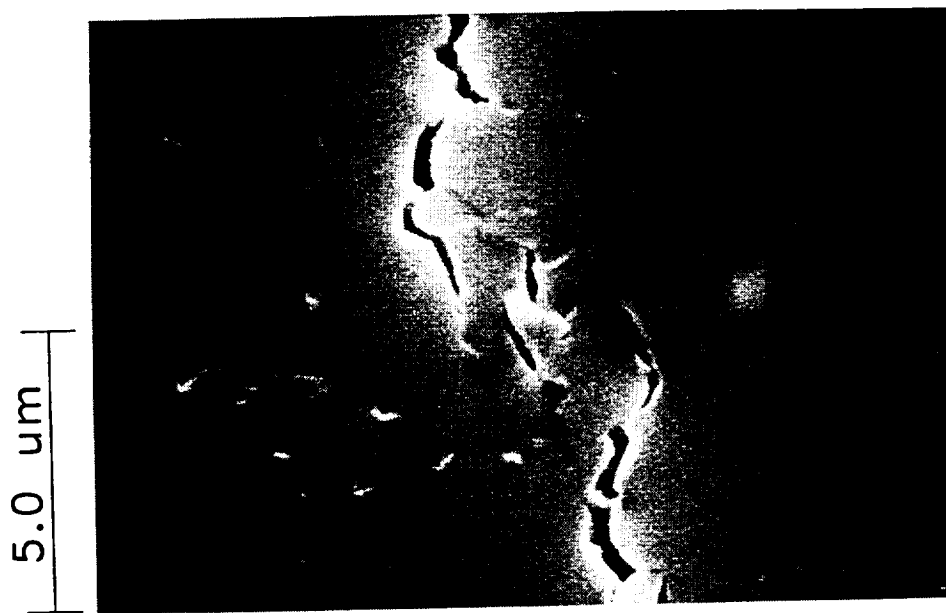


Figure 3.11: Electron micrographs of bridged electrical contacts due to grain rotation of substrate and plastic deformation of metallic film.

132 Si_3N_4 materials. In both cases, the critical stress intensity factors were computed to decrease with crack extension. Crack growth in the Al_2O_3 material remained subcritical

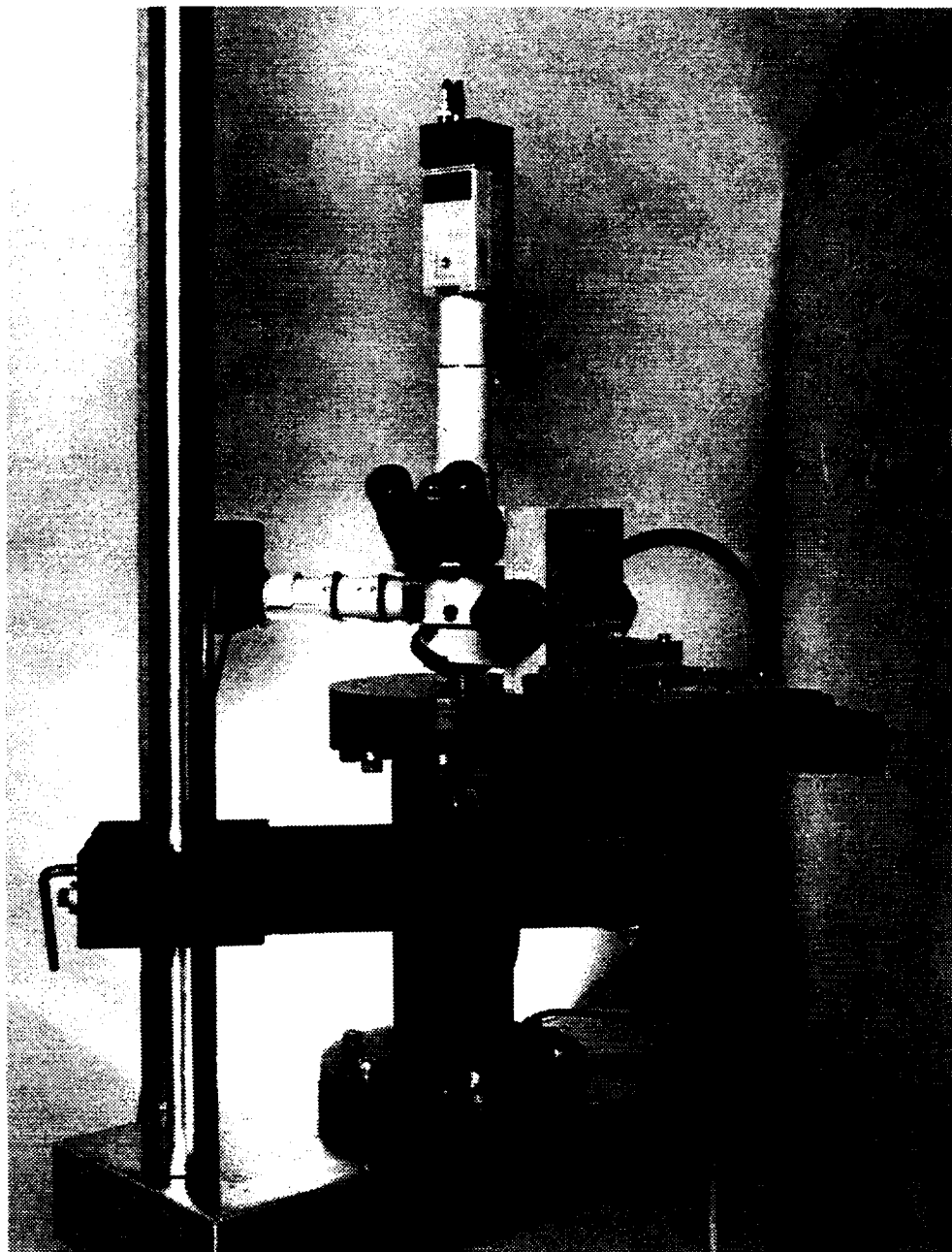


Figure 3.12: Traveling microscope and load frame for the SPL test procedure.

throughout the test. Since a sharp increase in crack velocity was not observed, a unique value for K_{Ic} could not be computed.

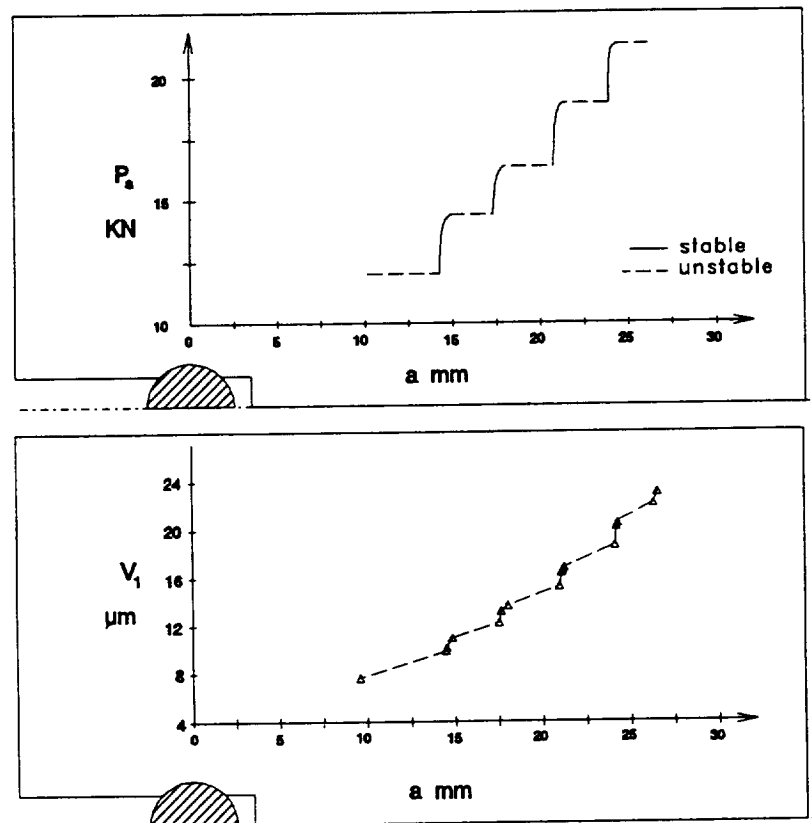


Figure 3.13: Experimental measurement of pin load and crack mouth opening displacement versus crack length for the NC-132 material.

Considering the susceptibility of Al_2O_3 to stress corrosion cracking and the relatively slow rate of loading, continuous subcritical growth was not surprising. However, the material displayed a disturbing trend of decreasing fracture resistance with increasing crack growth. It was noted that such a result was in direct contrast with a large body of experimental evidence suggesting the Al_2O_3 material had an increasing or, at best, constant fracture resistance. It was suggested that the decreasing trend could be related to stress corrosion cracking, however, other experimental behavior did not support such an effect. For example, crack velocities in the alumina were observed to increase shortly after initiation even though measured fracture properties decreased.

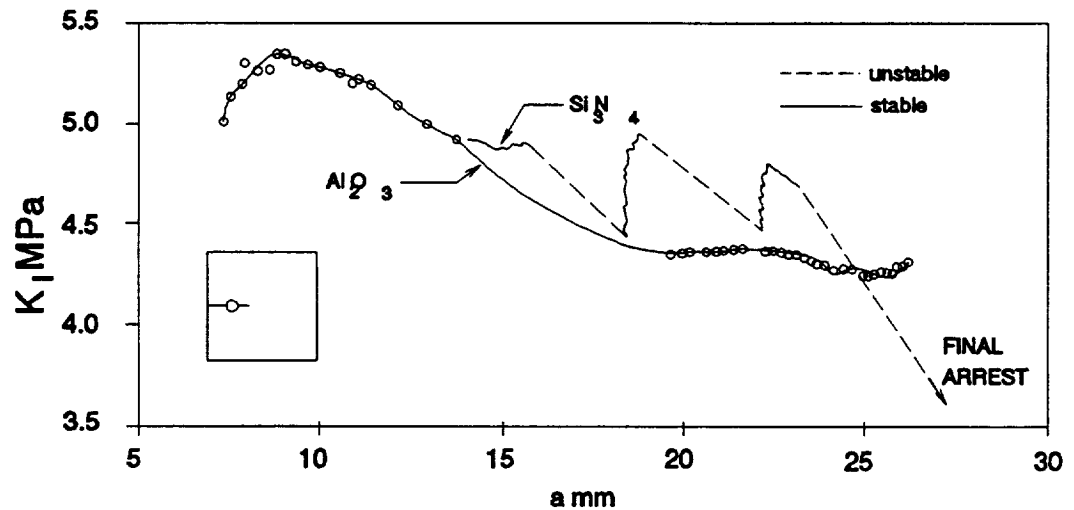


Figure 3.14: Original SPL test data revealing the measured decreasing fracture resistance produced by interface friction at the pin contact area.

Increasing crack velocities reduces the reaction time available for stress corrosion and one expects an associated increase in the fracture resistance. It was suspected therefore that the influence of the pin-specimen friction was not well understood or modeled.

It was decided that an investigation of the test specimen and stress model could be accomplished by employing a well tested material which is known to have little or no stress corrosion effect. For this reason, test samples of Norton NC-132 Si_3N_4 material were machined and tested. The results of this test are also displayed in figure 3.14. Similar to the Al_2O_3 tests, computed stress intensity factors for the Si_3N_4 material displayed a decreasing trend with increased crack extension.

One interesting difference noted with the Si_3N_4 material compared to the Al_2O_3 material was a discontinuity in crack propagation rates. As the applied load was increased, subcritical crack extension was observed to occur at an increasing rate. The crack propagation rate increased gradually up to a point of instability. An abrupt change in the propagation rate was observed which resulted in a 'jump' in crack extension.

Crack extension was then arrested within the specimen due to the decreasing stress intensity field of the specimen. The unstable portions of crack advance are shown in figure 3.14 as dashed lines. The sequence of subcritical extension leading into unstable propagation was repeated several times in one specimen. The average amount of subcritical extension was 0.5 mm and the average amount of unstable extension was approximately 2 to 3 millimeters for each fracture event

The decrease in critical fracture properties for a material known to show little stress corrosion behavior supported the idea that the effects of pin loading were not clearly understood or properly modeled. Stress analyses had revealed that the degree of fixity between the load pin and the specimen would affect the computation of fracture properties. Pin contact friction would be greatest at shorter crack lengths when specimen compliance is lowest. Examination of the stress analysis for the original SPL geometry suggested that higher frictional forces at shorter crack lengths could artificially produce high fracture toughness.

A negative change in fracture properties was consistent with the argument of relatively high constraint at short crack lengths and lower constraint at longer crack lengths. Frictional forces were greatest where pin constraint was greatest. Referring to figure 3.15, large constraints are generated in regions where the horizontal component of the pin's radial expansion is greater than the vertical or opening component. It was argued that removal of this material would minimize interfacial friction effects. The disadvantage of removing material at the crack mouth for the modified geometry were increased localized deformations and increased stored energy at the contact interface. Figure 3.4 clearly demonstrated how damaging the energy stored at the pin contact points

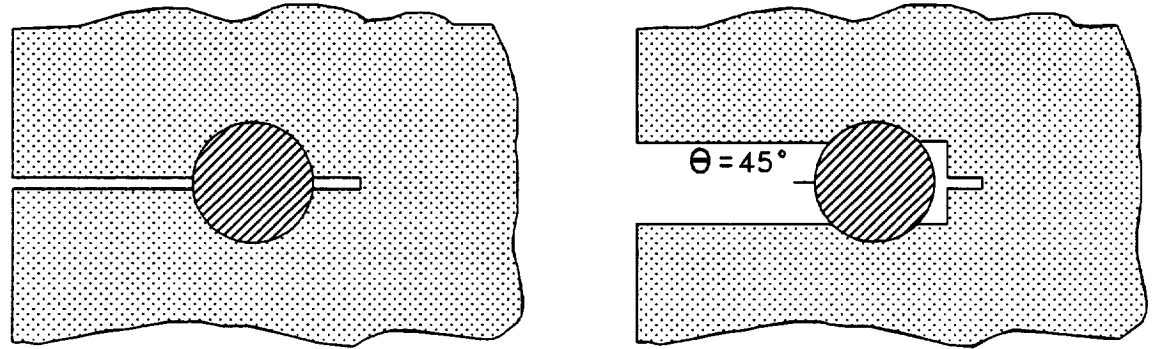


Figure 3.15: Pin to specimen contact area showing the pin's expansion constraint for angles less than 45° .

can be on fracture stability.

Modified SPL Performance

As discussed the numerical treatment for the modified geometry confirmed a reduced influence from friction as expected. Still, due to the unpredictable nature of the contact interface, experimental verification of fracture stability was needed. Both the AD-995 and NC-132 materials again were tested using the modified specimen geometry and the results are shown in figure 3.16. As with the original SPL geometry, subcritical crack extension was observed to occur throughout the test with the Al_2O_3 material where the crack was extended from a depth of 10.55 to 24.5 millimeters. The computed fracture resistance curve for the Al_2O_3 material increased slightly throughout the test. Unstable crack extension was not observed, thus a value for K_{Ic} could not be computed. However, measured stress intensity factors were observed to increase from $4.2 \text{ MPa}\sqrt{\text{m}}$

at a crack length of 10.5 millimeter to $4.8 \text{ MPa}\sqrt{\text{m}}$ at a crack length of 24.5 millimeter. This increasing trend in the fracture toughness for alumina is consistent with reported behavior of the material. These computed values for the fracture strength were slightly greater than values reported in the literature (Depoorter, 1990).

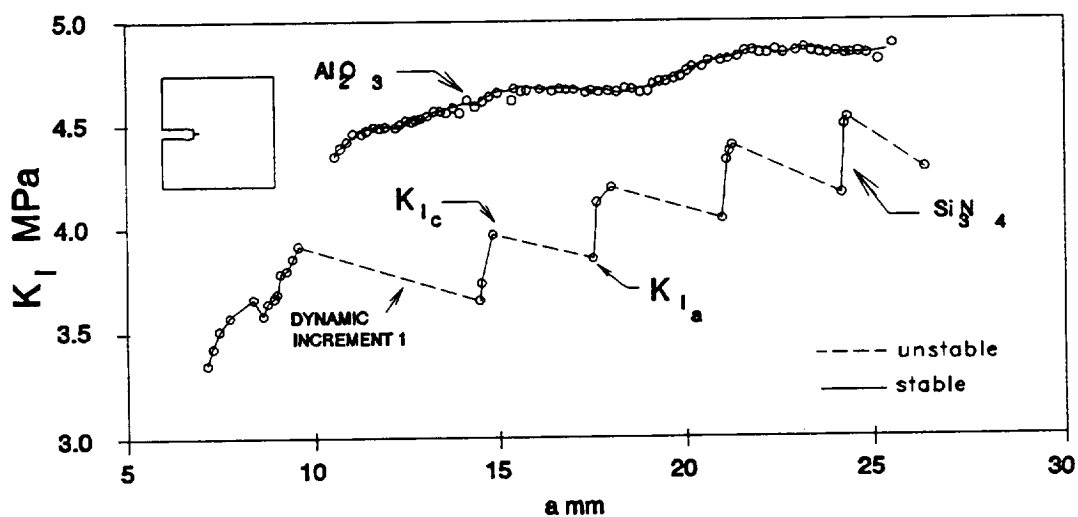


Figure 3.16: Modified SPL test data revealing the minimized influence of interface friction at the pin contact area.

Tests conducted with the modified test specimen on the Norton material exhibited a behavior similar to the original SPL specimen. The subcritical crack growth rate was observed to accelerate with increased pin load up to instability, as before. The length of subcritical extension averaged approximately 0.5 millimeter and unstable 'jumps' in crack growth were an average of 2 millimeters. Critical stress intensity factors increased from a low of $3.8 \text{ MPa}\sqrt{\text{m}}$ to $4.6 \text{ MPa}\sqrt{\text{m}}$ with the crack achieving a length 28 millimeters at the final arrest. Computed values for K_{Ic} and K_{Ia} are given in table 3.6 together with the length of the unstable jump preceding each crack arrest.

Table 3.6

Table VI Fracture Properties of NC-132

DYNAMIC INCREMENT	STRESS INTENSITY MPa√M		INCREMENT LENGTH mm
	INITIATION	ARREST	
1	3.9	3.7	4.7
2	4.0	3.9	2.4
3	4.2	4.0	2.8
4	4.4	4.2	2.6
5	4.5	4.3	1.9

SUMMARY

The modified specimen geometry was tested to investigate the specimen stability assumptions. From the stress analysis results shown in figure 3.9(a) the modification produced its most profound effect at shorter crack lengths, when compared to the stress analysis of the initial geometry given in figure 3.9(b). It is interesting to note that although the enlarged mouth opening did not appreciably change observed material behavior, the trend of computed fracture toughness with crack length changed considerably for both materials. This observation highlights the need to accurately model the influence of constraining forces at the loading pin for the stability analysis of a loading configuration.

The ability to observe and measure multiple fracture events for the NC-132 silicon nitride material demonstrates the unique abilities of the SPL specimen for conducting detailed fracture studies of brittle, highly stiff materials. Although the NC-132 material has not been reported to have an increasing fracture resistance, these controlled crack studies revealed that measured stress intensity factors systematically increased 10 to 20

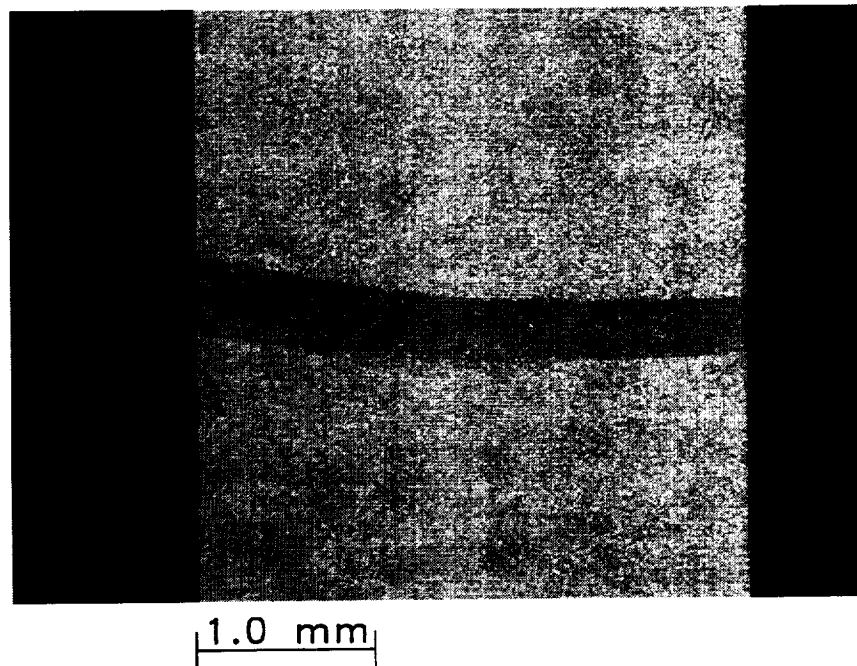


Figure 3.17: Optical contrast band generated on the fracture surface during increments of subcritical crack extension.

percent during subcritical extension. Also interesting for the NC-132 material were bands on the fracture surface which correlated with lengths of subcritical and dynamic crack extension. These bands were easily observed optically and an example is given in figure 3.17. Based on these results, it was decided that the NC-132 would be an excellent model material for a more detailed investigation of brittle fracture.

CHAPTER IV

Fracture Response of NC-132 Silicon Nitride

INTRODUCTION

Preliminary tests of the NC-132 material used to develop the SPL specimen and test procedure demonstrated that dynamic crack extension occurred after measurable increments of slow crack growth. These tests also indicated that increments of slow crack growth were associated with measurable increases in the material's fracture resistance prior to dynamic initiation. Based on these observations, it was decided that an experimental examination of the brittle fracture behavior of the NC-132 material could be used to study how subcritical failure events influence catastrophic fracture. The objectives of the experimental program were to identify crack growth resistance mechanisms of the ceramic and understand how subcritical crack growth affects critical fracture conditions. Identifying the characteristics of the fracture process which are material specific from those that relate to the process itself is considered key to developing a fracture model for general application. To this end, fractography studies of both the subcritical and dynamic crack growth increments were conducted and the results compared. The outcome of these studies suggests that fracture in the NC-132 incorporates a volume of material at the crack tip during subcritical growth. Furthermore, increments of subcritical crack growth permanently alter fracture surface morphology suggesting that a distinct change in the fracture process occurs between subcritical and dynamic conditions even though both involve intergranular fracture. The

experimental study was limited to the room temperature performance of the NC-132 material under static loading conditions.

EXPERIMENTAL PROCEDURES

The SPL specimen and loading technique were selected because of the ability to produce multiple events of slow crack growth, dynamic initiation, and arrest. The modified geometry with a large notch width was used to insure minimal influence from interfacial friction effects at the pin-to-specimen contact point. Specimens were machined to the planar dimension shown in figure 3.5. Two sets of specimen configurations were tested, one having a thickness of 1.0 mm and the other 3.0 mm. The change in specimen thickness was examined for possible influence from thickness affects in fracture property measurements.

Material

The amount of NC-132 material acquired for preliminary study while developing the SPL specimen was not ample for a more detailed fracture investigation. In addition, the material was estimated to be a number of years old and the batch identification number could not be obtained so processing information was lost. For this reason a new batch of NC-132 (billet size 25x150x150 mm) was acquired for the experimental investigation. Nominal values for the elastic modulus and Poisson's ratio reported by the manufacturer were 310 GPa and 0.28, respectively. Other information, including batch identification number, powder content, processing data, and microstructure is presented in Appendix B.

Specimen Preparation

Specimens were machined so that the prenotch direction and fracture surface normal would be perpendicular to the hot pressing direction. Specimens were surface ground using a 400 grit diamond impregnated wheel. The planar surface of each test specimen had to be polished to a high quality microstructural finish because crack length was measured optically and the width of a crack at its tip is less than a micron. Surfaces were first prepared for polishing using two stages of free abrasive lapping. After receiving the machined specimens, the first lapping stage used a 6 μm diamond slurry and a cast iron wheel and specimens were lapped until all traces of the 400 grit surface grindings had been removed. Using a relatively hard cast iron wheel was an effective way of eliminating machining roughness, but the lapping process was very aggressive and it produced significant grain pull-out. Polishing could not be accomplished before a second lapping stage where 3 μm diamond slurry was used together with a soft copper wheel. This lapping process was less aggressive and it was found to be a crucial step to preparing surfaces for polishing. The first stage of polishing was accomplished using 3 μm diamond paste and a hard, woven nylon cloth mounted on a rotational polisher. A vibration polisher with a soft cloth and 1 μm diamond slurry was used for the final polishing step.

Test Procedure

Ceramic tests were conducted on a closed-loop, servo-hydraulic test system with a 0.73 kN/min force controlled loading rate. The nominal load pin diameter was 5.0 mm and the specified loading rate corresponded to a specimen-free diametral pin expansion

of $0.5 \mu\text{m}/\text{min}$. A linearly applied loading rate on the pin did not correlate linearly with displacements applied to the specimen. Applied displacements depended on specimen compliance which changed during crack extension. The maximum stress applied to the steel pin was slightly more than 1.0 GPa which produced approximately $8 \mu\text{m}$'s of diametral expansion. Crack lengths were monitored optically with high resolution travelling microscope for all tests. Tests were conducted using the loading fixture developed during the preliminary SPL studies shown in figure 3.13. Continuous analog output for pin force and CMOD were recorded on an X-Y plotter and magnetic tape for each test specimen. An example of pin force versus CMOD recorded on the X-Y analog plotter is shown in figure 4.1 for a 3 mm specimen. After testing, magnetic tapes were digitized at frequency of 40 hertz and stored in digital format.

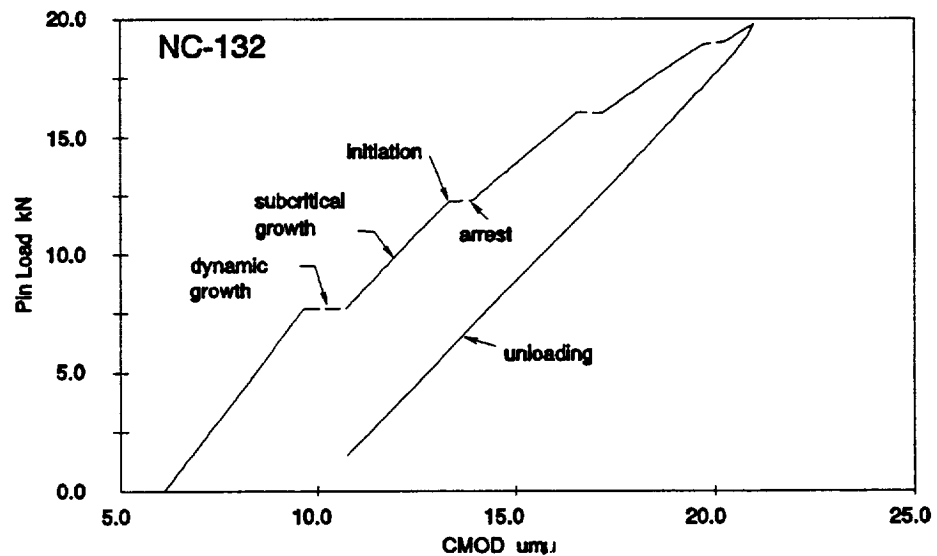


Figure 4.1: Analog records for CMOD versus axial pin load with dashed lines displaying increments of dynamic crack growth.

Voice records for crack length position were also recorded on the magnetic tape and these records provided the means for calibrating a continuous record for crack

length. Optical observations of the fracture surfaces revealed the same contrast changes between zones of slow and fast growth which were observed in the preliminary studies using the older batch on NC-132. Micrographs of the fracture bands observed for the newer NC-132 are presented in figures 4.2(a) and 4.2(b) for both the 3-mm and 1 mm tests. Crack length positions for crack arrest and dynamic initiation measured optically during testing were compared to fracture surface bands for accuracy. The critical crack positions for dynamic arrest and initiation measured during testing agreed with fracture surface features very well as shown in figure 4.3. This result confirmed the accuracy

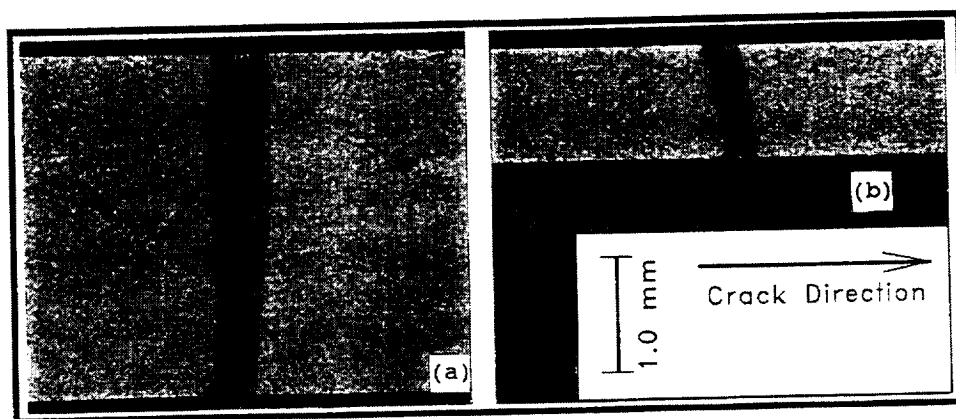


Figure 4.2: Optical light contrast bands observed on the fracture surface for, (a) the 3 mm test case, and (b) the 1 mm test case.

of tracking cracks optically during testing. There was some difficulty in recording the exact position of dynamic initiation during testing because subcritical crack velocities increased continuously with applied displacement. However, these discrepancies were usually small and a frame-by-frame post examination of video tapes produced crack tip

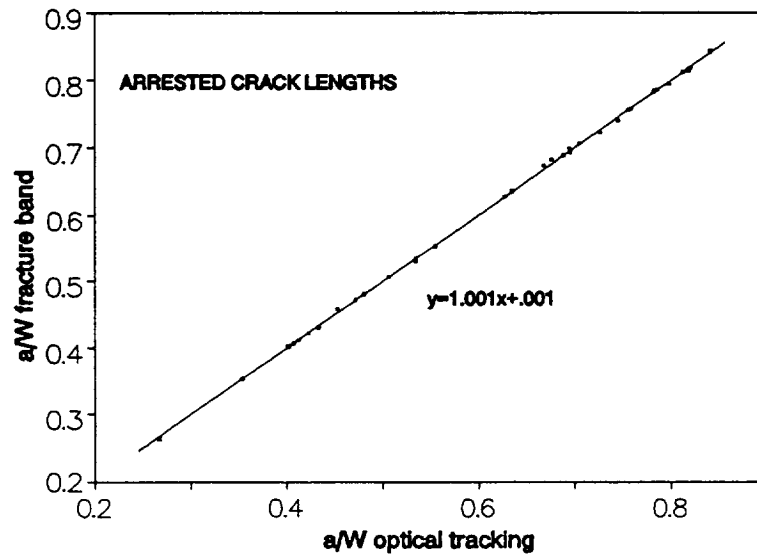


Figure 4.3: Comparison of optical crack length positions taken during testing to contrast band positions demonstrating the accuracy of optical tracking.

positions which agreed very well with the leading edge of each fracture band. Optical crack length measurements during testing represented surface positions. Therefore, the shape of fracture surface marks were used to account for curved or angled crack fronts according to adopted standards (ASTM-E399,1992). Records for continuous crack lengths were generated by plotting discrete crack tip positions versus the corresponding CMOD measurement and fitting a curve to the result as shown in figure 4.4. The best fitting function was then selected and using the CMOD values from the digitized data files as input, refined crack length data files were then generated and stored digitally. After completing this process of calibrating crack lengths, computer data files contained continuous records for time, crack length, CMOD, and pin force for each slow crack growth increment. Digital records for normalized crack length and time were plotted as shown in figure 4.5 to demonstrate the time dependency of slow crack growth conditions.

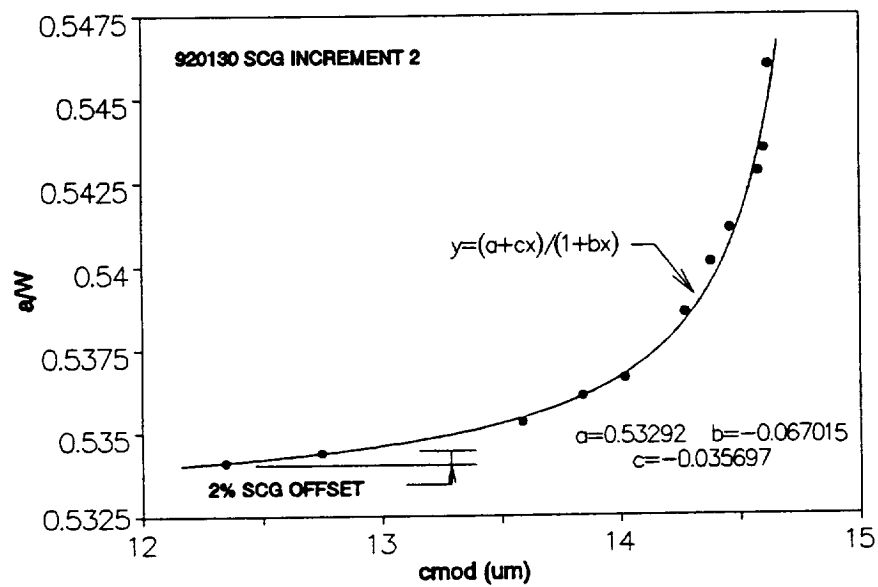


Figure 4.4: Calibration for generating continuous crack lengths from discrete measurements taken during testing.

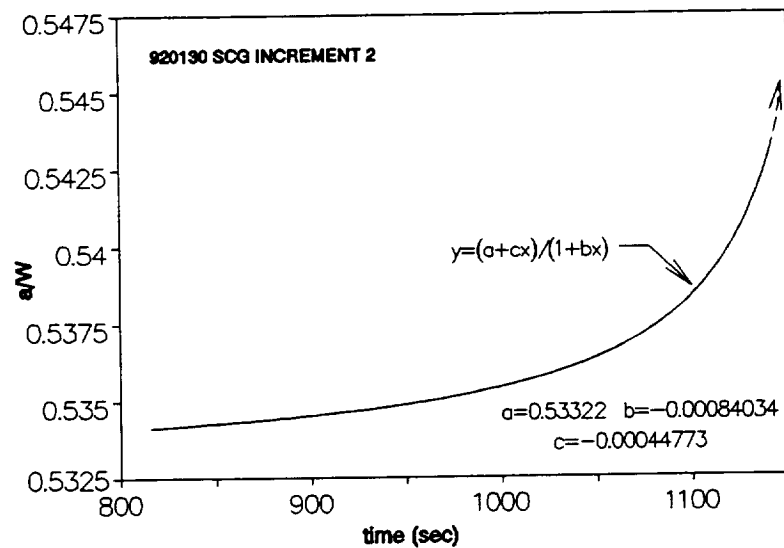


Figure 4.5: Time versus crack length plot for a SCG increment using digitized data records demonstrating a sharp, asymptotic increase in velocity at dynamic initiation.

EXPERIMENTAL RESULTS

General Observations

The number of subcritical crack growth events obtained for each test specimen varied from only one to as many as four in both the 1 mm and 3 mm specimens. Where only one subcritical crack growth event was observed, a single dynamic event often consumed much of the uncracked ligament. A typical plot of crack length versus measured CMOD, exhibiting 3 subcritical crack growth increments, is given in figure 4.6 for a 3 mm sample. Similar results were observed for the 1 mm samples. A summary of the experimental data taken from events of dynamic initiation and arrest is given in table 4.1 for both the 1 mm and the 3 mm samples. Most notable in the experimental results for both specimen thicknesses was large scatter in the dynamic growth increment. The size of dynamic growth increments ranged from 4 to 34 percent of the specimen width. They averaged 4.6 mm for the 3 mm tests and 3.6 mm for the 1 mm tests. Less scatter was observed in the slow growth lengths which averaged 440 and 340 μm for the 3 mm and 1 mm samples, respectively.

Nearly all of the history of each slow crack growth increment was recorded on video tape and crack growth rates were observed to be less than 30 $\mu\text{m}/\text{sec}$ before dynamic initiation. Dynamic initiation always occurred suddenly and little warning of its event was given in the records. Since there was no way of knowing when dynamic conditions would be reached, and how far the crack would extend, the event of dynamic arrest was never captured on video tape. Relocating the position of the crack tip after arrest required 4 to 7 seconds. Thus, other than a discrete measurement of an arrest CMOD, additional information for the arrest event could not be extracted. Video

Table 4.1 Summary of Experimental Results

TEST* SPECIMEN & SCG #	DYNAMIC ARREST		SCG INITIATION				DYNAMIC INITIATION	
			2 % OFFSET		5 % OFFSET			
	a/W	CMOD μm	a/W	CMOD μm	a/W	CMOD μm	a/W	CMOD μm
920109_1	.637	14.8	.637	17.4	.637	17.6	.647	19.0
	.814	20.0						
920210_1	.408	10.7	.409	11.0	.409	11.2	.419	13.4
_2	.555	14.0	.555	14.4	.555	14.6	.564	16.8
_3	.678	17.4	.678	17.5	.678	17.6	.685	20.1
final	.744	20.6						
920211_1	.687	13.4	.688	14.3	.688	14.8	.706	18.3
final	.761	18.9						
920112_1	.411	9.6	.411	9.9	.411	10.1	.420	11.9
_2	.470	12.2	.470	12.6	.470	12.8	.477	14.0
_3	.694	15.7	.694	16.1	.694	16.3	.703	20.4
final	.786	21.3						
920214_1	.487	12.2	.488	12.9	.488	13.3	.500	15.1
_2	.541	15.2	.541	15.4	.542	15.5	.549	17.2
_3	.684	18.1	.684	18.4	.684	18.6	.690	21.4
final	.827	22.6						
920122_1	.265	7.6	.266	8.0	.266	8.2	.285	9.4
_2	.447	10.8	.448	11.6	.448	12.3	.469	14.0
_3	.724	16.3	.724	17.7	.725	18.3	.736	21.1
final	.795	21.6						
920123_1	.363	9.6	.363	10.2	.364	10.4	.374	11.7
_2	.440	12.3	.440	12.5	.440	12.6	.453	14.2
_3	.520	14.8	.520	15.2	.520	15.3	.531	16.9
_4	.708	18.8	.708	19.7	.709	19.9	.712	22.2
final	.784	23.2						
920124_1	.630	14.0	.630	15.3	.630	15.8	.645	18.9
final	.758	19.8						
920129_1	.395	9.7	.396	10.0	.396	10.2	.413	12.3
final	.753	14.4						
920130_1	.427	9.9	.427	10.0	.427	10.1	.432	12.0
_2	.537	12.4	.537	12.8	.537	13.1	.546	14.6
_3	.694	15.6	.695	16.2	.695	16.6	.708	19.0
final	.819	19.9						

*Test samples with 1 millimeter thickness are bolded

recording continued after arrest and it was noted that subsequent crack growth did not occur until applied CMOD values had increased to some threshold level. Computer files for each subcritical increment were used to estimate the CMOD level required to re-initiate slow growth. Subcritical crack length offset levels of 2 and 5 percent of the total increment size, as shown in figure 4.4, were used and the resulting CMOD values are given in table 4.1. These measurements for CMOD are used later to estimate the energy required to re-establish subcritical crack growth after dynamic arrest.

Once slow crack growth was re-established, crack tip velocities increased monotonically with increased CMOD until the next dynamic event. The transition from slow growth ($\mu\text{m}/\text{sec}$) to fast growth (km/s) was sharp and explosive, not continuous and smooth as is commonly believed (Mecholsky, 1986). A post testing frame-by-frame review of the video tape records revealed that dynamic transition occurs in less than one frame. The time increment between frames is the standard 1/30 second, so the transition from subcritical to dynamic crack growth conditions is likely less than the resolution of the video system. Examination of the time versus crack length plot presented in figure 4.5 demonstrates the approach to critical crack growth conditions is asymptotic. Plots of normalized crack lengths versus CMOD for were reconstructed for the entire test record from the digital files and an example of this result is given in figure 4.6.

Crack Driving Forces

Energy release rates (ERR) at dynamic initiation, G_I^i , and arrest, , were evaluated from test data using the linear elastic solutions established during the development of the SPL specimen. The Coulomb friction calibration given in table 3.4

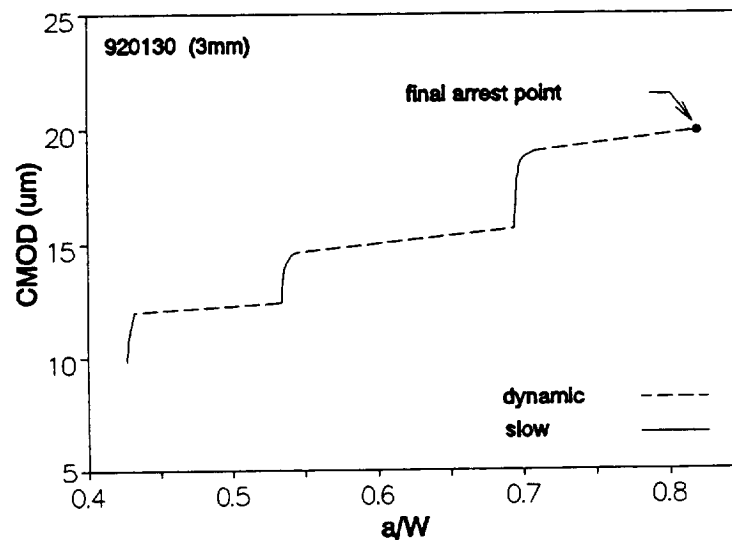


Figure 4.6: Plot of crack length versus CMOD for the entire test specimen taken from the computer records of digitized analog signals.

was used for ERR calculations and a typical result of these calculations is plotted in figure 4.7 for a 3 mm sample. Also shown in the figure are the corresponding optical micrographs of the slow growth zones on the fracture surface. The summary of experimental data listed in table 4.1 was used for the calculations given in table 4.2.

Evaluations for ERR at arrest only accounted for static stress conditions and no attempt was made to include kinetic effects. Although a static analysis simplifies the problem, the approach did not alter experimental interpretations since ERR estimates were used only to measure the minimum energy required to re-initiate slow crack growth. Nevertheless, for a static analysis to be valid, it had to be determined that input of kinetic energy from waves reflected from free surfaces did not interfere with the arrest event (Kanninen, 1985). A simple treatment equating crack propagation time to reflected wave time demonstrated that interference would not occur provided crack propagation

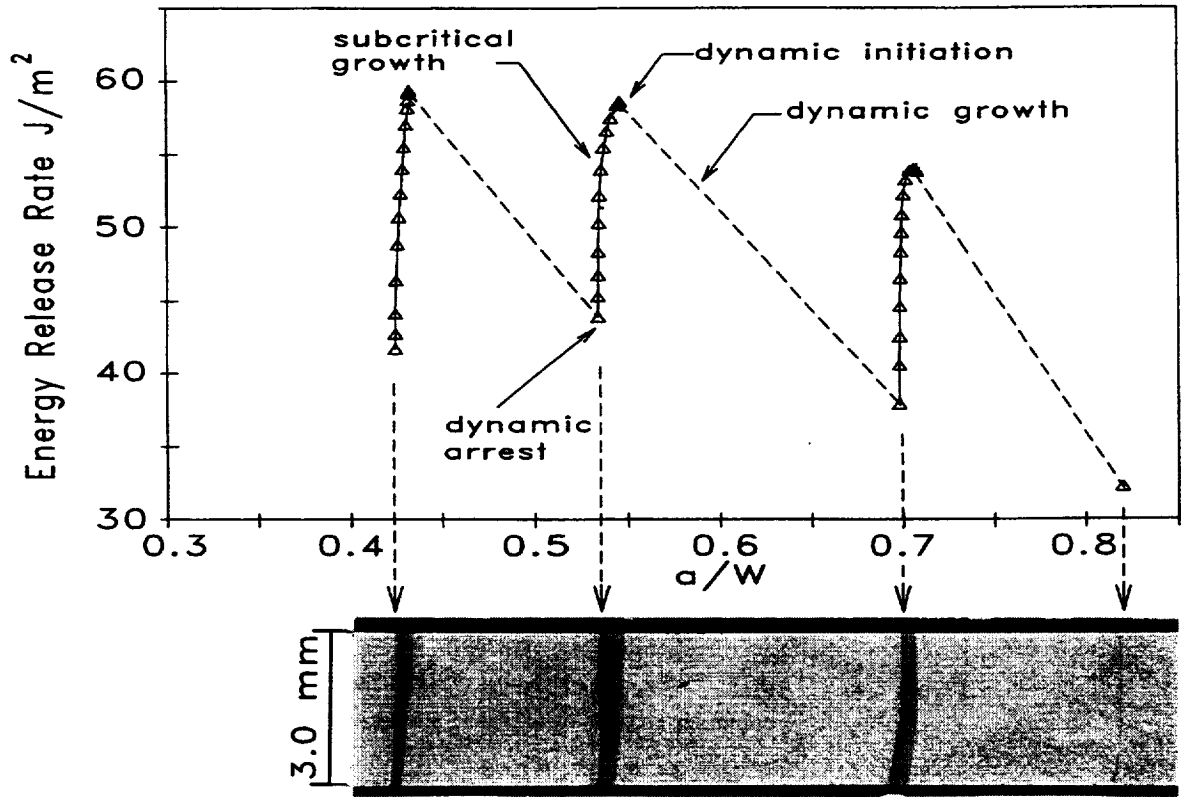


Figure 4.7: Linear elastic ERR evaluations taken from the data given in figure 4.6. Also shown are the respective contrast bands relating to each SCG increment.

rates were at least 40 percent of the shear wave speed. Since estimated values for this ratio range from 50 to 55 percent (Kanninen, 1985), dynamic arrest occurred before return waves could interfere. Specific details of the treatment are given in Appendix C.

The ERR values for G_I^a and G_I^i , varied significantly for each jump increment in both the 1 mm and 3 mm tests. The average value of G_I^i for the 3 mm tests was $68 J/m^2$ with a standard deviation of $8.3 J/m^2$, and the average value of G_I^a for the 3 mm tests was $46 J/m^2$ with a standard deviation of $9.5 J/m^2$. For the 1 mm tests G_I^i and G_I^a averaged 69 and 48 J/m^2 , respectively, with standard deviations of $8.9 J/m^2$ for both the initiation and arrest measurements. Due to the stated limits of the numerical calibration

Table 4.2 Summary of Linear Elastic Energy Release Rates

TEST* SPECIMEN & SCG #	DYNAMIC ARREST		SCG INITIATION		DYNAMIC INITIATION	
			2% OFFSET	5% OFFSET		
	a/W	G_{II} MPa√m	$G_{12\%}$ MPa√m	$G_{15\%}$ MPa√m	a/W	G_{II} MPa√m
920109_1	.637	43.7	59.9	61.4	.647	68.8
final	.813	34.1				
920110_1	.408	52.7	55.1	56.7	.419	79.1
2	.555	52.3	54.9	56.7	.564	72.4
3	.678	51.2	52.0	52.3	.685	66.2
final	.744	53.3				
920211_1	.687	29.3	33.4	35.3	.706	50.4
final	.761	41.3				
920112_1	.411	41.5	44.6	46.3	.420	61.9
2	.470	53.6	57.0	58.7	.477	68.9
3	.694	38.8	40.9	42.2	.703	63.3
final	.786	45.6				
920214_1	.487	50.6	56.4	59.5	.500	73.2
2	.541	64.6	66.1	67.0	.549	80.2
3	.684	54.4	56.2	57.4	.690	73.7
final	.827	39.7				
920122_1	.265	51.9	57.7	60.3	.285	71.6
2	.447	45.9	52.5	59.4	.469	71.0
3	.724	36.9	43.4	46.1	.736	58.1
final	.795	44.7				
920123_1	.363	50.4	57.1	59.4	.374	72.1
2	.440	61.1	62.9	64.1	.453	77.8
3	.520	65.9	69.2	70.5	.531	82.8
4	.708	52.6	57.6	58.7	.712	72.2
final	.784	54.7				
920124_1	.630	40.0	47.9	51.1	.645	68.5
final	.758	46.1				
920129_1	.395	45.6	48.2	50.2	.413	67.7
final	.753	25.1				
920130_1	.427	41.2	42.5	43.3	.432	59.4
2	.537	43.5	46.5	48.4	.546	58.6
3	.694	38.3	41.4	43.2	.708	53.8
final	.819	32.2				

*Test samples with 1 millimeter thickness are bolded

for the SPL specimen given in Chapter III, data points at crack lengths greater than $a/W=0.8$ were excluded in these averages. Calculated ERR values for both the 1 mm and the 3 mm tests were essentially comparable both in the average value and standard deviations. A statistical comparison of both the 1 mm and 3 mm data sets using a Student T criteria demonstrated that to a confidence level of less than 70 percent they could be considered equivalent. Since the fracture response of both the 1 mm and 3 mm specimens was the same and their numerical results compare, it was concluded that the change in specimen thickness did not affect fracture behavior for this study.

Calculated values for G_I^a and G_I^i were plotted versus normalized crack length to examine for possible dependency on crack length. The existence of a trend would suggest that multiple fracture events for one sample could not be considered independent events without additional treatment. Since there was no evidence of thickness effect, both data sets were merged for further numerical treatment. Combined G_I^i and G_I^a values versus normalized crack length are plotted in figure 4.8. A linear regression analyses of these test data suggested the presence of a decreasing trend with crack length in the both G_I^i and G_I^a values. Unfortunately the statistical scatter was large and statements concerning a trend could not be concluded.

A more conclusive statement concerning crack length trends was obtained by examining the unprocessed experimental data for CMOD values. Such an approach was a reasonable since ERR values are related to CMOD values squared which causes amplification of the scatter. The CMOD values at dynamic arrest, re-initiation of slow crack growth (2 percent offset), and dynamic initiation, were plotted versus normalized crack length as shown in figures 4.9(a) through 4.9(c). A best-fit curve for CMOD was

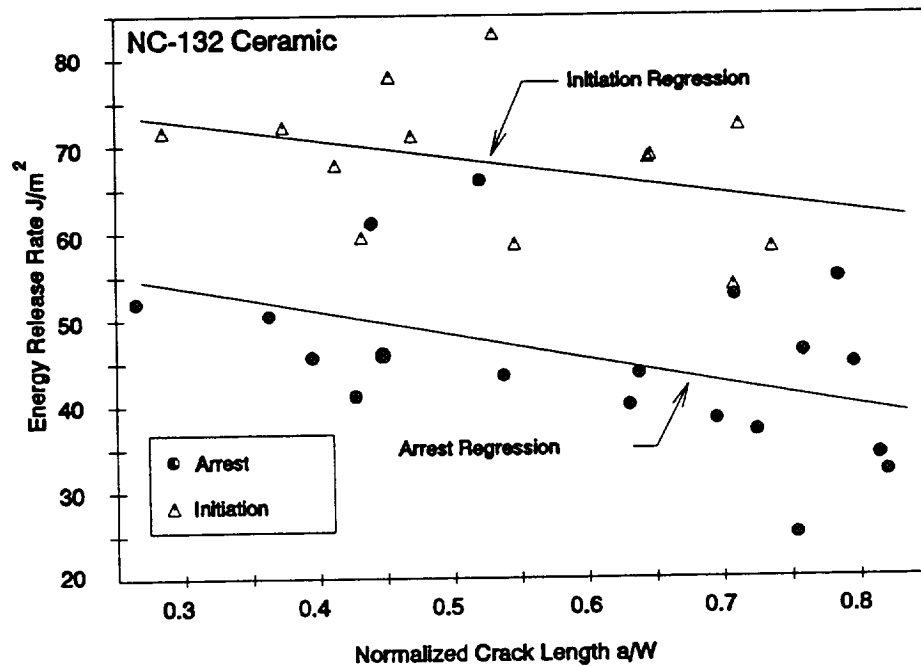


Figure 4.8: Plot of critical ERR at dynamic initiation and arrest with linear regression analysis results spuriously suggesting a decreasing trend in recorded values.

then calculated using the ERR elastic solution for the simple constant valued ERR case. The results of this approach revealed no evidence of a deterministic trend with crack length for experimental results. Considering that fracture is inherently a stochastic process, excellent agreement was achieved for the constant valued ERR approach. Additional support for the lack of a trend is exhibited in the linear regression analyses given in figure 4.9(a) through 4.9(c). For all three cases the constant ERR curve calculated through the 'best-fit' approach is nearly coincident with the linear regression results. Therefore, it was concluded that the sequence of dynamic arrest, slow growth, and dynamic initiation exhibited no evidence of crack length influence. The average ERR value at arrest, re-initiation of slow crack growth and dynamic initiation based on the best-fit approach are listed in table 4.3. The ERR values at dynamic arrest and

initiation were calculated to be 47 and 67 J/m², respectively. Using the best-fit approach for CMOD, threshold levels for the re-initiation of subcritical crack growth were 51 J/m² at the 2 percent and 53 J/m² at the 5 percent offset levels.

Best-fit calculations for ERR compared well with the mathematical averages of values given in table 4.2. Both approaches confirm that the fracture resistance of NC-132 increases during increments of subcritical crack extension. In terms of average linear elastic energy release rates, the critical fracture toughness of the ceramic material was 43 percent greater than that measured at dynamic arrest and nearly 30 percent greater than the average 2 percent threshold fracture resistance. This measured increase in fracture resistance is the first ever recorded for the NC-132 material. Although all previous studies have reported a constant valued resistance, the increase measured here is considered to be very accurate. The elastic solution for the SPL specimen is essentially constant for small increments of crack extension. Therefore, measured increases in resistance for subcritical growth depends on the increase in CMOD which was measured with conventional extensometry having an accuracy better than 0.10 μm . The discrepancy in reported performance of the NC-132 material is testimony to the refined capabilities of the SPL for assessing fracture behavior.

FRACTOGRAPHY

General Observations

Detailed information concerning the resistance mechanisms which contributed to increases in fracture resistance was obtained from fractography studies using scanning

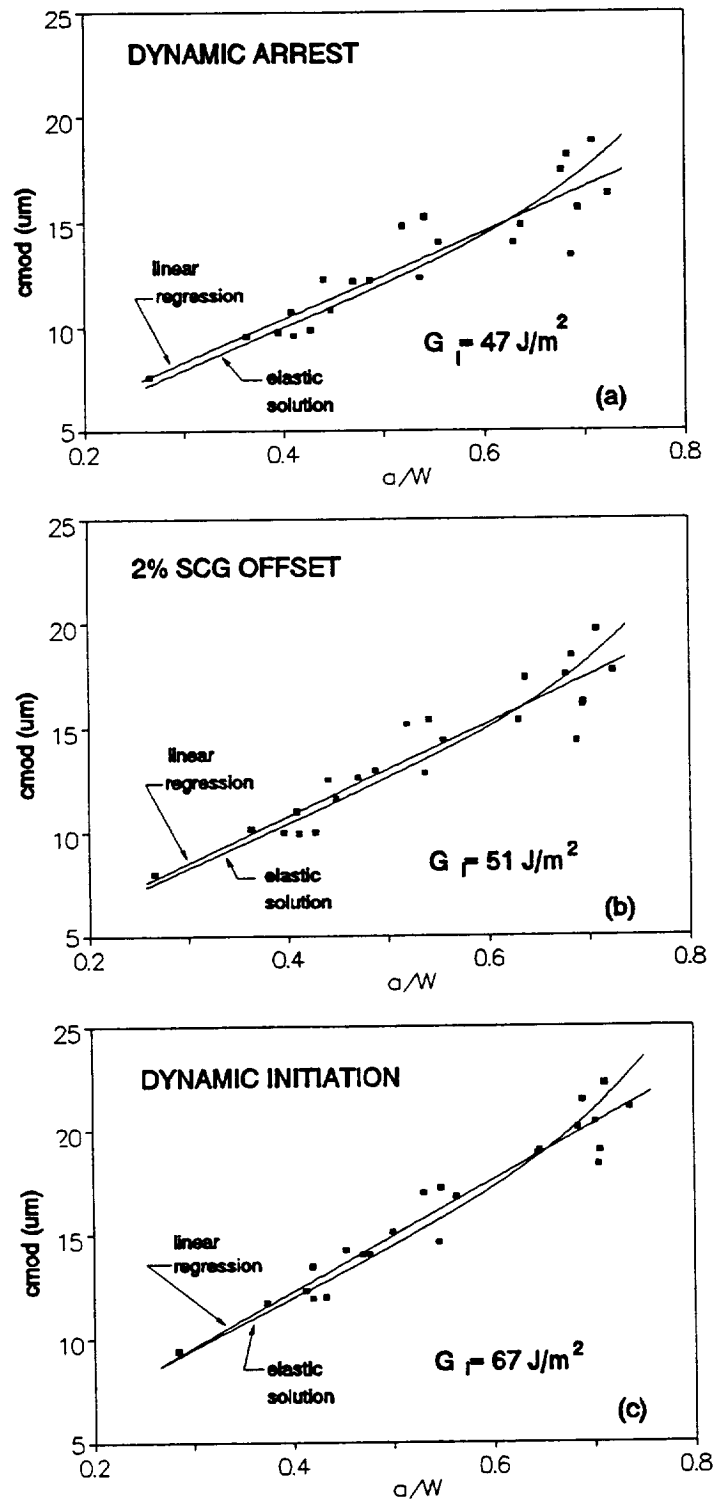


Figure 4.9: Energy Release Rate (ERR) analysis using experimentally recorded critical CMOD values compared to values expected assuming constant ERR behavior.

Table 4.3 Best-fit Energy Release Rates

Fracture Event	Average ERR* J/m ²	Std. Dev.* J/m ²	Best-fit ERR J/m ²
ARREST	47	9.2	47
2% OFFSET	52	8.8	51
5% OFFSET	54	8.9	53
INITIATION	68	8.4	67

*ERR values determined from data listed in table 4.1

electron microscopy. Since surface features were small and the Si_3N_4 material is opaque, optical micrographs did not reveal much information. Scanning electron microscopy (SEM) was used to obtain higher resolution images of fracture surfaces for comparison. These SEM studies revealed that the changes in optical contrast were produced by an increase in surface tortuosity for the slow crack growth bands. Additional SEM studies using acetate replicas taken from the fracture surface also revealed that the fracture process loosens ceramic material near the fracture surface in the subcritical bands. These particles were taken as evidence that, in addition to increased surface roughness, other resistance mechanisms were active during subcritical crack growth.

The SEM images shown in figures 4.10(a)-(d) were taken from the second fracture band of test specimen 920130. The secondary electron image shown in figure 4.10(a) demonstrates a similar contrast change for the slow growth increment observed in the optical micrographs. However, here the contrast is shown to be related to increase surface roughness which was enhanced by tilting the fracture surface 25° as shown in figure 4.10(b). A topography image of the tilted fracture surface as shown in figure 4.10(c) also demonstrates the increased size of surface features within the slow growth

zone. Clear evidence that slow crack growth produced increased surface roughness can be seen in figure 4.10(d) which was generated using the YZ modulated option of the SEM (see Appendix B for image description). The YZ modulation image enhances the finer details of the imaged surface and is therefore sensitive to the small scaled changes in surface texture between slow and fast crack growth. All four micrographs demonstrate the sharp transition in surface roughness between subcritical and dynamic crack growth conditions.

Higher magnification SEM micrographs of the fracture surface were taken to examine the characteristics of roughness at the microstructural level. Figures 4.11(a) through 4.11(d) were obtained from the second subcritical increment of 3 mm specimen 920130. Observation revealed that slow crack growth was primarily intergranular. These micrographs show surface texture immediately before arrest, during slow crack growth, just prior to dynamic initiation, and after dynamic initiation. Similar micrographs at a higher magnification are given in figures 4.12(a) through 4.12(d). Dynamic crack extension was primarily intergranular with a small mixed amount of transgranular fracture. These results are common with observations from other fracture studies of the NC-132 material (Mecholsky, 1981).

Comparison of the slow growth region at higher magnification also reveal a change in surface texture compared to that for fast extension. Figures 4.12(b) and 4.12(d) show that during fast extension elevation fluctuations are small and incremental steps extend over many grains during crack advance. However, during subcritical growth fluctuations in elevation are significantly larger and incremental steps encompass only a few grains. The transition morphology between the smooth dynamic surface and

rough slow growth surface was not sharp at high magnifications for both dynamic arrest and initiation. Figure 4.12(a) was taken near a dynamic arrest point just into the slow growth region, and figure 4.12(c) was taken at the dynamic initiation point. Fracture surface features in both micrographs are large compared to purely dynamic fracture region. Although subtle differences can be seen between all three micrographs taken within the slow growth band, individual comparisons did not yield obvious surface texture trends. In fact, surface analysis using the SEM lacked the ability to gauge texture changes where only subtle differences were present.

The SEM images provided information about the small (micro) scaled characteristics of surface texture, but larger (macro) scaled fluctuations and trends could not be clearly identified at high magnification. Since it was now established that increased surface roughness was a least one mechanism contributing to increased fracture resistance, there was a interest to quantify the changes in roughness throughout a subcritical crack growth increment. As a first attempt, acetate replicas were taken from a virgin fracture surface of a test sample. The motivation for replicating was to use light wave diffraction techniques to optically view the acetate film for possible surface patterns. Efforts to identify patterns in the acetate film proved to be unprofitable. However the process of replicating lead to an interesting discovery of ceramic particles which were actually removed from the surface in the process. Furthermore, an increased amount of these particles was found within the slow crack growth bands. Attempts to characterize fracture surface debris discussed next were simply exploratory investigations of what is expected to be a promising area for future research.

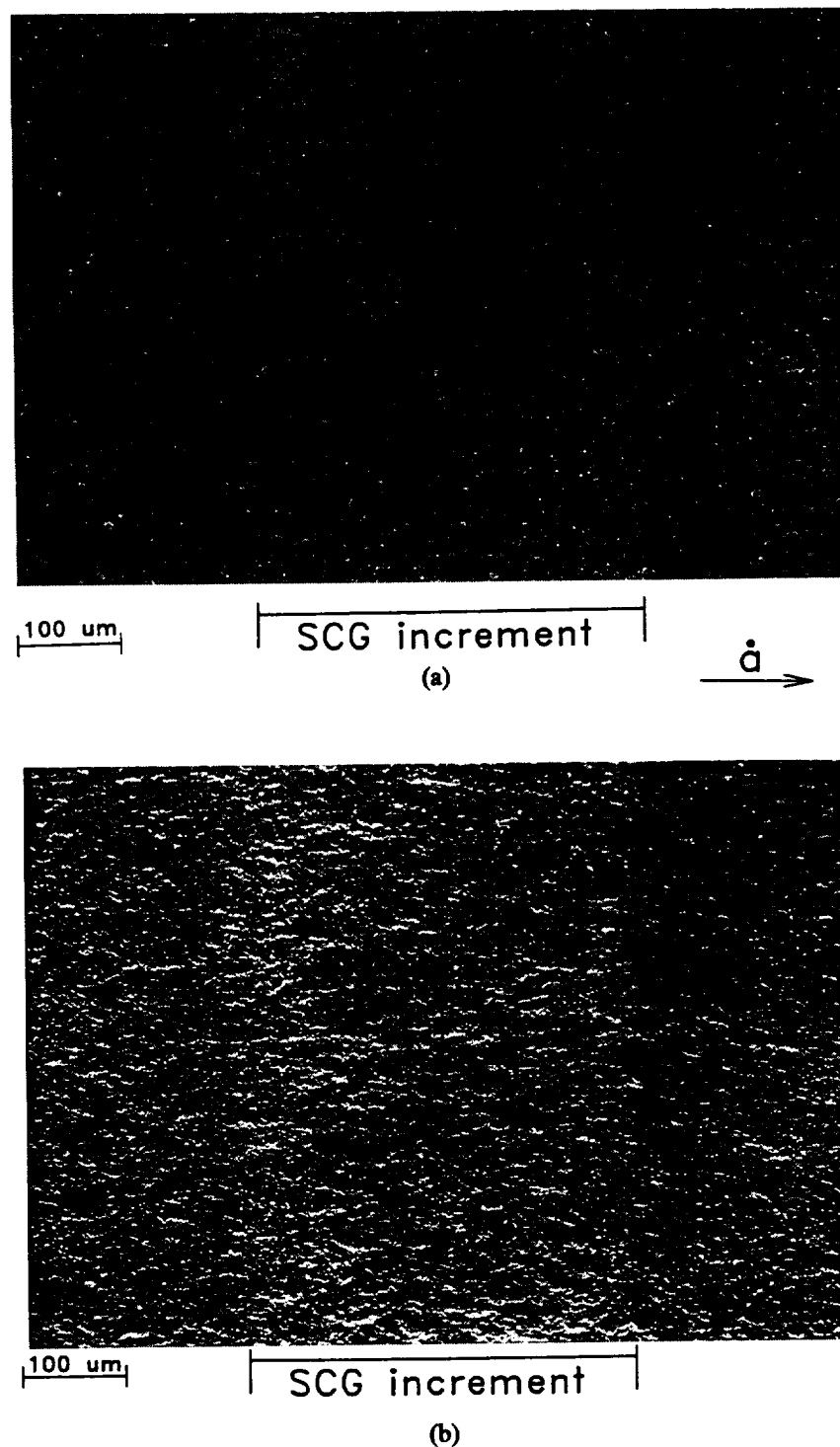


Figure 4.10: Low magnification SEM micrographs of SCG increment 2 [920130_2] (a) secondary electron (SE) image, (b) SE image with specimen tilted 25°. [4.14(c) and (d) next page]. All techniques demonstrate changes in fracture surface morphology between slow and fast growth with clear delineation of critical crack positions.

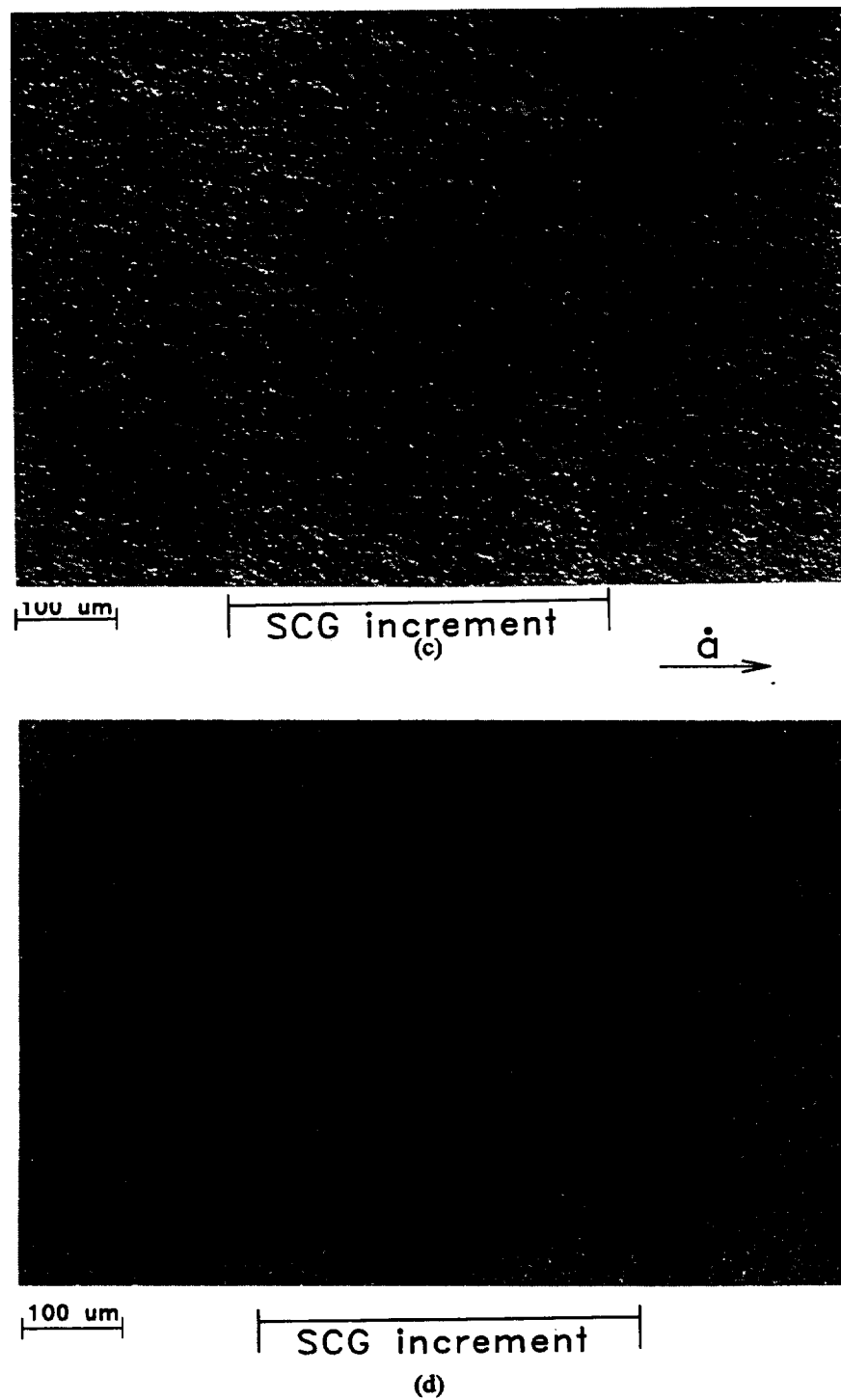


Figure 4.10: [continued] (c) topography image of 25° tilt, and (d) YZ modulated image. All techniques demonstrate changes in fracture surface morphology between slow and fast growth with clear delineation of critical crack positions.

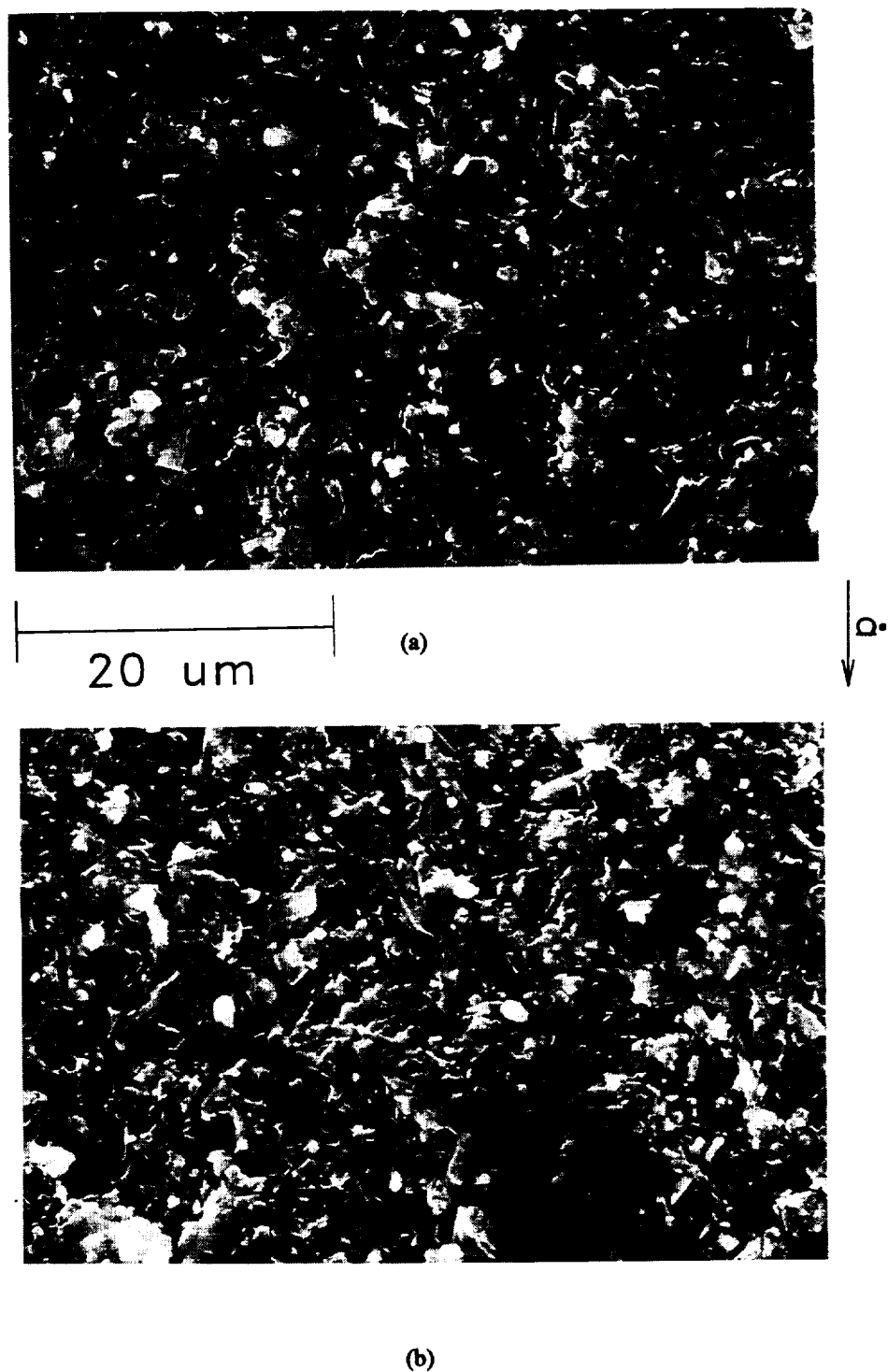


Figure 4.11: High magnification SEM images of fracture surface from 920130_2 showing surface texture (a) immediately after SCG initiation, (b) center of SCG increment, [4.11(c) and (d) next page]. Rough surface texture observed at the onset and center of SCG, smoother at the end and for DCG.

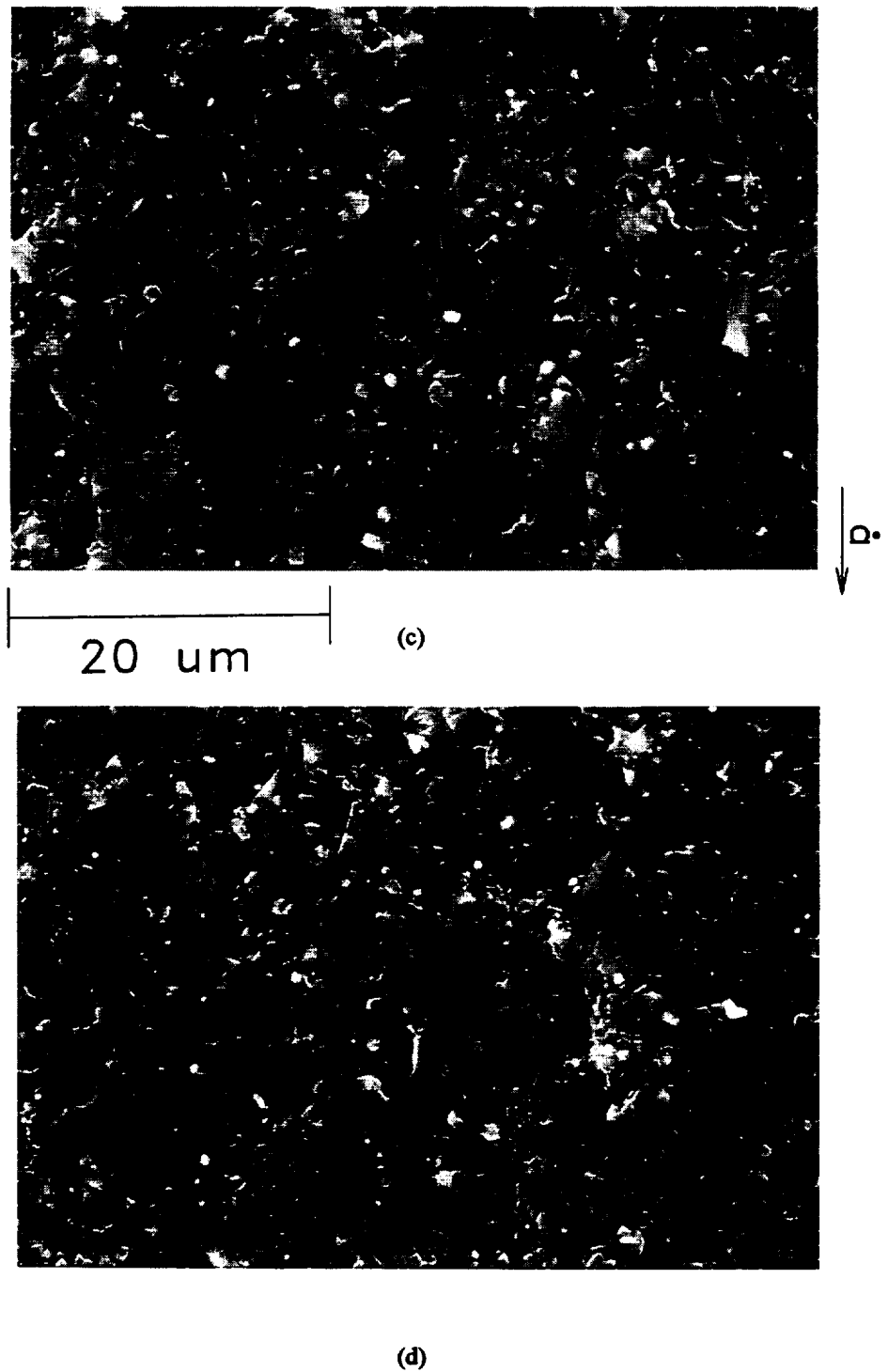


Figure 4.11: [continued] (c) end of SCG increment but before DCG, and (d) well after dynamic initiation. Rough surface texture observed at the onset and center of SCG, smoother at the end and for DCG.



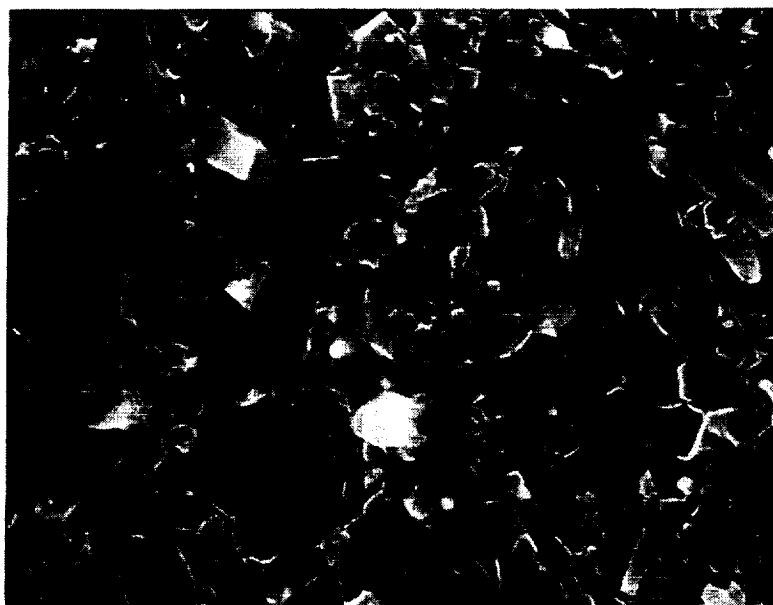
(a)

10 μm 

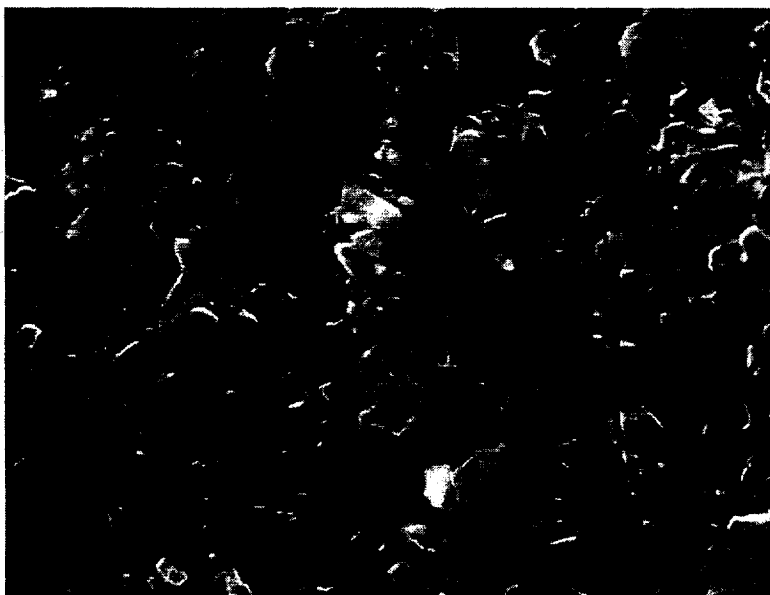
(b)

Figure 4.12:

Higher magnification SEM images similar to figure 4.11 (a) initiation of SCG, (b) center of SCG increment, [4.12(c) and (d) next page]. These images exhibit the difference in surface texture between slow (large elevational changes) and fast (smaller elevational changes) growth.



(c)

10 μm 

(d)

Figure 4.12: [continued] (c) end of SCG increment but before DCG, and (d) DCG increment.

Fracture Surface Debris

The optical micrograph in figure 4.13 was taken from a slow band and demonstrates that the replicating process actually removed ceramic material which had been loosened and left behind by the fracture process. The optical micrograph is not in focus over the entire field of view because of the warped surface of the acetate film, however, a high density of ceramics particles can still be clearly seen. Multiple replicas taken from the same fracture surface revealed that nearly all surface debris was removed with the first acetate tape, establishing that the removal of debris was not caused by replicating process.

Backscatter SEM imaging was used to identify Si_3N_4 particles on the acetate replica and a typical micrograph of these results is shown in figure 4.14 for the 3-mm sample 920122. The white areas are ceramic debris removed from surface and the black background is the acetate. The band of Si_3N_4 particles observed in the backscatter image corresponds directly with the band of slow crack growth with the more sparsely populated regions resulting from fast growth. Some care was given to the interpretation of the micrograph in figure 4.14 since it was determined that these images were slightly affected by surface texture. Still the majority of the white areas was related to surface debris which allows for a qualitative discussion. The backscatter image in figure 4.14 demonstrates the difference in the debris densities between fast and slow crack growth. Particularly interesting is an apparent trend to the density within the slow growth zone. A dense population of white areas is present during the early stages of slow growth immediately after arrest, but deeper into the slow growth zone densities taper to the fainter boundary where dynamic initiation occurs.

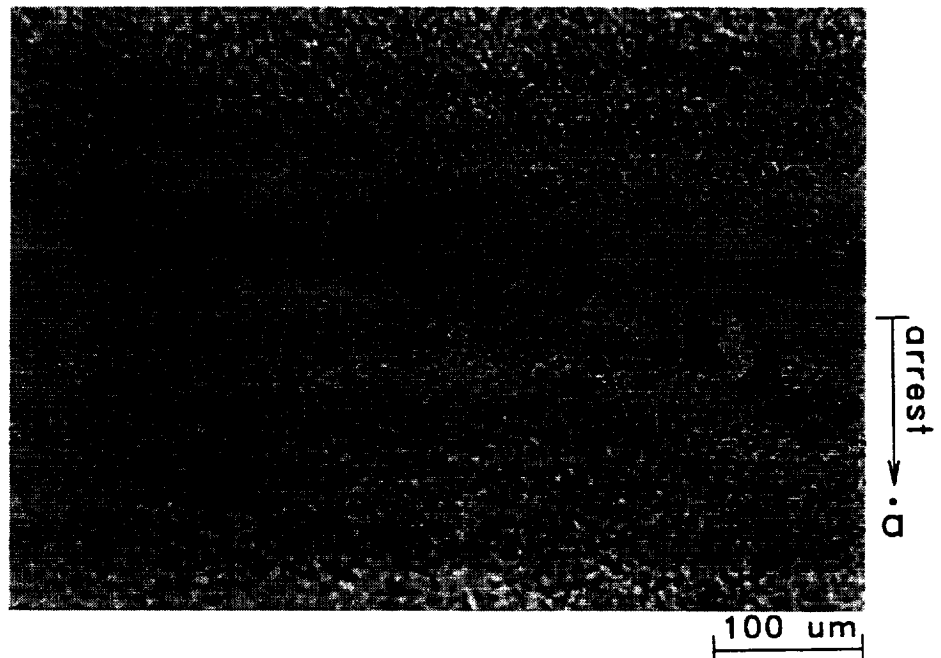


Figure 4.13: Transmitted light optical micrograph of acetate film taken within a SCG increment. Dark areas are ceramic debris removed during the replicating process.

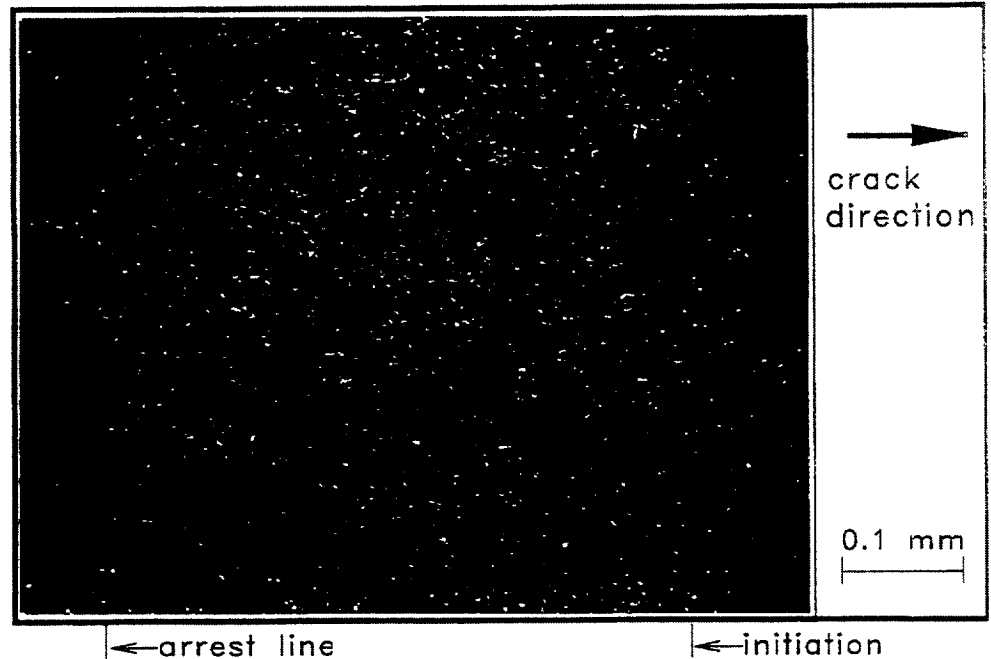


Figure 4.14: Backscatter scanning electron micrograph of acetate film displaying the increased amount of ceramic particles obtained within regions of SCG. Note some influence of surface texture was present in this image.

After discovering that increments of slow growth generated increased amounts of fracture debris which could be removed by replicating, more careful experiments were conducted. Based on the preliminary observations, it was thought some of the ceramic particles removed by the replicating film had been encapsulated by acetate material and could not be imaged with the SEM. It was proposed that a procedure of coating fracture surfaces with a conductive film before replication and examining these surfaces with the SEM after replication would provide more detailed information concerning surface debris. Provided the conductive film cohered well with the fracture surface, the removal of conductive coating would be associated with the extraction of particles. Examining the real fracture with the SEM after replication would then produce charged areas where the coating (ceramic debris) had been removed. Image analysis techniques could then be used to assess particle counts, size estimations and density distributions within regions of slow growth.

Because of its cohesive properties with the silicon nitride material (Dauskardt, 1987) a sputter deposited chrome film with a thickness of $0.01\ \mu\text{m}$ was used for this study. The 1 mm sample 920211, and 3 mm sample 920130 were selected for treatment. The second subcritical crack growth region was examined for each specimen considered. Scanning electron micrographs were taken from the fracture surface after coating samples with chrome but before replication for reference. After replicating, the same areas on the fracture surface were re-examined and comparative micrographs were taken as shown in figures 4.15(a) and 4.15(b) for a 1 mm sample. Three areas within each slow growth region were imaged at higher magnifications and the resulting micrographs are given in figures 4.16(a) through 4.16(c). A similar sequence of micrographs taken for the 3 mm

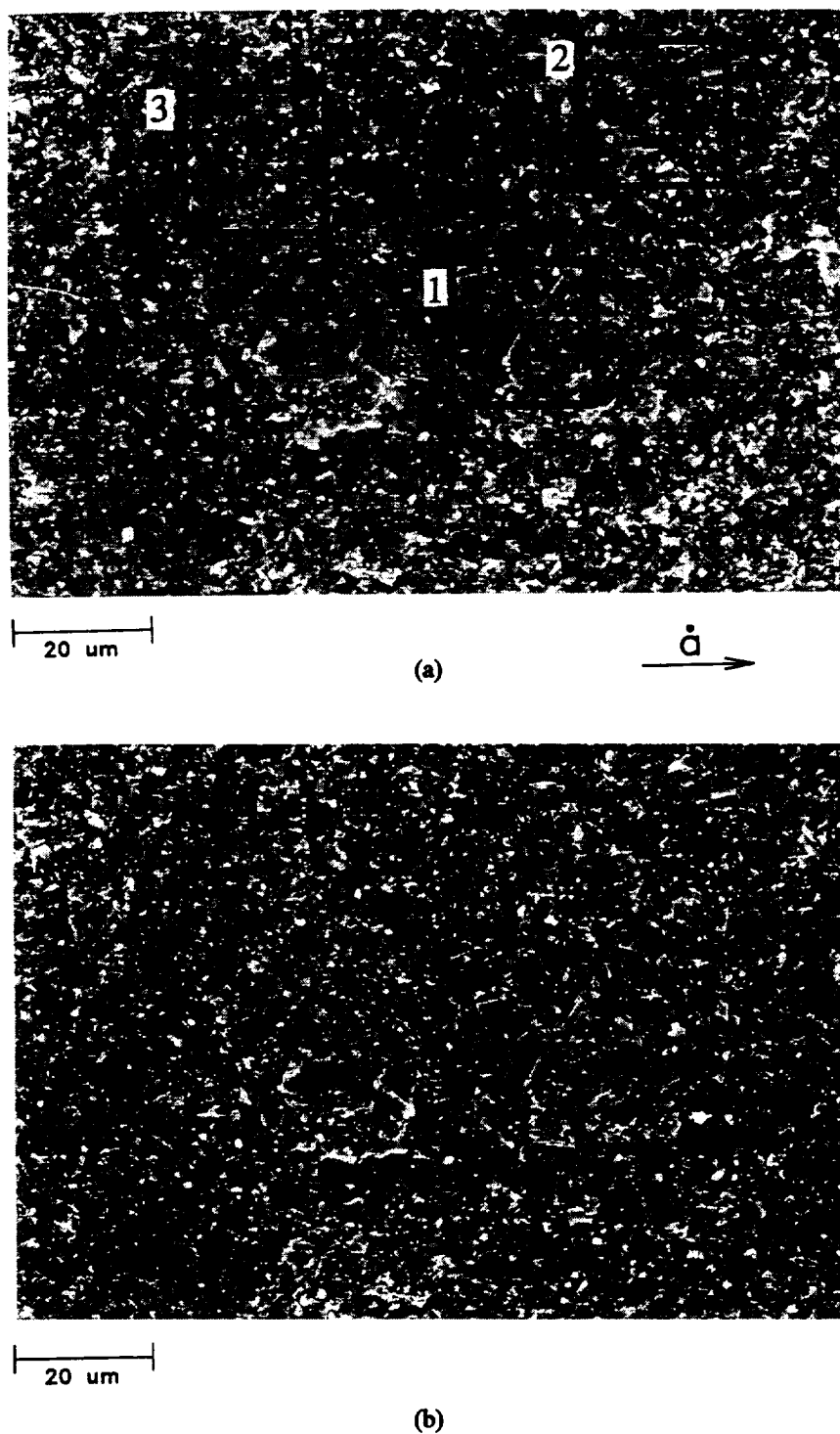


Figure 4.15:

SEM micrographs of fracture surface from a 1 mm sample taken (a) before replicating, and (b) after replicating showing three separate areas examined at high magnification. High magnification images given in figures 4.16(a) through (c). Similar micrographs for 3 mm sample given in Appendix D.

sample are given in Appendix D.

Unfortunately regions of the fracture surface uncovered by the replication process did not charge and produced the contrast changes expected. However, comparing the complementary micrographs taken before and after replication confirms that ceramic material was removed from the surface. Those features removed from the surface can be identified by scanning the micrographs visually and a few examples are circled. Particles removed from the surface varied in size from only 1 μm , or one grain, to more than 5 μm , corresponding to agglomerates of several grains. Although none of the three regions examined retained all of their features, the micrographs demonstrate that most of the surface features were not disturbed by replicating. Assessing more quantitative information concerning surface debris using a visual method was not considered practical. Accurate measurements needed to be made at a scale of 40 μm and then mapped up an order of magnitude to the band width scale of 400 μm for density distributions. Therefore only qualitative information was obtained from SEM images of the real fracture surface after replicating. It is possible that high resolution scanning Auger imaging could be used to distinguish chrome coated areas from the silicon nitride areas uncovered by replicating and this procedure may be a future consideration.

Quantitative information was generated from replicas taken off the second fracture band of specimen 920130. High magnification backscatter electron images of the acetate film taken from the second band are given in figures 4.17(a)-(b). These images were taken from selected areas within the slow growth band and show a distribution of ceramic particles ranging in size from less than 1 μm to almost 10 μm . At a magnification of 1000X the larger particles were clearly identified as clusters of smaller particles

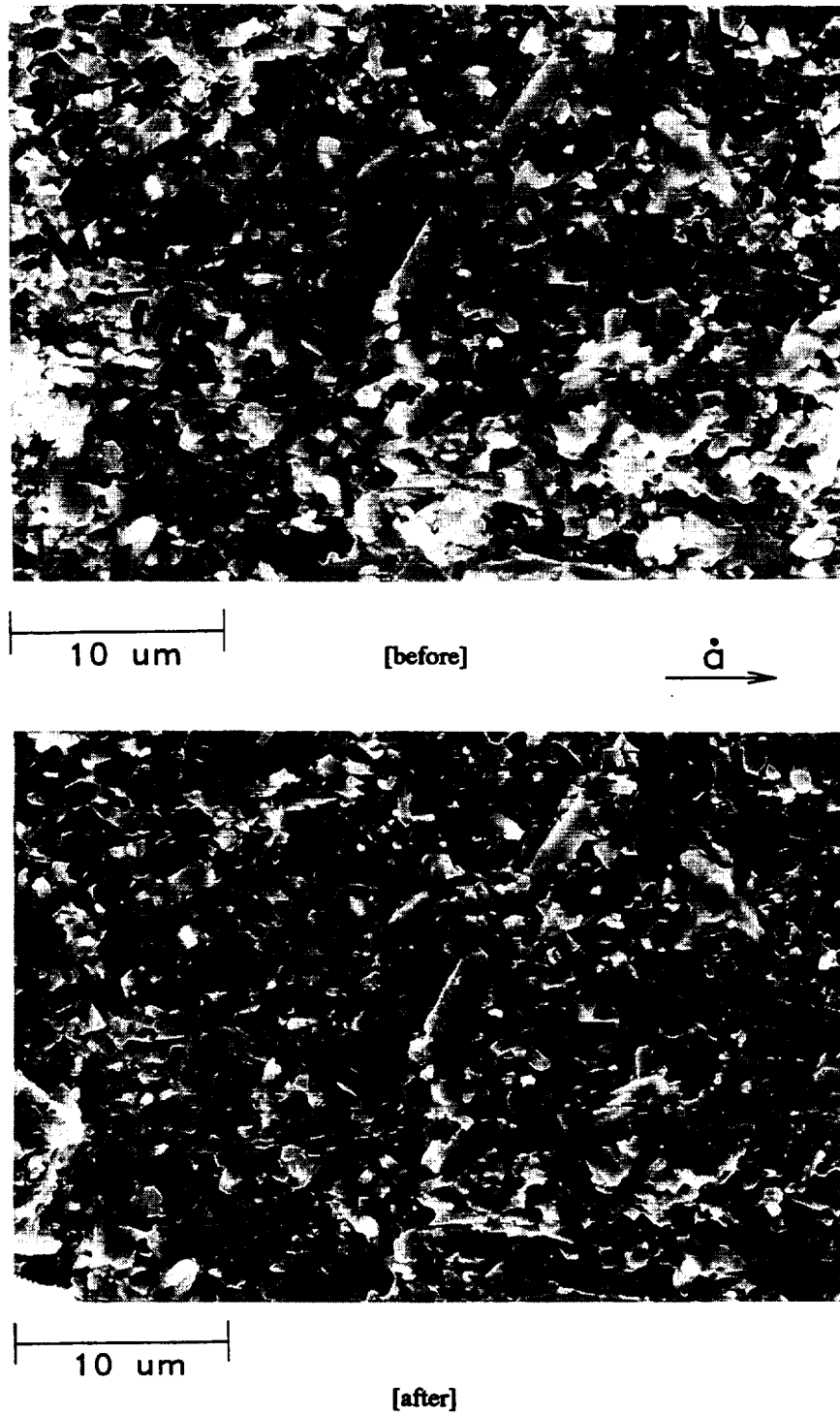


Figure 4.16(a): Fracture surface SEM micrographs taken from region 1 before and after replication exhibiting some characteristics of particles removed from the surface.

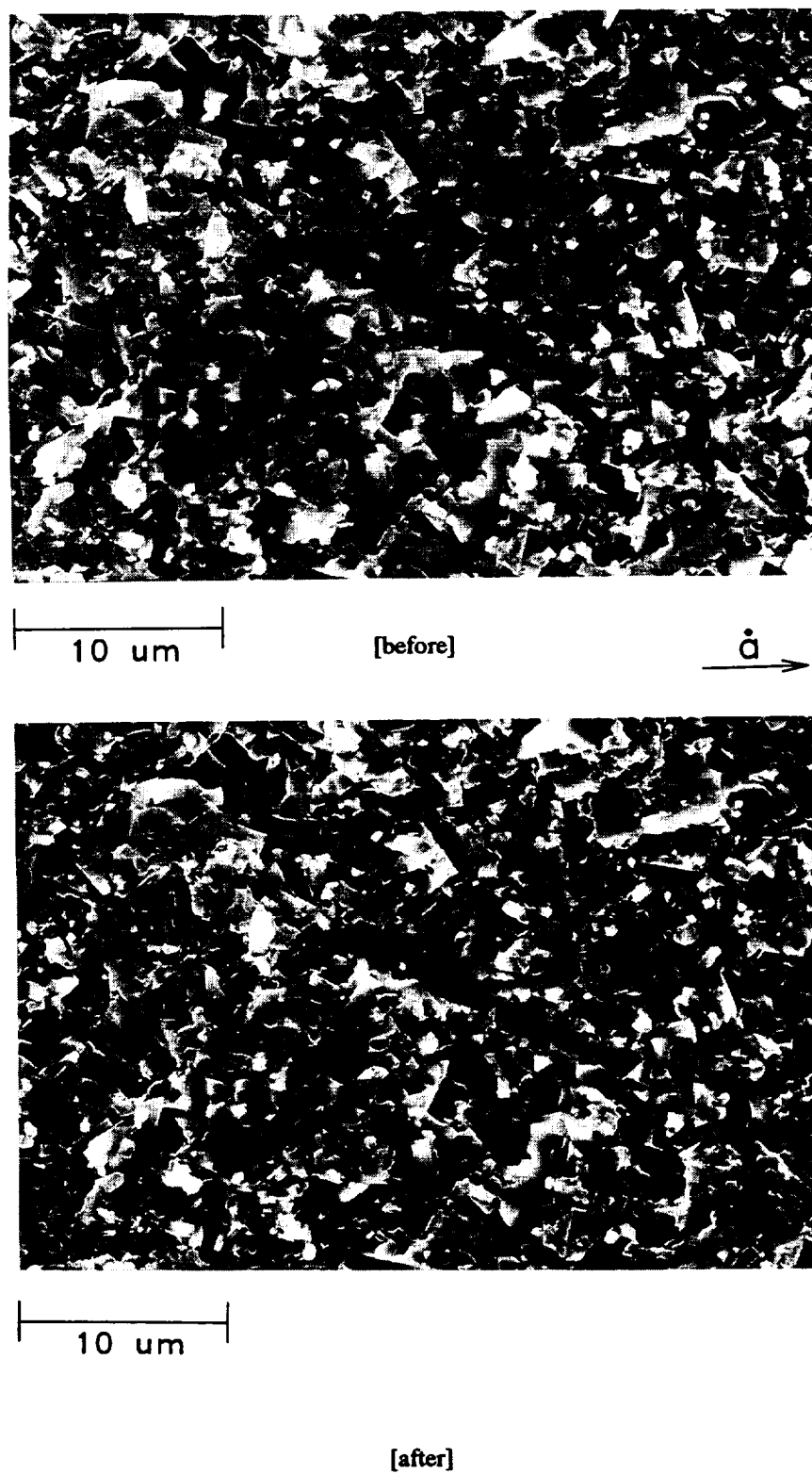
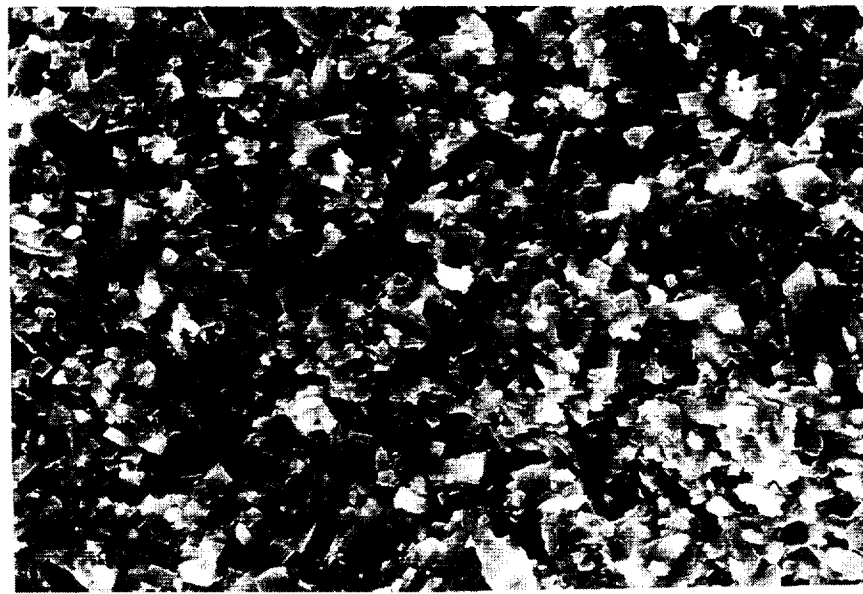


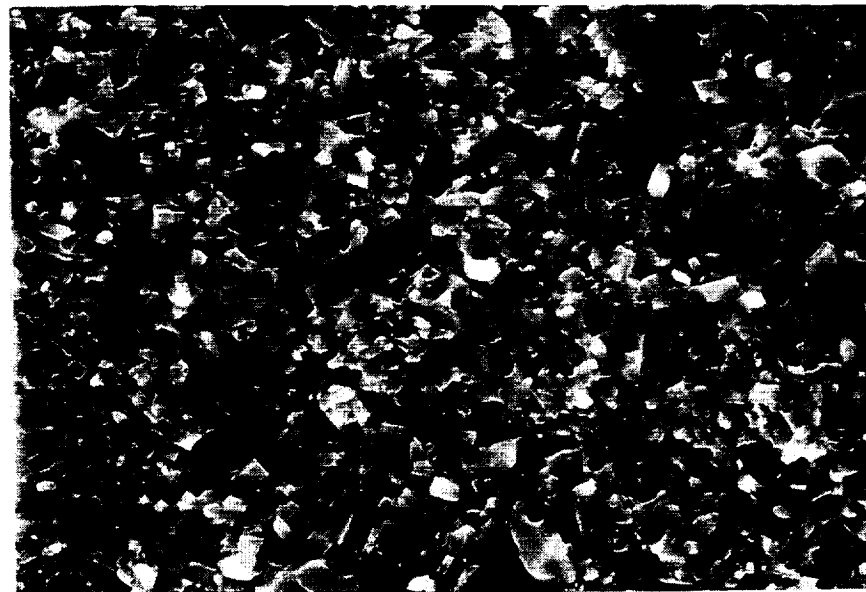
Figure 4.16(b): Fracture surface SEM micrographs taken from Region 2 before and after replication.



10 μm

[before]

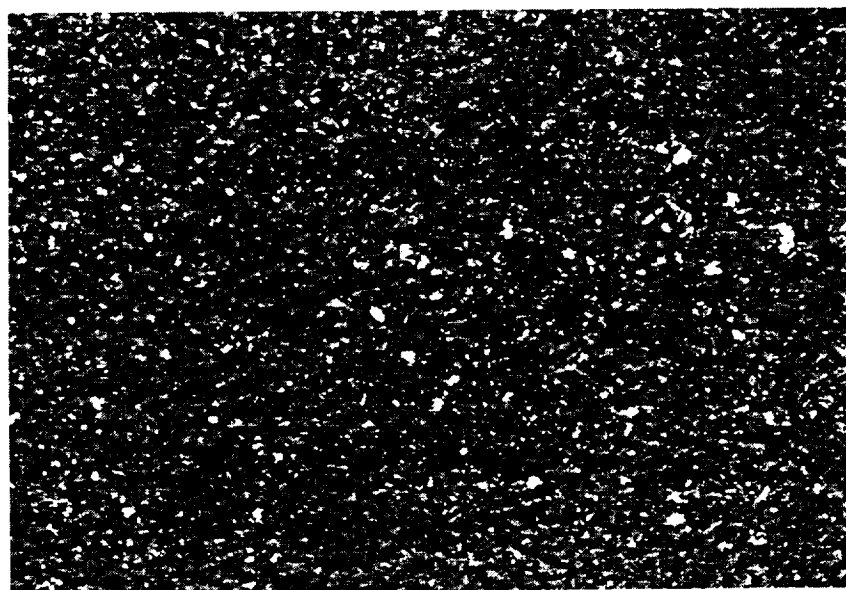
\rightarrow



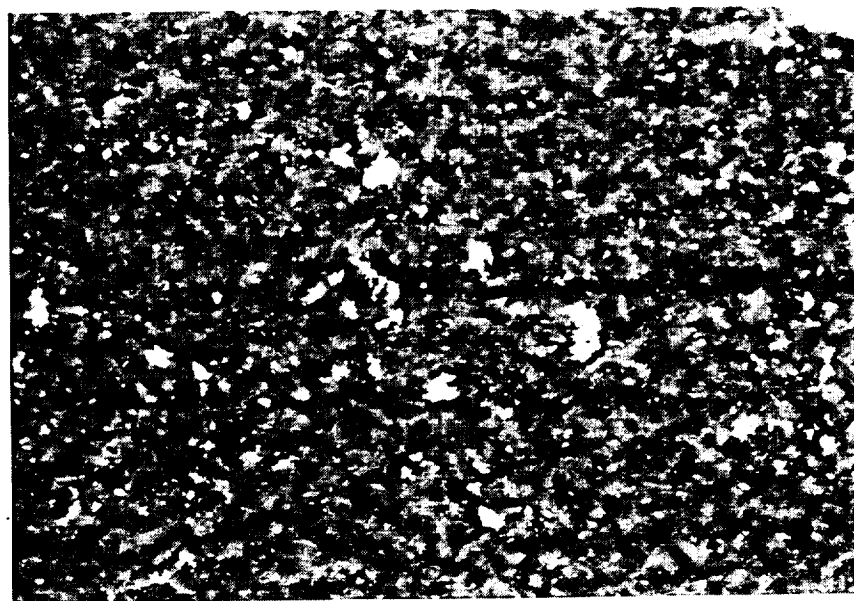
10 μm

[after]

Figure 4.16(c): Fracture surface SEM micrographs taken from Region 3 before and after replication.



(a)

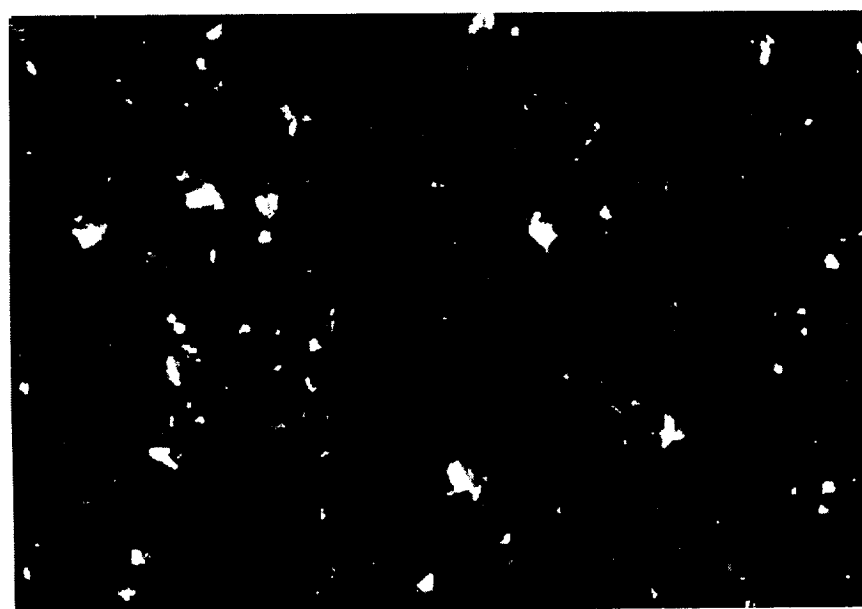


(b)

Figure 4.17: Low contrast backscatter electron images demonstrating that a portion of the ceramic debris removed from surface involved agglomerates of many grains. Particles as large as 10 μm are observed at higher magnification in (b).

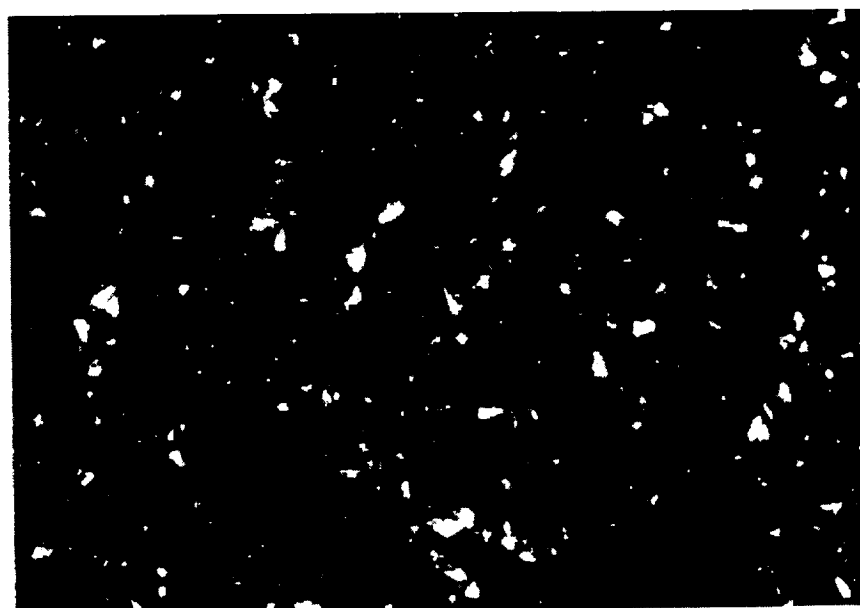
indicating that entire agglomerates are detached from the material during fracture. Special care was then exercised to remove the influence of surface texture from backscatter micrographs such that image analysis techniques could be used to estimate density distributions and particle size counts. Once surface texture was removed from backscatter images, a trend to the density of debris within the slow growth band could not be determined. However, it is important to note that filtering out surface texture also required masking out the influence of small sized debris, specially when magnifications were low ($<500\times$), so some information was likely lost and numerical results may be conservative.

Figures 4.18(a) through 4.18(d) are the digitized images obtained from the high magnification ($1500\times$) backscatter micrographs taken within the slow growth region and used for image analysis. Figures 4.18(a) and 4.18(b) were taken from regions near the arrest line and demonstrate the sharp increase in debris density associated with re-initiation of slow growth. Figure 4.18(b) is typical of the digitized images taken within the slow growth band. Figures 4.18(c) and 4.18(d) are images taken near the end of slow growth when subcritical crack velocities had increased to more than $20\text{ }\mu\text{m/sec}$. These two micrographs show the decrease in particle density noted with the onset of dynamic initiation. Several of these backscatter images taken within slow growth band were analyzed for distribution information. It was determined that, as an average, the white areas identifying particles accounted for more than 3 percent of an imaged surface, which compared to less than 0.5 percent outside subcritical crack growth bands. Slightly less than 95 percent of the particles making up the white areas within the slow growth region had sizes of $2.0\text{ }\mu\text{m}$ or less which scales well with the grain size of the material.



20 μm

(a)



20 μm

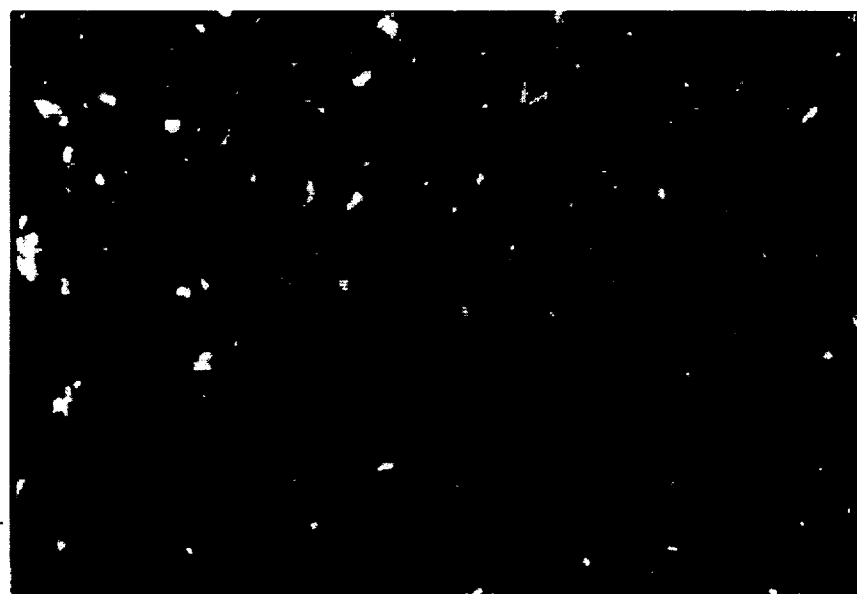
(b)

Figure 4.18: Digitized backscatter images used for debris particle counts and size estimations (920130_2). Image (a) was taken immediately before SCG and comparison with (b) taken immediately after shows the debris increase related with SCG [figures 14.18(c) and 14.18(d) next page].



20 μm

(c)



20 μm

(d)

Figure 4.18: [continued] Images (c) and (d) were taken before and after dynamic initiation exhibit the sharp decreases noted for dynamic propagation.

The other 5 percent of the particles had sizes ranging from 2.5 to 10 μm with an average of approximately 5 μm .

As noted, the existence of surface debris was unexpected and, although efforts were given to investigating its source, there is much that can be done in this area as future work. The source of this debris and how it affects fracture resistance is not known. It could be that surface debris represents the ceramic material which was detached by bridging mechanisms at the crack tip. It is equally likely that debris could be ceramic material which was loosened by microcracking and then exposed by crack propagation. In either case, the existence of this debris, and the fact that a higher density is produced during subcritical growth, implies that discontinuities extend beneath the apparent fracture surface and play an important role in crack growth resistance for NC-132.

Another interesting result was that after replicating the fracture surface, the surface morphology within both the slow and fast growth regions was preserved. This permanence of texture supports the conclusion that the roughness of a surface is a direct product of the fracture process, and that a change in fracture process will produce a distinct change in surface morphology.

Fracture Surface Texture

Even though filtering backscatter images to remove surface roughness effects may have led to conservative debris counts, the lack of a density trend was not expected. Since a distribution was noted earlier, it was suggested that it may be caused by surface roughness rather than the particle distribution. It was hoped that information concerning a roughness trend within the slow growth band could be extracted by imaging the

topography of the fracture surface. Elevation measurements were taken by scanning the surface from immediately before arrest, through slow crack growth and into dynamic initiation.

Surface topographies were acquired using an optical based noncontacting surface tracer. The measuring device uses coherent light from a helium-neon laser focused onto a two dimensional surface. The reflected image is monitored with a charged couple device (CCD) as a two dimensional array of pixel intensities while the specimen stage is automatically moved through focus. The CCD array had a resolution of 768 pixels in the direction of crack propagation and a transverse resolution of 240 pixels. Stage position is monitored simultaneously with pixel intensities and the point of maximum intensity signaled that the respective point was in focus and established its surface elevation. The manufacturer's (Laser Tech,1991) stated accuracy is $0.01\ \mu\text{m}$ for optimum conditions, however, the actual accuracy depends on the characteristics of the surface being measured which may include texture, reflectivity and transmissivity. Precise positioning of the specimen stage was accomplished through computer controlled servo-electronic motors.

A strip of the fracture surface $110\ \mu\text{m}$ wide and $1000\ \mu\text{m}$ long was imaged as ten individual areas mapped together as shown in figure 4.19. Individually sampled areas were $110\ \mu\text{m}$ wide in the transverse direction of crack propagation and $100\ \mu\text{m}$ wide parallel to the direction of propagation. A rectangular array of data points for the 622 by 218 pixels were taken for each individual area and surface elevations were stored digitally as two-byte integers. Patching the ten $110 \times 100\ \mu\text{m}$ areas together to obtain the $1000\ \mu\text{m}$ long strip was accomplished using a digital computer. A grey-scaled image

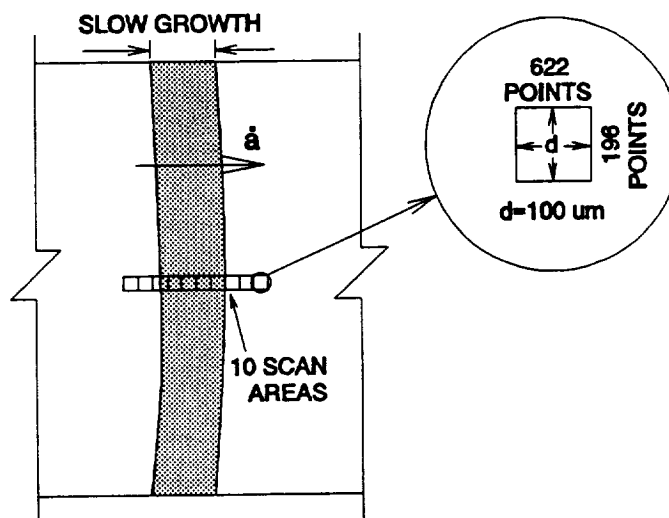


Figure 4.19: Scanning laser microscope topography procedure used to obtain quantitative elevation information from fracture surface (920130_2).

of the fracture topography for the imaged strip is given in figure 4.20. Surface elevations were scaled dark to bright for minimum to maximum peak values within the entire scan. The calculated range of elevations (dark to bright) was $1200 \mu\text{m}$. The approximate positions for crack arrest (re-initiation of slow growth), and dynamic initiation are given in the figure. Since the strip is only a narrow sample of the crack band and the data was generated at high magnifications (approximately $500\times$), there is some uncertainty associated with the exact position of dynamic arrest and initiation.

Surface roughness calculations were performed digitally using the computer data files stored for the entire strip. The root mean square method (ANSI, 1985) was used to calculate a roughness value for selected one-dimensional traces. An average of the roughness values was used to estimate the texture of a two-dimensional area. The $110 \times 1000 \mu\text{m}$ strip was subdivided into 28 adjoining areas having a transverse width of $110 \mu\text{m}$ and a parallel length of $50 \mu\text{m}$. Roughness values were calculated for each of the

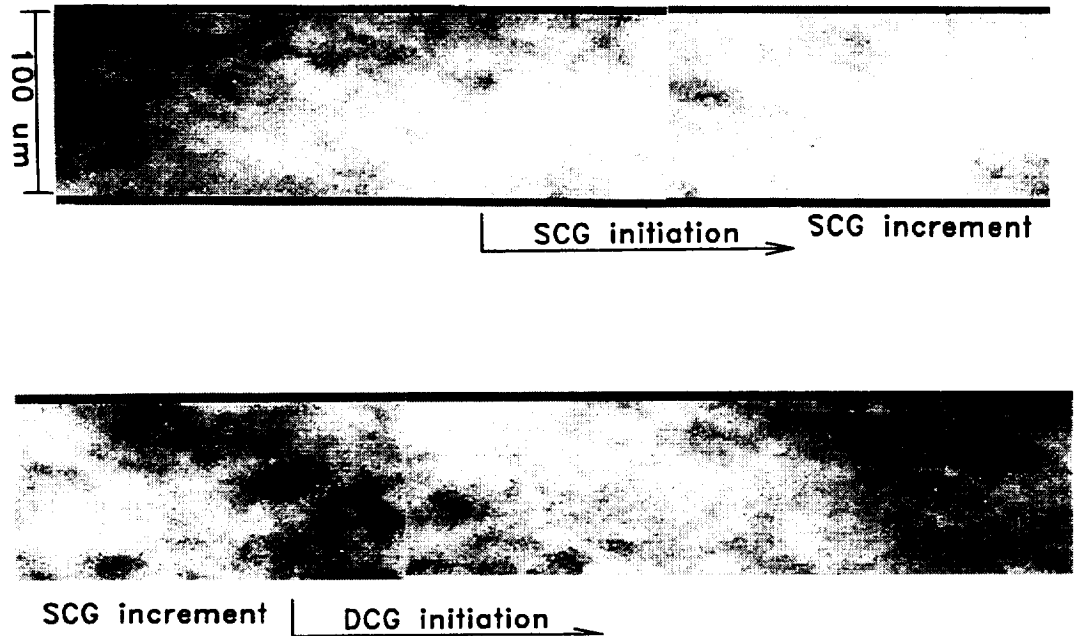


Figure 4.20: Grey scaled topography image of fracture surface through SCG band. Black is low white is high with total elevation change of 120 μm .

218 parallel scan lines and 311 transverse scan lines. The average of these values was then used as a representative roughness measure for each subdivided surface. The length of each scan line was 50 μm for both the parallel and transverse calculations. A plot of the average roughness for each area is given in figure 4.21 for both the transverse and parallel scan lines.

Roughness calculations for both the transverse and parallel scan lines, summarized in table 4.4, demonstrate a similar trend of increased roughness during slow growth. Surface roughness transverse to crack propagation increased from 5.0 μm during dynamic extension to 6.5 μm during slow growth. Scatter in roughness calculations was noted to be less than the increased trend observed as can be seen in figure 4.21. Surface

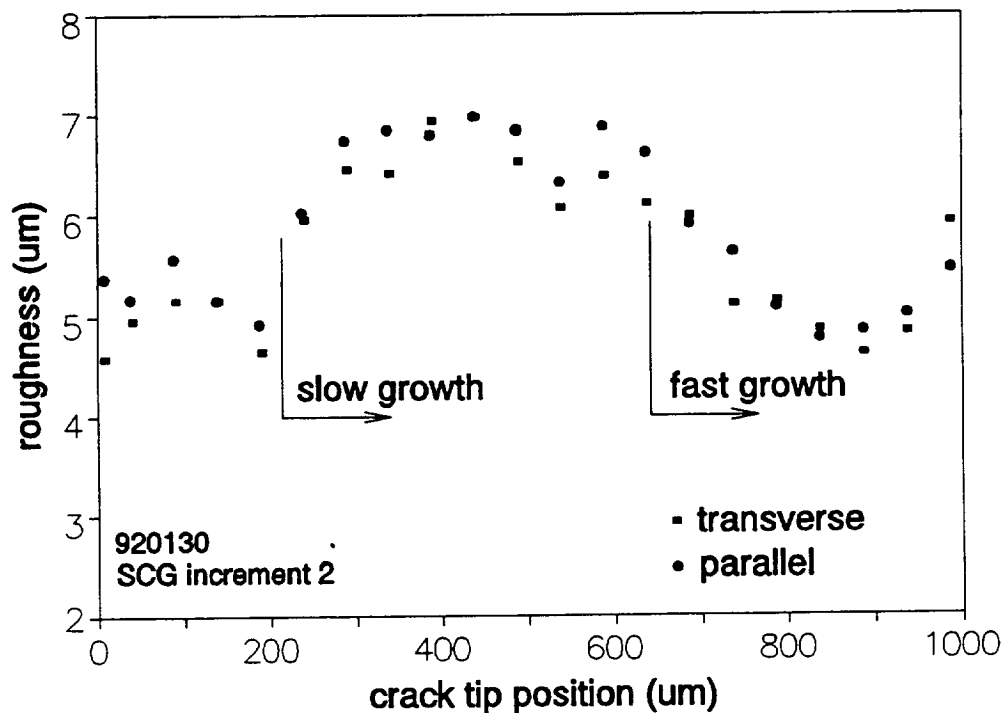


Figure 4.21: Surface roughnesses using individual scan lines with a 50 μm length. Scan lines taken both parallel and transverse to direction of crack propagation.

roughness calculations using trace lines parallel to the crack propagation direction also averaged 5.0 μm during fast extension and were noted to increase to 7.0 μm during slow growth. Scatter in the calculated results for the parallel trace lines was again less than the observed trend

Table 4.4 Surface Roughness Measurements

CRACK SPEED	AVERAGE ROUGHNESS (μm)	
	PARALLEL	TRANSVERSE
FAST (km/SEC)	5.0	5.0
SLOW ($\mu\text{m}/\text{SEC}$)	7.0	6.5

The average roughness during both fast and slow growth is larger than the average grain size which may support the suggestion that several grains act dependently

during fracture. Although roughness calculations for the transverse direction gave some indication that roughness decreased during slow crack growth extension, the results for parallel scan lines revealed essentially a constant roughness during slow extension. It is interesting that both the parallel and transverse roughness values increase sharply immediately after the arrest position, when slow crack growth is beginning, but reduce more gradually after dynamic initiation. This is best observed in the parallel results where, the increase in roughness after arrest occurs in less than 100 μm , whereas the decrease in roughness at dynamic initiation occurs over a distance of more than 200 μm . Such a transition might be expected given the trend observed in backscatter image presented in figure 4.14. Surface topography results are, however, preliminary and additional analysis would be necessary for more definitive statements concerning roughness trend beyond the reported increase from slow to fast crack growth. Caution must be exercised in the interpretation of surface topography and its relationship with the fracture process. Though it is generally recognized that the fracture surface texture and fracture process are related, the form of this relationship is not known. Furthermore, although the elevation data taken from the fracture surface for this study is considered accurate, the amount of information obtained in this study is not extensive enough for more substantive discussions. Only a narrow strip of the fracture band was used (actually less than 5 percent) and large sized surface patterns could not have been detected. Imaging larger areas will require significantly more computer storage room and software development effort (the 110 x 1000 μm strip generated a data file which was more than 3 megabytes in size and the software written to accurately patch small areas together required several hundred programming lines).

It is worth noting that evaluations for critical fracture energies may, in principle, be compared to the energy associated with the newly created free surfaces, γ_s . The energy required to propagate the crack is estimated from equation 3.6 using Griffith's specific fracture surface energy term, γ , which represents the average energy dissipated per unit surface area created. At dynamic initiation γ averaged 34 J/m². Crack propagation is essentially intergranular and the fractured material is primarily nitride-based glasses which may have a free surface energy comparable with a high strength glass at 1 J/m² (Wiederhorn,1969). If direct comparisons are made, the average measured specific fracture energy is at least 30 times greater than the expected free surface energy. In reality, however, such comparisons cannot be made because a fracture surface is not ideally flat for most brittle materials, and the projected surface area is significantly smaller than the actual area created if surface tortuosity is included.

Unfortunately, accounting for the effects of surface tortuosity in Griffith's energy term is not simply a matter requiring a more detailed estimation for the actual area created. The procedure for assessing fracture area is not deterministic. The fractured surface of most brittle polycrystals are fractal in nature and it is known that surface metrics are scale dependent (Mandelbrot,1984). Generally, approximations for created surface area increase substantially with a decrease in measurement scale, and there is no established limit which can be used to define fracture area absolutely. The science of Fractal Geometry is itself very new (Mandelbrot,1982) and theories used to characterize fractal geometries are likely to impact fracture research in the future. Present studies however have produced mixed results and the relationship between fractal science and fracture mechanics is not clear (Baran,1992;Mecholsky,1989;Dauskardt,1990).

Therefore, utilizing the horizontally projected area of a fracture surface is currently the easiest and most effective means of quantifying fracture energy.

There are other issues concerning estimations for fracture energies which make a comparison with free surface energy difficult to interpret. Fracture energies are determined using continuum mechanics concepts which average in the effects of additional energy dissipating mechanisms. Included is the generation of heat, phonons, visco-plastic flow, and other non-reversible mechanisms. Therefore, even if an appropriate method of accounting for surface tortuosity is established, these other energy dissipation mechanisms must be isolated before a comparison with the free surface area of the material fractured can be accomplished.

SUMMARY

The experimental fracture study using the modified SPL specimen and the NC-132 material revealed that increments of slow crack growth always preceded increments of dynamic crack growth and subsequent crack arrest occurred without interference from reflected stress waves. There was some initial concern whether interrupted crack growth behavior for NC-132 was an artifact of friction at the pin-to-specimen interface. However, it was noted that such behavior had not been observed for either the Al_2O_3 , or a silicon carbide material tested separately, even though the same procedure had been employed. Furthermore, modifications to the interface did not alter the NC-132 material's fracture behavior. A gold surface film placed on the internal surface of the receiver hole, used to cushion surface asperities between the steel pin and the ceramic specimen, did not alter the fracture performance of the NC-132 material. Similarly,

surface lubricants such as silicon oil and petroleum oil applied to the interface surface before the steel pin was inserted had no effect on fracture behavior.

Finally, the observed kinetics of subcritical crack growth indicate that the process of interrupted growth was a genuine fracture process for the NC-132 material. During each increment of subcritical growth, crack velocity was observed to have a smooth monotonic increase up to dynamic initiation. If a sudden supply of elastic energy was released by the pin-to specimen interface, one would expect a sharp increase in crack tip velocity producing more erratic kinetics during subcritical crack growth. Such erratic behavior had not been observed for any test case, including those where interfacial films were applied to further minimize pin-to-specimen friction.

It is worth noting that the interrupted crack growth behavior observed for the NC-132 material has also been documented by Salem and Shannon (1987) using the same material with the chevron-notched short bar fracture geometry. In their studies multiple increments of subcritical crack growth, dynamic initiation and subsequent growth with arrest were observed, and increments of subcritical crack growth were associated with changes in surface morphology. This study supports the conclusion that the fracture behavior observed for the NC-132 in this study represents a true response from the material which is unaffected by the pin-to-specimen interface. Slow crack growth increments were associated with both an increasing crack-tip velocity and increasing fracture resistance. The ERR at dynamic initiation was, on the average, 40 percent greater than the average energy release rate required to establish slow crack growth after arrest. Both dynamic initiation and arrest occur abruptly and leave distinct evidence of their occurrence on the fracture surface. The increase in fracture resistance during slow

growth is associated with an increase in fracture surface tortuosity and the presence of ceramic debris on the fracture surface. Both the surface debris and the surface roughness relate to the process of fracture during slow crack growth.

CHAPTER V

Modeling of Experimental Results

INTRODUCTION

One of the primary interests for this research was to establish the existence of subcritical crack growth prior to fracture, and provide the means for predicting its influence on the fracture response of brittle materials with a physically based model. The experimental studies conducted using the NC-132 material established the systematic existence of subcritical crack growth prior to dynamic initiation. For this material, increments of subcritical crack growth lead to increases in fracture resistance and some of the mechanisms which contributed to this increase have been identified. A remaining task is to integrate the results of the experimental program in a predictive model.

An interesting feature of the NC-132 material's fracture response was the interruption of subcritical crack growth with dynamic initiation, partly because it was not expected given the nature of the test setup. The SPL specimen was specifically designed to promote the conditions for stable crack growth. The supply of energy from the elastic system decreases with crack extension, therefore, subcritical crack growth should be present throughout the test range of the SPL specimen. Although the measured increase in fracture resistance during subcritical growth certainly plays a role in dynamic initiation event, it cannot, by itself, explain why the fracture process becomes unstable. The increase in material resistance leads to an increase in the force required to drive the crack forward, but the supply of energy from the elastic system still decreases with each incremental advance of the crack, so the fracture process should remain stable. The

transition from stable to unstable conditions requires a surplus supply of elastic energy and, for the SPL test configuration, this is possible only if the material's fracture resistance suddenly decreases during subcritical crack growth.

In order to provide a mechanism for a decrease in fracture resistance, the model proposed below utilizes the concept of a zone of damaged material ahead of the main crack tip. Formation of the zone's size and the density of its damage is assumed to be stochastic. The density of damage is captured by decreasing the elastic modulus of the material within the zone. Although the damage mechanism is not defined, it is imagined that an array of microcracked material will have the same modeled affect, and the existence of surface debris is taken as evidence of multiple cracking. Therefore, the fracture model must account for the influence of a damage zone and subcritical crack growth in the evaluation of probabilities for critical fracture parameters. The specific features of the NC-132 experimental results which attract an interest are the sequence of dynamic initiation and arrest, the process of subcritical crack growth, and estimations for critical values for the energy release rate (ERR) at dynamic initiation and arrest. A review of the probabilistic models discussed previously revealed a general lack of models which account for subcritical crack growth. Of these, the Statistical Fracture Mechanics (SFM) theory was identified as the only approach which specifically addresses the influence of subcritical crack growth during brittle fracture.

PROBABILITY THEORY FOR SUBCRITICAL CRACK GROWTH

Single Path SFM Theory

Developing a physically based probabilistic model which incorporates the potential

for subcritical crack extension is accomplished by addressing the following question: what is the probability that a crack will extend from point \underline{x} through \underline{X} in an elastic medium having a fluctuating strength field given the prescribed loading condition?. The problem is formulated by considering that crack advance from point \underline{x} occurs as a sequence of local failures ahead of the main crack tip, and each local failure is a random event controlled by fluctuations in material strength. Since the fluctuations in strength are spatially distributed in the elastic solid, the final crack path from point \underline{x} through \underline{X} becomes a random trajectory which is selected stepwise from a large set of virtual trajectories as shown in Figure 5.1.

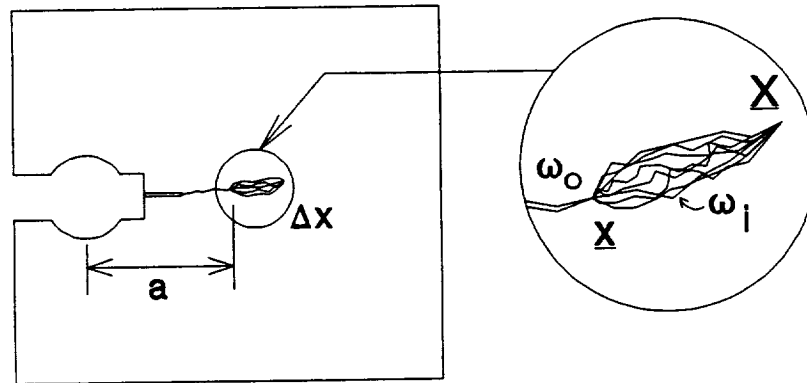


Figure 5.1: Potential crack trajectories from point \underline{x} to \underline{X} having equal probabilities of occurrence. Event of one path excludes the occurrence of other potential paths.

Each virtual trajectory from the set of all possible trajectories connecting points \underline{x} and \underline{X} is considered to be equally probable. If it is assumed that the stepwise formation of one crack path, ω_k , excludes the formation of other paths, ω_m ($k \neq m$), then only one unique crack path, ω_k , will be formed from \underline{x} through \underline{X} and the probability of its formation, P_{ω_k} can be written as

$$P_{\omega_k} = P\{\underline{X}, \underline{X} | \omega_k\} \cdot P\{\omega_k\} \quad 5.1$$

Here $P\{\omega_k\}$ is the probability that ω_k is selected and $P\{\underline{X}, \underline{X} | \omega_k\}$ the conditional probability that the crack will extend beyond \underline{X} along the path ω_k . In engineering terms, the conditional probability becomes an integral statement of Griffith's energy criterion for crack extension. That is, the energy release rate along the path ω_k must exceed the energy required to form two new surfaces, $[G(\xi_i) \geq 2\gamma(\xi_i)]$, at every position, ξ_i , along the trajectory ω_k . Crack extension is considered to occur as an ordered sequence of 'n'

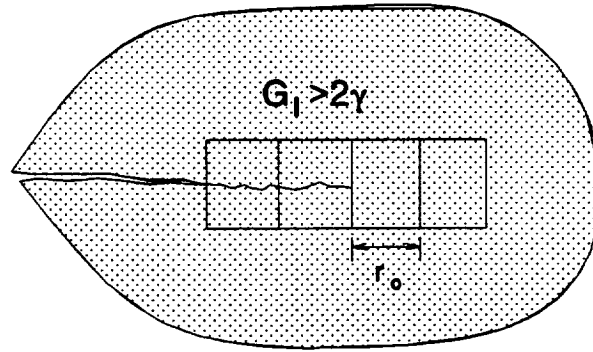


Figure 5.2: Stepwise sequential failure of material in front of the crack tip meeting the failure condition $G_I(x) > 2\gamma(x)$.

elementary steps as shown in figure 5.2, therefore the conditional probability is the probability of the product of events

$$P\{\underline{X}, \underline{X} | \omega_k\} = P\left\{\bigcap_{i=1}^n G_I(\underline{X}_i | \omega_k) > 2\gamma(\underline{X}_i)\right\} \quad 5.2$$

where ξ_i is a point along the path ω_k and $G_I(\xi_i | \omega_k)$ is the energy release rate evaluated for a crack with its tip at point ξ_i on trajectory ω_k . The condition that all preceding events have occurred is evaluated through the energy release rate calculation. If it is

assumed that the probability for arrest is small for each increment of crack advance, the relationship $(1-\epsilon)^n \approx \exp(-n\epsilon)$ for $\epsilon \ll 1$ can be used, and the conditional probability given in 5.2 (see Chudnovsky and Kunin [1987] for details) can be approximately written as

$$P\{\mathbf{X}, \mathbf{X}|\omega_k\} = \exp\left[-\int_{\mathbf{x}}^{\mathbf{X}} P\{2\gamma(\mathbf{X}) > G_I(\mathbf{X}|\omega_k)\} \frac{d\mathbf{X}}{r_0}\right] \quad 5.3$$

It is assumed that γ is a statistically homogeneous random field having a correlation distance, r_0 , which is much smaller than the crack size. This correlation distance represents the physical scale of material inhomogeneity, and at distances greater than r_0 the strength field assumes an independent values. The Weibull distribution of minimal values from the theory of statistics of extremes [Leadbetter, 1983] is used to represent random values of γ for each point along a given crack trajectory to reflect that the crack selects the path of least resistance. Therefore the strength field can be represented as

$$F(\gamma) = \begin{cases} 1 - \exp\left\{-\left[\Gamma\left(1 + \frac{1}{\alpha}\right) \frac{\gamma - \gamma_{\min}}{\gamma^* - \gamma_{\min}}\right]^\alpha\right\}, & \gamma > \gamma_{\min} \\ 0, & \gamma < \gamma_{\min} \end{cases} \quad 5.4(a)$$

where $\alpha > 0$ and $\Gamma\left(1 + \frac{1}{\alpha}\right)$ is the Γ -function. The values α , γ^* , and γ_{\min} are empirically derived constants. The values γ^* , and γ_{\min} are the mean and minimum values of the strength field, respectively.

Since the formation of each increment of the main crack excludes the formation of other cracks, only one crack trajectory will develop between points \underline{x} and \underline{X} in a single test, therefore the formula of total probability can be used to reformulate the crack propagator as

$$P_{\Omega_{\underline{x}, \underline{X}}}(\underline{X}, \underline{X}) = \sum_{k=1}^n P\{\underline{X}, \underline{X} | \omega_k\} \cdot P\{\omega_k | \Omega_{\underline{x}, \underline{X}}\} \quad 5.5$$

The elastic solid is considered to be a continuum and the set, $\Omega_{\underline{x}, \underline{X}}$, of virtual trajectories, ω_k , is uncountable, consequently the discrete sum in 5.5 becomes the integral sum

$$P_{\Omega_{\underline{x}, \underline{X}}}(\underline{X}, \underline{X}) = \int_{\Omega_{\underline{x}, \underline{X}}} P\{\underline{X}, \underline{X} | \omega_k\} d\mu(\omega) \quad 5.6$$

where $d\mu(\omega)$ is the probability measure on $\Omega_{\underline{x}, \underline{X}}$. Substituting 5.3 into 5.6 provides

$$P(\underline{X}, \underline{X}) = \int_{\Omega_{\underline{x}, \underline{X}}} \exp\left(-\int_{\underline{x}}^{\underline{X}} P\{2\gamma(\xi) > G_I(\xi | \omega)\} \frac{d\xi}{r}\right) d\mu(\omega) \quad 5.7$$

The form of the crack propagator given for the continuum based model provides an effective means for evaluating the probabilities of fracture events corresponding to single crack path formation from point \underline{x} to \underline{X} . However, it was proposed that the fracture behavior of NC-132 included aspects which could be modeled with a zone of microcracked material ahead of the main crack. In this case, formation of one crack no

longer precludes formation of other virtual cracks and the existence of multiple cracking must be addressed for model development.

Multiple Cracking SFM Theory

Evaluating the probabilities associated with the formation of several cracks requires a separate formulation of the crack propagator, $P^*(\mathbf{x}, \mathbf{x})$, which accounts for multiple cracking events A_k and A_m ($k \neq m$). Evaluations associated with multiple cracking can be simplified if cracking events A_k and A_m can be treated independently. Unfortunately, for real materials multiple cracks are closely spaced and the interaction between them cannot be neglected. Therefore cracking events A_k and A_m strictly speaking are not independent and a modified technique for evaluating probabilities is required. The presence of secondary cracks can be accounted for by including their effect on the stresses applied to the main crack. However, even if the spacial parameters of the secondary cracks are known, evaluating the influence of multiple cracks is a difficult problem requiring the solution of interaction equations which are highly nonlinear. Since little is known concerning secondary cracking, an approach based on the Mean Field approximation is proposed (Chudnovsky and Wu, 1990). Such an approach accounts for the influence of secondary cracks by replacing them with their effective cumulative stress which acts on the main crack line. Chudnovsky and Wu used this approach and demonstrated the presence of a shielding stress provided most of the secondary cracks are aligned parallel. As a crack propagates farther into a microcrack array, shielding increases and, without additional external loading, crack driving forces decrease. Following their work the observed experimental behavior of the apparent ERR

for the NC-132, i.e. a build up of fracture resistance, together with the fractographic evidence of possible secondary cracking, it is proposed that the cumulative shielding effect of secondary cracking can be modeled as soft elastic inclusion as shown in figure 5.3. The elastic inclusion has an elastic modulus which is less than the original undamaged material. Such an approach allows propagation of each crack trajectory within a damaged zone of material to be treated as a statistically independent event.

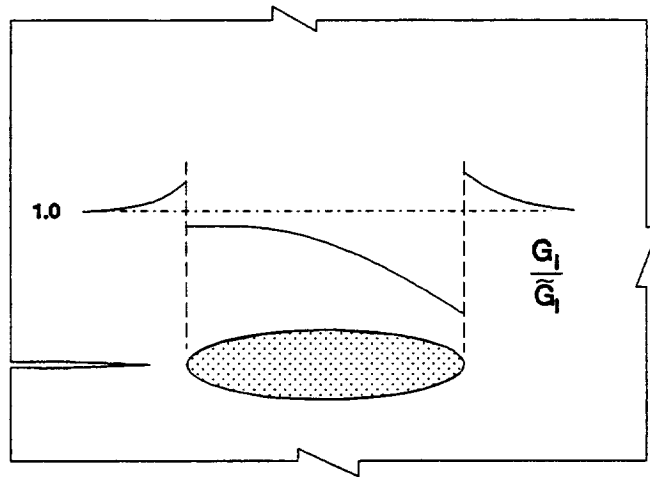


Figure 5.3: Apparent energy release rate response normalized by actual energy release rate for a crack tip propagating through an elastic inclusion.

The ERR solution for a main crack propagating through a soft elastic inclusion has recently been obtained by the finite element technique (Li, 1993) and the dependency of the actual ERR, G_I , on crack tip position is given in figure 5.3. Here G_I is normalized by the ERR for the same crack tip position with no inclusion, \tilde{G}_I . Properties of the elastic solution which are important for modeling the experimental behavior of the NC-132 material are the monotonic decrease of the ERR within the soft elastic inclusion, and the stepwise increase in the ERR as the crack tip crosses the

inclusion's far boundary. Throughout the inclusion the actual ERR is less than that for the homogenous solid which captures the shielding effect of an array of microcracks. Several inclusion geometries were considered for finite element analysis and all possessed the behavior in actual ERR demonstrated in figure 5.3.

Distribution Density for Arrest ERR

The form of the Crack Propagator given in expression 5.7 can be re-written as

$$P(\underline{x}, \underline{X}) = \int_{\Omega_{\underline{x}, \underline{X}}} \exp\left(-\int_{\underline{x}}^{\underline{X}} U[\xi, \omega(\xi)] \frac{d\xi}{r_0}\right) d\mu(\omega) \quad 5.8$$

where $U[\xi, \omega(\xi)]$ is the probability for crack arrest at each position ξ . In order to evaluate the statistical distribution for the ERR at arrest, G_I^a , a distribution for the depth of crack penetration must be first constructed. This is accomplished by limiting crack propagation to only rectilinear extension, i.e. $\omega(\xi) \equiv 0$, which is termed the zeroth approximation for the SFM theory. For this approximation the functional integral in 5.8 simplifies and the probability for crack propagation from $\underline{x}=(a,0)$ to point $\underline{X}=(x,0)$ becomes

$$P\{(a, 0) ; (x, 0)\} = \exp\left(-\int_a^x U(\xi) \frac{d\xi}{r_0}\right) \equiv P_0(x) \quad 5.9$$

$P_0(x)$ expresses the probability that the crack will advance by a distance $\overline{x-a}$ or farther from position $\underline{x}=(a,0)$, therefore, $\tilde{P}_0(x) = 1 - P_0(x)$ is the distribution function for the

crack arrest length. The distribution function $\tilde{P}_0(x) = 1 - P_0(x)$ can be used to evaluate the probability density function for the crack arrest location, $f_a(x)$, as

$$f_a(x) = \frac{d(1 - P_0(x))}{dx} = P_0(x) U(x) \frac{1}{r_0} \quad 5.10$$

The arrest ERR, G_I^a , can be evaluated for a crack length x by the deterministic function

$$G_I^a = \frac{(V_1^a)^2 E_0}{W} \cdot \Psi^2\left(\frac{x}{W}\right) \quad 5.11$$

where E_0 is the elastic modulus of the homogeneous solid, W is the specimen width, and $\Psi\left(\frac{x}{W}\right)$ is the dimensionless monotonically decreasing function given in table 3.4. The apparent ERR, \tilde{G}_I , can be adjusted to be dimensionless, $\tilde{G}_I = \frac{G_I W}{(V_1)^2 E}$, such that

$$\tilde{G}_I = \Psi^2\left(\frac{x}{W}\right) \quad 5.12$$

The probability density function for the ERR at arrest can be then given as

$$f_a(\tilde{G}_I) = f_a(x) \frac{1}{\left(\frac{d\tilde{G}_I}{dx}\right)} = f_a(x) \left[\frac{W}{2\Psi\left(\frac{x}{W}\right) \cdot \Psi'\left(\frac{x}{W}\right)} \right] \quad 5.13$$

Equation 5.13 expresses the probability density function for the ERR for the SPL configuration given that the function $\Psi\left(\frac{x}{W}\right)$ is taken from the finite element solution for the stress intensity factor given in table 3.4. The arrest probability density function for

crack arrest length, $f_a(x)$, must be evaluated from the Crack Propagator given in 5.9, and, provided fracture is ideally brittle, the procedure involves a straight forward substitution, assuming the arrest condition $\tilde{G}_I(x) = 2\gamma$, of the deterministic function $\tilde{G}_I(x)$ for γ in the strength field distribution such that

$$U(x) = \exp - \left[\Gamma \left(1 + \frac{1}{\alpha} \right) \cdot \frac{\tilde{G}_I(x) - \gamma_{\min}}{\gamma^* - \gamma_{\min}} \right]^\alpha \quad 5.14$$

Unfortunately, for increments of subcritical growth, use of the Mean Field approach to account for the damage zone modifies the driving forces such that they can no longer be considered deterministic. Damage zone formation is also a stochastic process and the actual ERR, $G_I(x)$, for increments of subcritical crack extension contains scatter. Since variation in $G_I(x)$ are not directly accounted for in the development of the Crack Propagator, a modified approach which will include these variations must be pursued.

MONTE CARLO METHOD FOR SUBCRITICAL CRACK GROWTH

The Crack Propagator defined in equation 5.13 is used as one of the main building blocks of SFM theory and it can be used to develop expressions for the probability of crack initiation or crack arrest, as well as statistical distributions for critical fracture toughness parameters. The main difficulty of applying the SFM theory is evaluation of the Crack Propagator because it involves a functional integration. Analytical treatments can be used to reduce integration to solving partial differential, or even ordinary differential equations, but such a simplification requires certain restrictive assumptions. Namely, the set of admissible crack trajectories, $\Omega_{x,x}$, must belong to a

class of Wiener-type processes. If this assumption can be made, then the functional integration can be reduced to solving diffusion-type differential equations. Unfortunately, a Wiener-type random function for a crack trajectory, $\omega(x)$, may not always describe experimental observations adequately (Kunin and Gorelik, 1991). Furthermore, even if a Wiener-type random function is assumed for crack path formation, there is no general solution for the Crack Propagator, and each evaluation must be adapted to a particular physical problem. Without this assumption, evaluation of the Crack Propagator becomes a very difficult problem.

For the reasons given above, it is proposed here that a numerical technique based on the method of Monte Carlo simulations can be used together with the SFM framework to model the brittle fracture behavior of the NC-132 material. The central idea of this approach is to substitute the analytical evaluation for the probability of crack extension along every virtual trajectory with the average frequency of events from computer simulations of a set of N virtual crack paths from point \underline{x} to \underline{X} . In principle, as the number of computer simulations increases the simulated frequency should converge to the value of the Crack Propagator for the actual experimental setup. Selected fitting parameters, which are physically based, can be adjusted such that computer simulated results for statistical parameters, such as critical toughness or critical crack length, agree with experiment.

Model Development for Application of SFM

For simplicity, actual crack paths are approximated by a straight crack having the same horizontal projection along the x axis, which is consistent with the zeroth

approximation used above for the SFM theory. This approach not only simplifies the problem, it also allows a direct comparison of modelling results for ERR with experimental ERR values. This comparison is accomplished through what has been defined as the apparent ERR, $\tilde{G}_I(x)$, which is based on estimations for the critical CMOD's and crack lengths with the finite element solution for the SPL specimen geometry assuming a perfectly elastic homogeneous solid.

For model development, it is assumed that the damage zone is present immediately after arrest. The apparent ERR, $\tilde{G}_I(x)$, within the inclusion region is approximated as linear for simplicity. The validity of the linear substitution for $\tilde{G}_I(x)$ is obvious from figure 4.8. When the crack tip position is within the damage zone, the actual ERR, $G_I(x)$, is estimated by reducing the apparent value, $\tilde{G}_I(x)$, with a correction factor $\Phi(x)$ which accounts for shielding of the soft inclusion such that

$$G_I(x) = \tilde{G}_I(x) \cdot \Phi(x) \quad 5.15$$

This correction factor is approximated by the function

$$\Phi(x) = \frac{1}{1+bx} \quad 5.16$$

where b is one of the fitting parameters of the model representing the ratio of the inclusion modulus, E_i , to the modulus of the homogeneous solid, E_0 . The average ratio of $\langle b \rangle = \langle E_i \rangle / E_0$ was determined from the computer simulations to be 0.53. When the crack tip enters the inclusion the ERR is close to that for the crack in the homogeneous solid and, for modeling purposes, it is assumed that no change in the ERR occurs at this boundary as shown in figure 5.4.

Another fitting parameter of the model is distribution of traction forces, $\sigma(x)$,

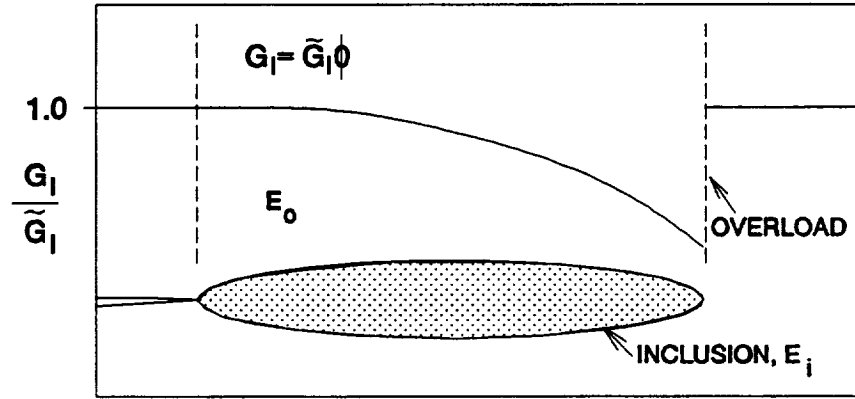


Figure 5.4: Model of the apparent energy release rate for subcritical crack growth used in the Statistical Fracture Mechanics approach.

which acts along the boundary of the damage zone. It is assumed that the variation in $\sigma(x)$ along the central portion of this boundary is small and a crack-face traction force, σ_{tr} , can be utilized in the model to represent the integral average of the boundary traction such that

$$\sigma_{tr} = \frac{1}{\ell} \cdot \int_{x^a}^{x^a + \ell} \sigma(x) dx \quad 5.17$$

where x^a is the crack position after dynamic arrest, and ℓ , is the damage zone length. It is assumed that a unit volume formation of the damage zone dissipates a specific energy ρ^* . This specific energy and the traction stress, σ_{tr} , are used together with an increment of effective strain for formation of damaged material, ϵ_{tr} , to define a dimensionless quantity $\bar{\rho} = \frac{\rho^*}{(\sigma_{tr} \epsilon_{tr})}$ which can be used to establish an equilibrium size, ℓ , for the damage zone. The average value of σ_{tr} is evaluated based on the damage zone equilibrium equation

$$K_I [V_1^{scg}, x^a + \ell] = K_I [\sigma_{tr}, x^a, \ell] \quad 5.18$$

where v_1^{scg} is the CMOD at initiation of subcritical crack growth. The average value of the traction force was determined to be $\langle \sigma_u \rangle = 0.123$ Pa from the computer simulated results. Once the damage zone length is determined from the equilibrium equation, the crack length for dynamic initiation is determined as $x^i = x^a + \ell$. Both fitting parameters σ_u and E_i are statistical quantities having scatter and are modeled as independent Gaussian random variables. Since these parameters are assumed to be normally distributed, they are completely defined by their first two central moments, i.e., the mean and standard deviation.

Modeling Parameters and Procedure

The input parameters for the Monte Carlo simulation include an elastic modulus for the soft inclusion, E_i , a damage zone traction force σ_u which are used to model the damage zone. Other input parameters used for input relate to the strength field which includes values for α and γ_{min} defined by the two parameter Weibull distribution, and a radius of correlation for subcritical crack growth, r_t , and, r_o , for dynamic growth. For the purpose of computer analysis and ease of comparing simulated results to experiment, CMOD values are used as the loading parameter. Crack extension is controlled locally by Griffith's condition $G_I(x_j) \geq 2\gamma(x_j)$ where $G_I(x_j)$ is the deterministic value for the actual ERR and $\gamma(x_j)$ is modeled as white noise having a point wise Weibull distribution. When the crack tip is within the damage zone, the actual ERR is evaluated using the relationship given in 5.15 together with computer generated values for ℓ and b as previously described. The crack is considered to be stationary if $G_I(x_j) \leq 2\gamma(x_j)$. The

condition $G_I(x_j) = 2\gamma(x_j)$ advances the crack a distance equal to the strength field's correlation radius, r_t , and the actual ERR is re-evaluated for a constant V_I at the new position x_{j+1} and then compared to a newly generated value for $\gamma(x_{j+1})$. If the arrest condition, $G_I(x^{j+1}) < 2\gamma(x^{j+1})$, is met then V_I is increased such that $G_I(x^{j+1}) = 2\gamma(x^{j+1})$ and the process is repeated as shown in figure 5.5. The correlation radius of the strength field within the subcritical crack growth region, r_t , is modeled to be less than that for the dynamic region, r_0 , to account for its more tortuous surface. The number of elementary steps, N , for which values of $\gamma(x_j)$ must be generated and comparisons made with the actual ERR can be evaluated as the integer part of $\frac{\ell}{r_t}$.

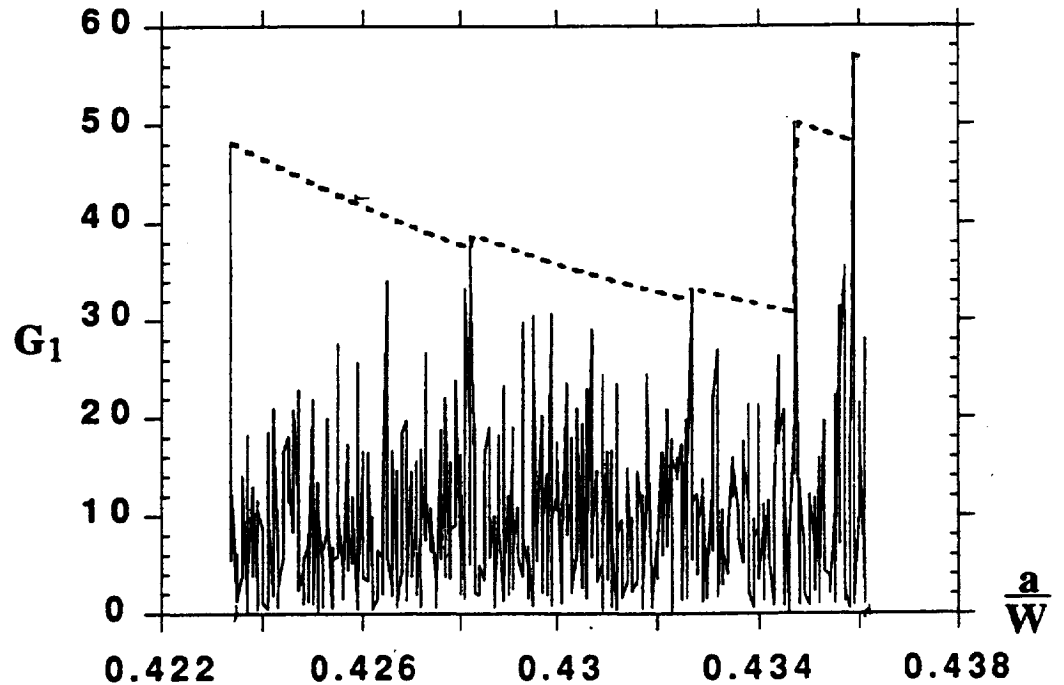


Figure 5.5: Monte Carlo simulation for increments of subcritical crack propagation leading to the overload of elastic energy required for dynamic initiation.

Immediately after the crack tip crosses the far boundary of the damaged zone, the applied ERR experiences a stepped increase equal to

$$\Delta G_I(x^i) = \tilde{G}_I(x^i) - G_I(x^i) = G_I(x^i) \left[\frac{1}{\Phi(\ell)} - 1 \right] \quad 5.19$$

after which dynamic extension is initiated and actual ERR values are then determined from elastic solution for a homogeneous solid without a correction factor. The simulation for dynamic crack advance is accomplished in the same stepwise manner as subcritical crack advance except that the size of each incremental crack step, r_0 , is greater to account for the smoother surface generated during increments of crack extension. Since the fractography studies revealed essentially intergranular fracture during increments of both subcritical and dynamic crack extension, the Weibull parameters, α and γ_{\min} , are the same for subcritical and dynamic propagation. In the actual experiments, dynamic extension did not occur under constant CMOD conditions, as there were small differences between V_1^i and V_1^a for each jump. To account for the additional energy input, dynamic crack arrest was a two step process. Once the condition $G_I(V_1^i, x) < 2\gamma(x)$ is achieved, a small increment of CMOD is added and propagation continues until $G_I(V_1^i + \Delta V, x) < 2\gamma(x)$, where actual arrest occurs. The process for subcritical crack growth is then repeated. Once the ratio of x/W exceeds 0.80 the computer simulation is ended for that computer *experiment* and a new *experiment* is initiated duplicating the actual experimental procedure.

RESULTS AND DISCUSSION

The results from ten *experiments* are compiled and their statistics compared to the actual experimental results. The set of statistical output parameters which is used for comparison includes the critical crack lengths a_i , and a_a , and critical CMOD values V_1^a and V_1^i (or the apparent ERR at arrest and initiation). Obviously there is random scatter in the experimental results and computer simulated results, so the first two moments of each statistic are compared. Adjustments are made to the input parameters until simulated results converge with the experimental observations with satisfactory agreement. Since both the simulated results and the experimental results are stochastic, exact agreement is not realistic and only statistical comparisons are possible. The procedure for selecting specific values for the input parameters is not straightforward. This is because variation of nearly every input parameter affects nearly all components of the output. Therefore, in order to obtain a set of input parameters which will produce output parameters which agree with experiment, a process of trial and error must be employed. An example of the computer generated *experiment* is given in figure 5.6. The final values determined for the list of input parameters is given in table 5.1. The resulting list of output parameters is given in table 5.2 and it can be seen that for a

Table 5.1 Summary of Input Parameters

E_i/E_0	0.53 ¹	0.01 ²
σ_{tr} (Pa)	0.150 ¹	0.015 ²
γ -field	$\alpha=1.2$	$\gamma^*=9.7 \text{ J/m}^2$

¹ mean value

² standard deviation

physically acceptable set of modeling parameters, good agreement was possible for all significant experimental features observed.

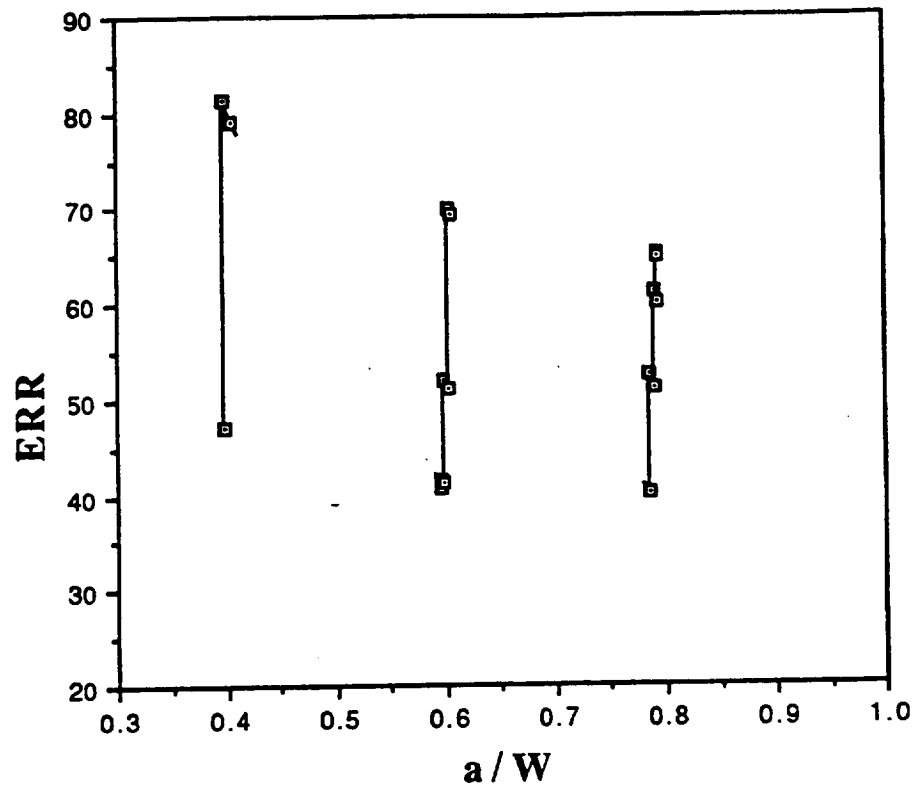


Figure 5.6: Plot of one computer *experiment* showing multiple increments of subcritical crack growth and dynamic initiation simulating experimental observations.

Table 5.2 Summary of Output Parameters

		G_I^a J/mm ²	G_I^i J/mm ²	ℓ μ m	Δx (DYNAMIC) mm
MEAN	experiment	47.	68.	398	4.4
	simulation	48.	68.	385	4.9
STANDARD DEVIATION	experiment	18. %	12. %	42. %	59. %
	simulation	17. %	13. %	36. %	44. %

It is worth noting that other methods for modelling the process of interrupted subcritical crack growth observed for the NC-132 material were considered. The first of these was to assume that fracture toughness was crack growth rate sensitive, and that the specific fracture energy increased with velocity. However, this model cannot explain the process of dynamic initiation and subsequent extension. If stress corrosion activated, a rate sensitive fracture toughness should increase with velocity without the sudden decrease required for dynamic initiation. Another mechanism often employed to explain increases in fracture resistance is interlocking or bridging forces at the crack tip. This model was examined (see Appendix E) and it was determined that the dependency of the apparent ERR within the subcritical crack growth increment is qualitatively different from that observed in the experiment. That is the interlocking forces decrease during subcritical extension which leads to a decrease in the apparent fracture resistance. This behavior is opposite from the modeled behavior of the apparent ERR within a soft inclusion.

As a final consideration, it is possible to obtain a difference in the statistical mean for the critical ERR for dynamic arrest and initiation simply using the SFM theory without modification. The argument may be that the process of arrest 'samples' the maximum values for the specific fracture energy, and the process of initiation 'samples' the minimum values. Such an approach can be used to explain the higher mean value for the initiation ERR, but it cannot predict the size of the dynamic jumps observed, or the noted changes in the surface morphology between slow and fast extension increments since there is no transformation in the actual fracture process.

Only the combination of SFM and a damage zone formation detailed above

captures the essence of the fracture behavior observed for the NC-132 material. Although it cannot be said that the final result for the input parameters is a unique solution for the Crack Propagator, there is reason to believe this since the number of output parameters which agree with experiment exceeds the number of input parameters. Furthermore, the agreement between output parameters and experiment is not taken as proof of the model. However, the procedure used establishes a list of a list input parameters which can now be used to test the SFM model by predicting the fracture performance for a different test configuration.

CHAPTER VI

Conclusions

The review of experimental research in brittle fracture revealed evidence that events of subcritical failure often precede catastrophic fracture for many brittle materials. Fractographic features surrounding failure nucleating flaws in both crystalline and non-crystalline materials exhibit similarities which suggest the existence of a common fracture process. The similarities of these features for several different materials may relate the interdependence between the applied mechanical loads the evolution of a flaw. Strength models currently used to assess material performance are sensitive to the subcritical evolution of flaws which underlines the importance of conducting crack growth studies. Research efforts which identify the resistance mechanisms contributing to subcritical crack growth will advance the predictive capacity of failure models, and this is best accomplished by establishing testing procedures which allow crack growth behavior to be directly observed and accurately quantified.

Many of the obstacles associated with conducting controlled crack growth studies in brittle, high modulus materials are solved with the development of the Stable Poisson Loaded (SPL) specimen. The specimen design and loading technique enables pure Mode I fracture studies to be performed with acceptable standards for engineering accuracy. The problems associated with gripping and grip alignment, which have been inherent

sources of error in brittle testing, are minimized by the novel testing procedure. The SPL specimen and testing procedure has demonstrated its ability to promote controlled propagation of through-thickness cracks in several ceramics.

The detailed experimental fracture study using the modified SPL specimen and the NC-132 material showed that increments of slow crack growth always preceded increments of dynamic crack growth. Slow crack growth increments occurred with an increase in the crack-tip velocities and an increase in fracture resistance. The energy release rate at dynamic initiation was, on the average, 40 percent greater than the average energy release rate required to initiate slow crack growth after each dynamic arrest. Dynamic initiation occurs abruptly, and both dynamic initiation and arrest leave distinct marks on the fracture surface. Fractographic studies reveal a transition in the fracture resistance mechanism between increments of slow and fast crack growth, and slow crack growth produces an increase in fracture surface tortuosity compared to fast growth. The presence of ceramic debris within increments of subcritical growth suggests that either crack bridging or subsurface microcracking are mechanisms contributing to the increase in fracture resistance. The analytical treatment utilizes an approach based on a zone of microcracked material in front of the crack tip as this provides a rational basis for modeling experimental results. It was demonstrated that a single parameter, for example the critical fracture toughness, G_{Ic} , does not characterize the conditions required for propagation instability. Experimental measurements for critical crack lengths, and the energy release rates at dynamic initiation and arrest exhibit significant experimental scatter. Only the combination of Statistical Fracture Mechanics with a damaged zone of

material in front of the crack tip reproduced the essence of the fracture behavior observed for the NC-132 material.

REFERENCES

- Abdel-Latif, A. I. A., R. C. Bradt, and R. E. Tressler. 1977. "Dynamics of Fracture Mirror Boundary Formation in Glass," Int. J. Frac. 13:349-359.
- Abdel-Latif, A. I. A., R. C. Bradt, and R. E. Tressler. 1981. "Multiple-Mist Regions on Glass Fracture Surfaces." In Fractography and Material Science, edited by L. N. Gilbertson and R. D. Zipp, 259-70. Philadelphia, American Society for Testing and Materials.
- Amar, E., G. Gauthier, and J. Lamon. 1989. "Reliability Analysis of a Si_3N_4 Ceramic Piston Pin for Automotive Engines." In Ceramics Materials and Components for Engines, edited by V. Tennery, 1334-46. Westerville, OH: American Ceramic Society.
- American National Standards Institute. 1985. "Surface Texture." ANSI/ASME B46.1. New York: ANSI.
- American Society for Testing and Materials. 1992. "Standard Practice for R-Curve Determination." ASTM E561. Philadelphia: ASTM.
- American Society for Testing and Materials. 1992. "Standard Test Method for Plane-Strain Fracture Toughness of Metallic Materials." ASTM E399. Philadelphia: ASTM.
- Bahat, D., G. Leonard, and A. Rabinovitch. 1982. "Analysis of Symmetric Fracture Mirrors in Glass Bottles." Int. J. Frac. 18:29-38.
- Bansal, G. K., and W. H. Duckworth. 1977. "Fracture Stress as Related to Flaw and Fracture Mirror Sizes." J. Am. Ceram. Soc. 60:304-10.
- Barsoum, R. S. 1974. "On the Use of Isoparametric Finite Elements in Linear Fracture Mechanics." Int. J. Num. Meth. Eng. 10:25-37.
- Batdorf, S. B., and J. G. Crose. 1974. "A Statistical Theory for the Fracture of Brittle Structures Subjected to Nonuniform Stresses." J. of Appl. Mech. 41:459-64.
- Batdorf, S. B., and H. L. Heinisch. 1978. "Weakest Link Theory Reformulated for Arbitrary Fracture Criterion." J. Am. Ceram. Soc. 61:355-58.

- 154 Batdorf, S. B. 1978. "Fundamentals of the Statistical Theory of Fracture." In Fracture Mechanics of Ceramics, v.3, edited by R. C. Bradt, D. P. H. Hasselman, and F. F. Lange, 1-30. New York: Plenum.
- Bolotin, V. V. 1965. Statistical Methods in Structural Mechanics. San Francisco: Holden-Day.
- Boulet, J. M. 1988. "An Assessment of the State of Art in Predicting the Failure of Ceramics." ORNL/Sub/86-57598/1. Oak Ridge, TN: Oak Ridge National Laboratory.
- Chao, L. Y., and D. K. Shetty. 1991. "Reliability Analysis of Structural Ceramics Subjected to Biaxial Flexure." J. Am. Ceram. Soc. 74:333-44.
- Chudnovsky, A., and P. C. Perdikaris. 1983. "On the Scale Effect of Fracture in Concrete." In International Conference - Applications of Statistics and Probability in Soil and Structural Engineering, 407-419. Bologna, Italy: Pitagora Editrice.
- Chudnovsky, A. 1984. "Statistics and Thermodynamics of Fracture." Int. J. Eng. Sci. 22:989-997.
- Chudnovsky, A., and B. Kunin. 1987. "A Probabilistic Model of Brittle Crack Formation." J. App. Phys. 62:4124-29.
- Chudnovsky, A., and B. Kunin. 1989. "On Applications of Probability in Fracture Mechanics." In Computational Mechanics of Probabilistic and Reliability Analysis, Wing K. Liu and Ted Belytschko, eds., 395-416. Lausanne: Washington: Elmepress International.
- Chudnovsky, A., and S. Wu. 1990. "Effect of Crack-Microcracks Interaction on Energy Release Rate." Int. J. Frac. 44:43-56.
- Chudnovsky, A., A. Kim, and C. P. Bosnyak. 1992. "An Energy Analysis of Crack Initiation and Arrest in Epoxy." Int. J. Frac. 55:209-222
- Claussen, N., R. Pabst, and C. P. Lahmann. 1975. "Influence of Microstructure of Al_2O_3 and ZrO_2 on K_{Ic} ." Proc. Brit. Cer. Soc. 25:139-49.
- Cooke, R. G. 1982. "Microstructure and Failure Probability of Coarse Structural Ceramics." Proc. Brit. Cer. Soc. 32:171-80.
- Dauskardt, R. H., W. Yu, and R. O. Ritchie. 1987. "Fatigue Crack Propagation in Transformation-Toughened Zirconia Ceramic." J. Am. Ceram. Soc. 70:C248-C252

Dauskardt, R.H., F. Haubensak, and R. O. Ritchie. 1990. "On The Interpretation of Fractal Character and Fracture Profiles." Acta Met. Matl., 38:143-59

Davidge, R. W. 1980. "Combination of Fracture Mechanics, Probability, and Micromechanical Models of Growth in Ceramic Systems." Metal Sci. 14:459-62.

Depoorter, G. L., T. K. Brog, and M. J. Readey. 1990. "Structural Ceramics." In Metals Handbook, 10th ed., v.2. 1021, table 2. Materials Park, OH: ASM International. Dukes, W. H. 1975. "Brittle Materials: A Design Challenge." Mech. Eng. 97:42-47.

Easler, T. E., R. C. Bradt, and R. E. Tressler. 1981. "Concurrent Flaw Populations in SiC." J. Am. Ceram. Soc. 64:C53-55.

Evans, A. G., and T. G. Langdon. 1976. "Structural Ceramics." Prog. Mat. Sci. 21:171-441.

Evans, A. G., D. R. Biswas, and R. M. Fulrath. 1979. "Some Effects of Cavities on the Fracture of Ceramics: I. Cylindrical Cavities." J. Am. Ceram. Soc. 62:101-106.

Evans, A. G. 1974. "Fracture Mechanics Determinations for Ceramics." In Fracture Mechanics of Ceramics, R. C. Bradt, D. P. H. Hasselman, and F. F. Lange, eds., 17-48. New York: Plenum.

Faber, K. T., and A. G. Evans. 1983. "Crack Deflection Processes: II, Experiment," Acta Met. 31:577-584.

Field, J. E. 1971. "Brittle Fracture: Its Study and Application." Contemp. Phys. 12:1-31.

Freudenthal, A. M. 1969. "Statistical Approach to Brittle Fracture." In Fracture, v.2, edited by H. Leibowitz, 591-619. New York: Academic.

Freiman, S. W., A. G. Gonzalez, and J. J. Mecholsky. 1979. "Mixed-Mode Fracture in Soda-Lime Glass." J. Am. Ceram. Soc. 62:206-8.

Gee, M. G., and R. Morrell. 1986. "Fracture Mechanics and Microstructures of Ceramics." In Fracture Mechanics of Ceramics 8, edited by R. C. Bradt, A. G. Evans, D. P. H. Hasselman, and F. F. Lange, 1-22. New York: Plenum.

Ghosn, L., A. M. Calomino, and D. N. Brewer. 1992. "Numerical Calibration of the Stable Poisson Loaded Specimen," NASA TM-105609. Cleveland, OH: NASA Lewis Research Center.

- Ghosn, L. 1990. Private Communications. Sverdrup Corporation, NASA Lewis Research Center, Cleveland, OH
- Godfrey, D. J., and M. W. Lindey. 1973. "Strength of reaction-bonded silicon nitride ceramics." Proc. Brit. Cer. Soc. 22:229-52.
- Govila, R. K, P. Beardmore, and K. R. Kinsman. 1981. "Strength Characterization and Nature of Crack Propagation in Ceramic Materials." Fractography and Materials Science, edited by N. Gilbertson and R. D. Zipp, 225-245. Philadelphia: American Society for Testing and Materials.
- Griffith, A. A. 1921. "The Phenomena of Rupture and Flow in Solids." Phil. Trans. R. Soc. London, Ser. A 221:163-198.
- Gyekenyesi, J. P. 1986. "SCARE: A Postprocessor Program to MSC/NASTRAN for Reliability Analysis of Structural Ceramic Components." J. Eng. Gas Turb. 108:540-546.
- Hanney, M. J., and R. Morrell. 1982. "Factors Influencing the Strength of a 95% Alumina Ceramic," Proc. Brit. Cer. Soc. 32:277-290.
- Haritos, G. K., J. W. Hager, A. K. Amos, and M. J. Salkind. 1988. "Mesomechanics: The Microstructure-Mechanics Connection." Int. J. Sol. Struc. 24:1081-1089, 1091-1096.
- Healy, J. T., and J. J. Mecholsky. "Scanning Electron Microscopy Techniques and Their Application to Failure Analysis of Brittle Materials." In Fractography of Ceramic and Metal Failures, edited by J. J. Mecholsky, Jr., and S. R. Powell, Jr., 157-181. Philadelphia: American Society for Testing and Materials.
- Helms, P.E., P. W. Heitman, L. C. Lindgren, and S. R. Thrasher. 1984. "Ceramic Applications in Turbine Engines." NASA CR-174715. Cleveland, OH: NASA Lewis Research Center.
- Hull, D. R., T. A. Leonhardt, and W. A. Sanders. 1991. "Plasma Etching a Ceramic Composite," NASA TM-105430. Cleveland, OH: NASA Lewis Research Center.
- Irwin, J. R. 1948. "Fracture Dynamics." In Fracture of Metals. Metals Park, OH: American Society for Metals.
- Johnson, J. W., and D. G. Holloway. 1968. "Microstructure of the Mist Zone on Glass Fracture Surfaces." Philos. Mag. 8S.17:899-910.
- Johnson, C. A., and W. T. Tucker. 1985. "Advanced Statistical Concepts of Fracture in Brittle Materials," General Electric Corp. Report.

Johnson, J. W., and D. G. Holloway. "Shape and Size of the Fracture Zones on Glass Fracture Surfaces." Philos. Mag. 14:731-743.

Kanninen, M. F., and C. H. Popelar. 1985. Advanced Fracture Mechanics. New York: Oxford University.

Kirchner, H. P., and R. M. Gruver. 1974. "Fracture Mirrors." In Fracture Mechanics of Ceramics, v.2, edited by R. C. Bradt, D. P. H. Hasselman, and F. F. Lange, New York: Plenum.

Kirchner, H. P., and J. W. Kirchner. 1979. "Fracture Mechanics of Fracture Mirrors." J. Am. Ceram. Soc. 62:198-201.

Krohn, D.A., and D. P. H. Hasselman. 1971. "Relation of Flaw Size to Mirror in the Fracture of Glass." J. Am. Ceram. Soc. 54:411.

Kunin B., and M. Gorelik. 1991. "On Representation of Fracture Profiles by Fractional Integrals of a Wiener Process." J. Appl. Phys. 70:7651-7653.

Lawn, B. R., and T. R. Wilshaw. 1974. Fracture of Brittle Solids. Cambridge, MA: Cambridge Univ.

Leadbetter, M. R., G. Lindgren, and H. Rootzen. 1983. Extremes and Related Properties of Random Sequences and Processes. New York: Springer-Verlag.

Lewis, D. 1981. "Fracture Strength and Mirror Size in a Commercial Glass-Ceramic." J. Am. Ceram. Soc. 64:82-6.

Li, R., and A. Chudnovsky. 1993. "Variation of the Energy Release Rate as a Crack Approaches and Passes Through an Elastic Inclusion." To be published, contact A. Chudnovsky. University of Illinois at Chicago.

Mandelbrot, B.B. 1982. The Fractal Geometry of Nature. W. H. Freeman and Co., San Francisco

Mandelbrot, B.B., D.E. Passoja, and A.J. Pullay.(1984). "Fractal Character of Fracture Surfaces of Metals." Nature. 308.721-22

MARC General Purpose Finite Element Program. Version K.4. Palo Alto, CA: MARC Analysis Research Corporation.

Margetson, J. 1976. "Statistical Theory of Brittle Failure for an Anisotropic Structure Subjected to a Multiaxial Stress State. AIAA Paper 76-632. New York: American Institute of Aeronautics and Astronautics.

Maugis, D. 1986. "Sub-Critical Crack Growth, Surface Energy and Fracture Toughness of Brittle Materials." In Fracture Mechanics of Ceramics 8, edited by R. C. Bradt, A. G. Evans, D. P. H. Hasselman, and F. F. Lange, 255-72. New York: Plenum.

McKinney, K. R., B. A. Bender, R. W. Rice, and C. CM. Wu. 1991. "Slow Crack Growth in Si_3N_4 at Room Temperature." J. Mat. Sci. 26:6467-72.

Mecholsky, J. J., R. W. Rice, and S. W. Freiman. 1974. "Prediction of Fracture Energy and Flaw Size in Glasses from Measurements of Mirror Size." J. Am. Ceram. Soc. 57:440-43.

Mecholsky, J. J., S. W. Freiman, and R. W. Rice. 1976. "Fracture Surface Analysis of Ceramics." J. Mat. Sci. 11:1310-19.

Mecholsky, J. J., A. C. Gonzalez, and S. W. Freiman. 1979. "Fractography Analysis of Delayed Failure in Soda-Lime Glass." J. Am. Ceram. Soc. 62:577-80.

Mecholsky, J. J., and S. W. Freiman. 1981(A). "Fractographic Analysis of Delayed Failure in Ceramics." In Fractography and Materials Science, edited by L. N. Gilbertson and R.D. Zipp, 246-58. Philadelphia: American Society for Testing and Materials.

Mecholsky, J. J. 1981(B). "Intergranular Slow Crack Growth in MgF_2 ." J. Am. Ceram. Soc. 64:563-66.

Mecholsky, J. J. 1981(C). "Application of Scanning Electron Microscopy to Failure Analysis in Ceramics and Glasses." SAND-81-0063C. Albuquerque, NM: Sandia National Laboratories.

Mecholsky, J.J., D.E. Passoja, and K.S. Feinberg-Ringel. 1989. "Quantitative Analysis of Brittle Fracture Surfaces Using Fractal Geometry." J. Am. Ceram. Soc., 72:60-5

Mull, M. A., A. Chudnovsky, and A. Moet. 1987. "A Probabilistic Approach to the Brittle Fracture Toughness of Composites." Philos. Mag. A 56:419-43.

Munz, D., R. T. Bubsey, and J. E. Srawley. 1982. "Compliance and Stress Intensity Coefficients for Short Bar Specimens with Chevron Notches." Int. J. Frac. 16:359-74.

Mutuh, Y., M. Takahashi, and A. Kanagawa. 1992. "Fatigue Crack Growth Behavior of Surface Cracks in Silicon Nitride." Submitted to the Symposium on Cyclic Deformation, Fracture, and Nondestructive Evaluation of Advanced Materials. Philadelphia: American Society for Testing and Materials.

Nakayama, J. 1965. "Direct Measurement of Fracture Energies of Brittle Heterogeneous Materials." J. Am. Ceram. Soc. 48:583-87.

Newman, J. C. 1984. "A Review of Chevron-Notched Fracture Specimens." In Chevron-Notched Specimens Testing and Stress Analysis, edited by J. H. Underwood, S. W. Freiman, and F. I. Bratta, 5-31. Philadelphia: American Society for Testing and Materials.

Nose, T., and T. Fujii. 1988. "Evaluation of Fracture Toughness for Ceramic Materials by Single-Edge-Precracked-Beam Method." J. Am. Ceram. Soc. 71:328-33.

Passmore, E. M., R. M. Spriggs, and T. Vasitos. 1965. "Strength-Grain Size-Porosity Relations in Al_2O_3 ." J. Am. Ceram. Soc. 48:1-7.

Pierce, F. T. 1921. "Tensile Tests for Cotton Yarns in The Weakest Link - Theorems on the Strength of Long and of Composite Systems." J. Text. Inst. 17.

Prasad, N. E., and S. B. Bhaduri. 1988. "Subcritical Growth of Long Cracks in Heterogeneous Ceramics." J. Mat. Sci. 23:2167-73.

Quinn, G. D., and J. B. Quinn. 1983. "Slow Crack Growth in Hot-Pressed Silicon Nitride." In Fracture Mechanics of Ceramics 6, edited by R.C. Bradt, A.G. Evans, D.P.H. Hasselman, and F.F. Lange, 603-36. New York: Plenum.

Quinn, G. D. 1990. "Flexure Strength of Advanced Structural Ceramics - A Round Robin." J. Am. Ceram. Soc. 73:2374-84.

Quinn, G. D. 1991. "Design Data for Engineering Ceramics: A Review of the Flexure Test." J. Am. Ceram. Soc. 43:2037-66.

Rice, R. W., and P. F. Becher. 1977. "Comment on "Creep Deformation of 0 o Sapphire." J. Am. Ceram. Soc. 60:186-188.

Rice, R. W. 1979. "The Difference in Mirror-to-Flaw Size Ratios Between Dense Glasses and Polycrystals." J. Am. Ceram. Soc. 62:533-35.

- Rice, R. W., S. W. Freiman, and P. F. Becher. 1981. "Grain-Size Dependence of Fracture Energy in Ceramics." J. Am. Ceram. Soc. 64:345-54.
- Rice, R. W. 1984(A). "Ceramic Fracture Features, Observations, Mechanisms, and Uses." In Fractography of Ceramic and Metal Fractures, edited by J. J. Mecholsky, Jr., and S. R. Powell, Jr., 5-103. Philadelphia: American Society for Testing and Materials.
- Rice, R. W. 1984(B). "Pores as Fracture Origins in Ceramics." J. Mat. Sci. 19:895-914.
- Salem, J., and J. Shannon. 1987. "Fracture Toughness of Si_3N_4 Measured with Short Bar Chevron-Notch Specimens." J. Mat. Sci. 22:321-24.
- Shetty, D.K., G. K. Bansal, A. R. Rosenfield, and W. H. Duckworth. 1980. "Criterion for Fracture Mirror Boundary Formation in Ceramics." J. Am. Ceram. Soc. 63:106-8.
- Shetty, D. K., A. R. Rosenfield, and W. H. Duckworth. 1983. "Biaxial Stress State Effects on Strengths of Ceramics Failing from Pores." In Fracture Mechanics of Ceramics 5, edited by R. C. Bradt, D. P. H. Hasselman, and F. F. Lange, 531-42. New York: Plenum.
- Shih, T. T. 1980. "An Evaluation of the Probabilistic Approach to Brittle Design," Int. J. Eng. Frac. Mech. 13:257-71.
- Suresh, S., and J. R. Brockenbrough. 1988. "Theory and Experiments for Fracture in Cyclic Compression: Single Phase Ceramics and Ceramic Composites." Acta. Met. 36:1455-70.
- Swank, L. R., and R. M. Williams. 1981. "Predicting Reliability of Ceramic Turbine Components." Cer. Bull. 60:830-.
- Tada, H., P. C. Paris, and G. R. Irwin. 1985. The Stress Analysis of Cracks Handbook. St. Louis, MO: Paris Productions.
- Tappin, G., R. W. Davidge, and J. R. McLaren. 1978. "The Strength of Ceramics Under Biaxial Stresses." In Fracture Mechanics of Ceramics 3, edited by R. C. Bradt, D. P. H. Hasselman, and F. F. Lange, 435-49. New York: Plenum.
- Tattersall, H.G., and G. Tappan. 1966. "The Work of Fracture and Its Measurement in Metals, Ceramics and Other Materials." J. Mat. Sci. 1:296-301.
- Weibull, A. 1951. "A Statistical Distribution Function of Wide Applicability." J. Appl. Mech. 18:293-97.

Weil, N. A., and I. M. Daniel. 1964. "Analysis of Fracture Probabilities in Nonuniformly Stressed Brittle Materials." J. Am. Ceram. Soc. 47:268-74.

Wiederhorn, S. M., and H. Johnson. 1973. "Effect of Electrolyte pH on Crack Propagation in Glass." J. Am. Ceram. Soc. 56:192-97.

Wiederhorn, S. M., A. G. Evans, and D. E. Roberts. 1974(A). "A Fracture Mechanics Study of the Skylab Windows." In Fracture Mechanics of Ceramics 5, edited by R. C. Bradt, A. G. Evans, D. P. H. Hasselman, and F. F. Lange, 829-42. New York: Plenum.

Wiederhorn, S. M. 1974(B). "Subcritical Crack Growth." In Fracture Mechanics of Ceramics 2, edited by R. C. Bradt, A. G. Evans, D. P. H. Hasselman, and F. F. Lange, 613-46. New York: Plenum.

Wiederhorn S. M. 1983. "A Probabilistic Framework for Structural Design." In Fracture Mechanics of Ceramics 6, edited by R. C. Bradt, A. G. Evans, D. P. H. Hasselman, and F. F. Lange, 297-336. New York: Plenum.

Weiderhorn, S.M. 1969. "Fracture Surface Energy of Glass,"J. Am. Ceram. Soc., 57.99-105

APPENDIX A

Crack Growth Kinetics

Many ceramics, particularly those with oxide glasses at their grain boundary, exhibit a loss in strength with time under load. This behavior is termed static fatigue or delayed failure and it is usually associated with the subcritical extension of cracks due to stress corrosion. The lifetime of ceramics that exhibit static fatigue depends on the environment surrounding the crack and the applied stress intensity. The empirical relationship that is often used to model the kinetics of crack growth takes the form of a power law given in equation A.1.

$$V = V_o \left(\frac{K_I}{K_o} \right)^n = AK_I^n \quad \text{A.1}$$

Here V is the crack front velocity at a given applied stress intensity level and V_o and n are experimentally determined constants. The stress intensity factor K_o is a normalizing factor taken as unity. This expression can be combined with equation 2.6 to calculate the time to failure under a specific load, σ_a , as

$$t_f = \int_{c_{init}}^{c_{crit}} \delta \frac{c}{V} = \int_{c_{init}}^{c_{crit}} \delta \frac{c}{AK_I^n} = \int_{c_{init}}^{c_{crit}} \frac{1}{A} \left(\frac{\sigma_a \sqrt{1.2\pi}}{\phi} \right)^{-n} C^{-\frac{n}{2}} \quad \text{A.2}$$

integration yields the expression

$$t_f = \frac{1}{A} \left(\frac{\sigma_a \sqrt{1.2\pi}}{\phi} \right)^{-n} \left(\frac{2}{n-2} \right) \left[C_{init}^{\left(\frac{2-n}{2}\right)} - C_{crit}^{\left(\frac{2-n}{2}\right)} \right] \quad A.3$$

The value c_{crit} is the critical flaw size and c_{init} is the estimated size of the failure nucleating flaw. Since measured values of n are large (often greater than 50 for room temperature) $C_{crit}^{\left(\frac{2-n}{2}\right)} \ll C_{init}^{\left(\frac{2-n}{2}\right)}$, and the time to failure is approximated as

$$t_f = \frac{2}{A(n-2)} \left[\left(\frac{1.2\pi c_{init}}{\phi} \right)^{\frac{1}{2}} \sigma_a \right]^{-n} c_{init} \quad A.4$$

One can see that errors in lifetime increase rapidly with the uncertainty in either the initiating crack length, C_{init} , or the crack shape, ϕ , both of which are unknown. A simple analysis can be used to demonstrate how quickly errors multiply by assigning $K_I^* = K_I(1+\epsilon)$ and substituting into equation A.1, thus

$$V = AK_I(1\pm\epsilon)^n \quad A.5$$

and since $(1\pm\epsilon) \approx 1\pm n\epsilon$, the error in the velocity estimate becomes

$$\Delta V \approx AK_I^n \cdot n\epsilon = V(n\epsilon) \quad A.6$$

Obviously, unless K_I is known accurately, that is, c_{init} and ϕ , estimations for lifetime using the kinetics model proposed are likely to be of little use. For a value of $n=50$, an error of only $\epsilon=0.10$ can produce velocity predictions which are in error by 500 percent.

APPENDIX B

Material Processing and Microstructure information

The new material (batch identification 166481#1) was manufactured in 25x150x150 mm billets with the hot pressing direction parallel to the 25 mm thickness. The manufacturer reports nominal values for Young's modulus and Poisson's ratio as 310 GPa and 0.28, respectively. The results of a chemical analysis for the powder lot are given in table B.1. A chemical analysis of the processed material revealed similar results. The alpha silicon nitride content of the starting powder was 94.1 percent. The silicon nitride powder was hot pressed at a temperature of 1780 °C and a pressure of 21 Mpa. The fired density of the material was 3.22 grams/cc. Samples of the material

Table B.1 Chemical Analysis of Powder

ELEMENT	% WEIGHT
Fe	0.095
Al	0.089
Ca	0.021
Mg	0.550
W	1.850
O	2.520

were polished and etched for microstructural analysis. Metallographic samples were cut such that the polished surface would have the same plane normal as the fracture surface. Polished samples were etched using two methods: plasma etching using $\text{CF}_4 + 4\% \text{O}_2$ gas and molten salt using potassium hydroxide (Hull,1991). Because NC-132 is a fine grained material with very little glass content it was difficult to obtain clearly identified

grain boundaries. The molten salt technique proved to be altogether unsuccessful. Although better results were obtained by plasma etching, grain boundaries were still difficult to identify. Micrographs of a plasma etched sample using the a scanning electron microscope (SEM) are given in figures B.1(a) and B.1(b) for an etch time of 30 seconds and figure B.2(a) and B.2(b) for a 180 second etch time. The YZ modulated SEM image is a plot of contrasts relating to elevation changes on the etched surface. Both the short and long etch times yield faint grain boundaries which are difficult to distinguish. Replication of the 30-second etched surface using an acetate film provided the best results for SEM studies of microstructure and micrographs of the SEM images taken from the replica are displayed in figures B.3(a) and B.3(b). Examination of the replicas from the 30-second etched sample supported the manufacturer's grain size analysis report that maximum grain size is less than $1.5\ \mu\text{m}$ and the average grain size was less than $1.0\ \mu\text{m}$. Fractography studies of the fracture surfaces also correlated with these results for grain size (see Chapter IV).

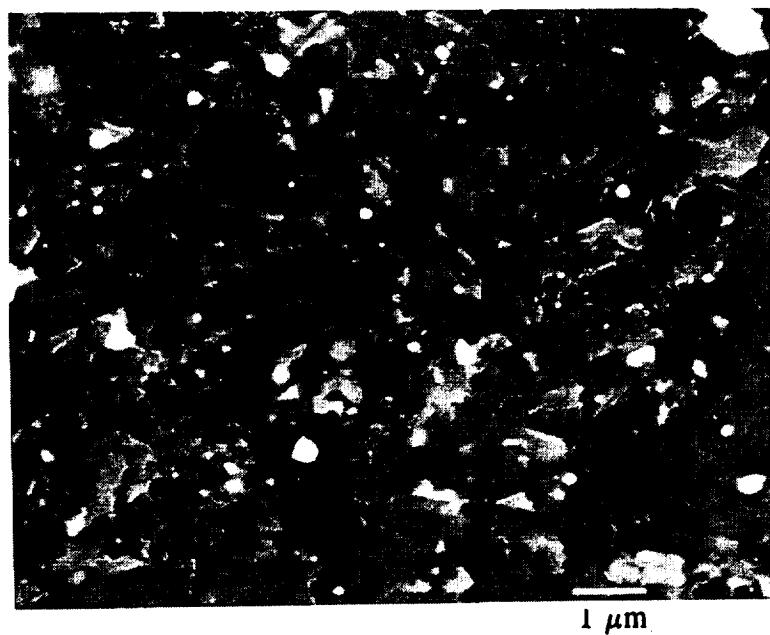


Figure B.1(a): Secondary electron SEM micrographs of NC-132 microstructure using a plasma etching technique for 30 seconds.



Figure B.1(b): SEM micrograph of YZ image taken from the 30-second plasma etched microstructural sample displayed in figure B1.(a).

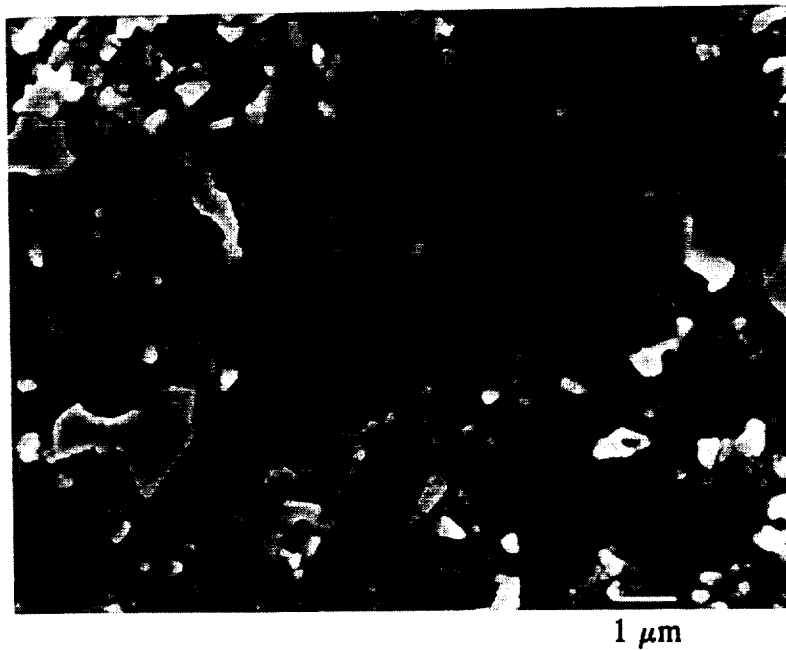


Figure B.2(a): Secondary electron SEM micrograph of NC-132 microstructure using a plasma etching technique for 180 seconds.

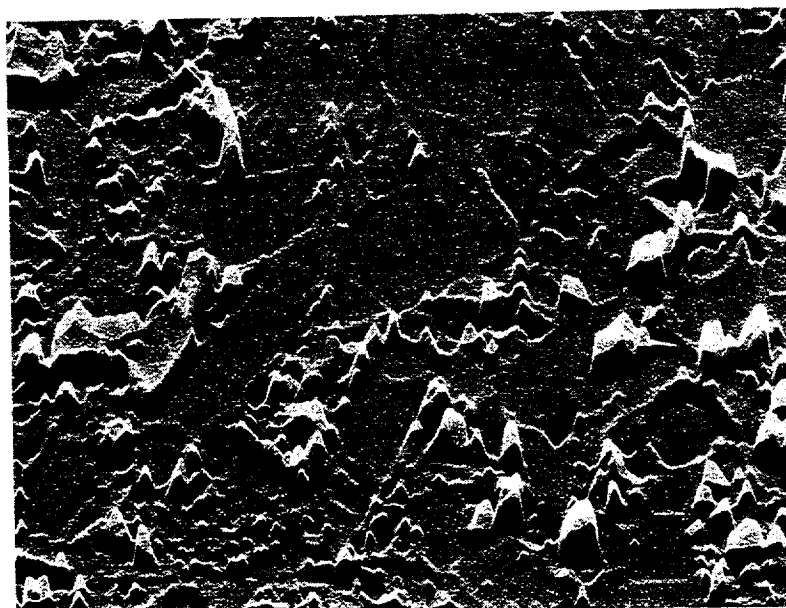


Figure B.2(b): SEM micrograph of YZ image taken from the 180-second plasma etched microstructural sample displayed in figure B1.(a).

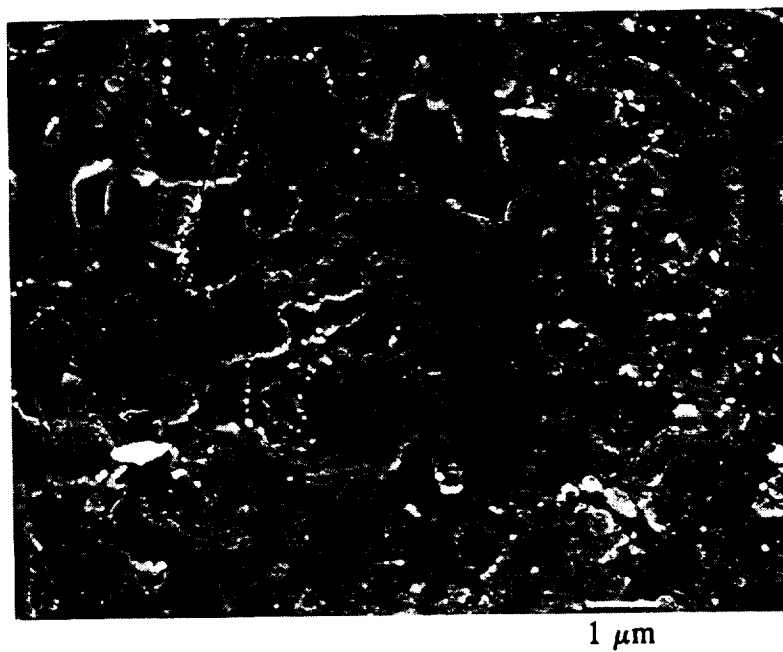


Figure B.3(a): Secondary electron SEM micrograph of acetate replica taken off a 30-second plasma etched sample showing grain boundaries and sizes which are generally less than 1.5 μm.

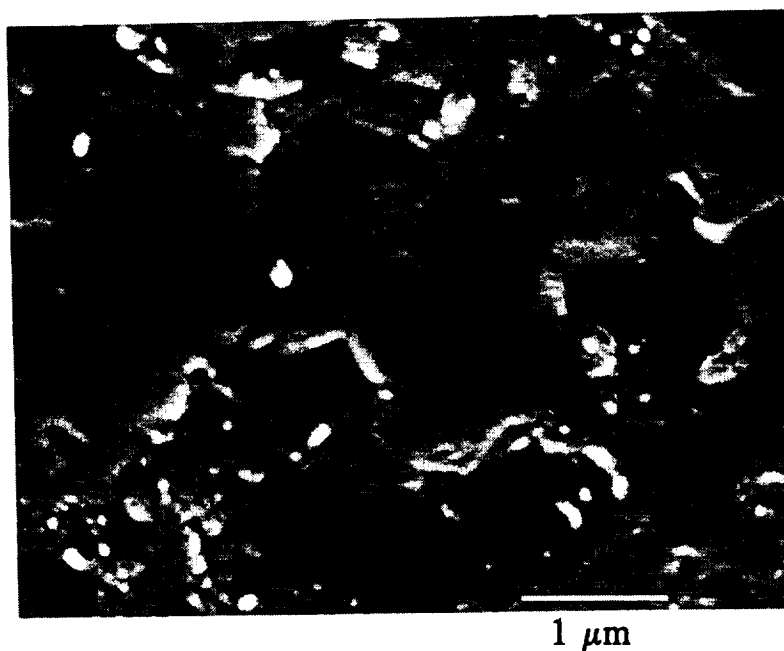


Figure B.3(b): Higher magnification SEM micrograph of acetate replica shown in figure B3.(a).

APPENDIX C

Stress Wave Interaction

A simple dynamic treatment was used to estimate an interaction envelope for stress reflections. It is expected that reflections from the back face provided for the minimum return time for a reflected wave at the crack tip. Interference will not occur if the crack's propagation time is less than the stress wave's return time, or, assuming that the crack tip propagates at some percentage of the stress wave speed, $v_c = \alpha c$, the relationship can be expressed as

$$\frac{\Delta a}{W} \cdot \frac{1}{\alpha c} < \left[2 \left(1 - \frac{a}{W} \right) - \frac{\Delta a}{W} \right] \cdot \frac{1}{c}. \quad C.1$$

The maximum size of the arrested crack, $\left(\frac{a}{W} \right)_{new} = \left(\frac{a}{W} \right)_{old} + \frac{\Delta a}{W}$, is

$$\left(\frac{a}{W} \right)_{new} = \frac{2\alpha}{1+\alpha} \left[1 - \left(\frac{a}{W} \right)_{old} \right] + \frac{a}{W_{old}}. \quad C.2$$

A similar treatment shows that crack tip interaction with stress waves reflected from the free side edges of the specimen will not occur unless the jump increment, $\frac{\Delta a}{W}$, exceeds the size where 'h' is the specimen height (45 millimeters). However, a simple

$$\frac{\Delta a}{W} = \alpha \frac{h}{W} \quad C.3$$

examination would show that waves returning from the side edges require more time than

those returning from the backface. Experimental data were examined for backface stress wave interference by plotting the crack tip positions at initiation versus the succeeding arrest position as shown in figure C.1. The interference region for backface wave returns shown as the hatched section was generated assuming that the dynamic crack speed is half of the stress wave speed, $v_c = 0.5\alpha c$ (Kanninen and Popelar, 1985). All of the crack arrest data taken for both specimens fall well outside the interference zone indicating that arrest was not influenced by stresses reflected from free surfaces.

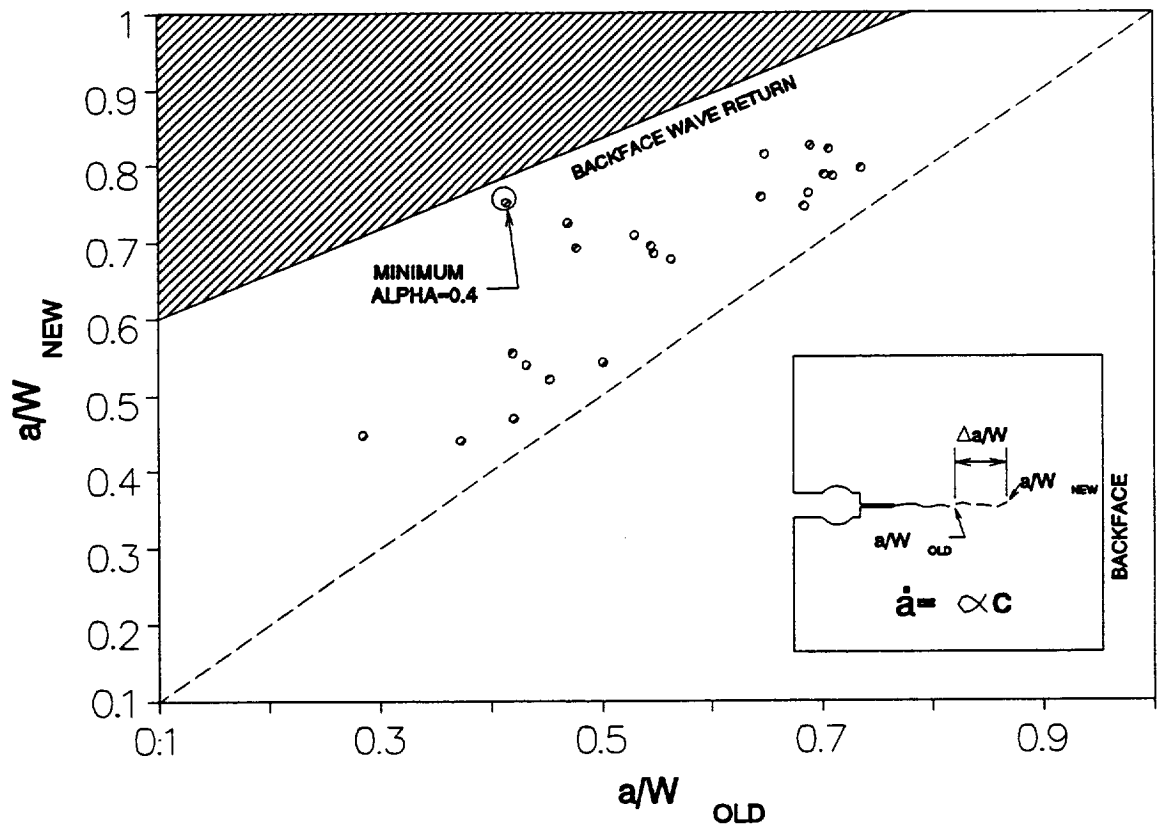


Figure C1: Plot of backface stress wave reflection interaction with propagating crack tip displaying an interaction envelop for energy input at arrest.

APPENDIX D

Replicated Fracture Surface for 3 mm Sample

Fracture debris generated within the second subcritical crack growth band of the 3 mm sample 920130 was examined by replication. Scanning electron micrographs were taken from the fracture surface after coating the sample with chrome but before replication for reference. After replicating, the same areas on the fracture surface were re-examined and comparative micrographs taken. Three areas within each slow growth region were imaged in this manner and the sequence of these micrographs for the 3 mm sample are given in figures D.2 through D.4. Figure D.1 is a low magnification SEM image which shows the relative location of the three higher magnification areas.

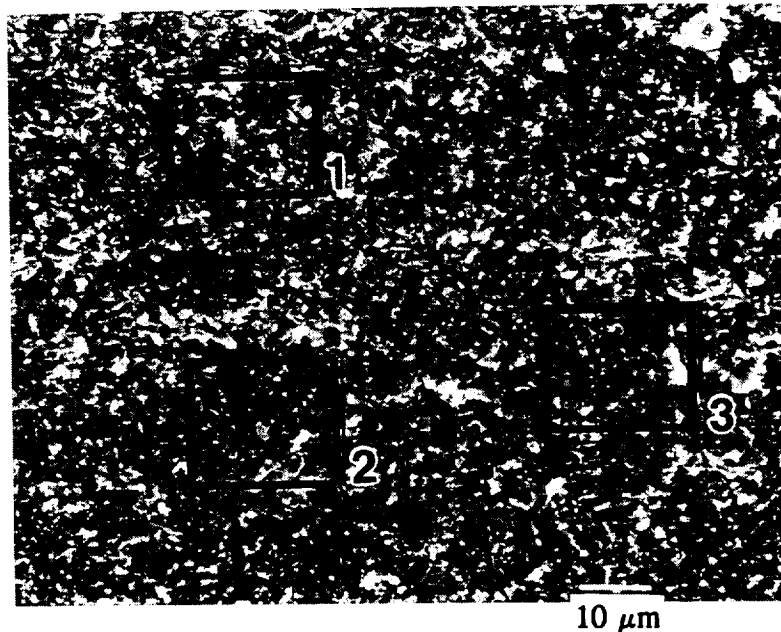


Figure D.1: Low magnification reference micrograph taken before replication showing the relative location of the three higher magnification micrographs in figures D.2 through D.4

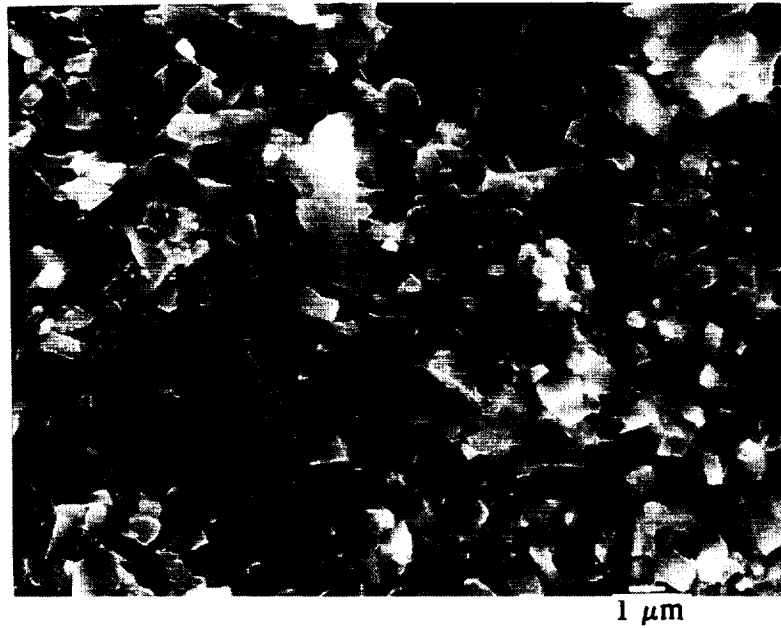


Figure D.2(a): Secondary electron SEM micrographs of Region 1 taken before replication.



Figure D.2(b): Micrograph of Region 1 taken after replication.

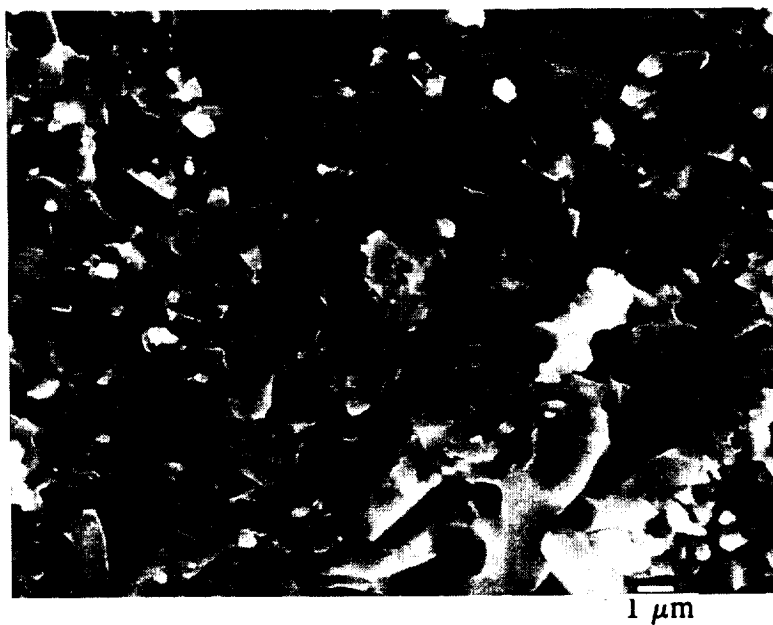


Figure D.3(a): Secondary electron SEM micrograph of Region 2 before replication.



Figure D.3(b): Secondary electron SEM micrograph of Region 2 image taken after replication.



Figure D.4(a): Secondary electron SEM micrograph of Region 3 taken before replication.



Figure D.4(b): Secondary electron SEM micrograph of Region 3 taken after replicating.

APPENDIX E

Effect of Interlocking Stress as Damage Zone Mechanism

Traction forces acting across the crack face at the crack tip is a mechanism which is often used to model experimentally observed increases in fracture resistance. However, the ERR for such a configuration does not produce the characteristic response needed to model experimental results. This can be shown by considering an edge cracked semi-infinite specimen subjected to a point load at the crack face as shown in figure E.1. The damage zone is modeled as an extension of the crack tip with an

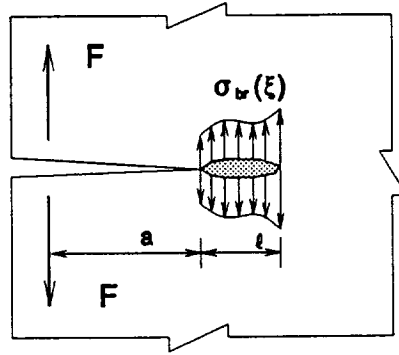


Figure E.1: Single-edged crack in a semi-infinite plane loaded under a pair of point forces, F , and an arbitrary crack tip bridging stress $\sigma_{br}(x)$.

arbitrarily distributed bridging stress $\sigma_{br}(\xi)$. The crack driving forces can be evaluated from Gibb's potential, Π , for this system

$$\Pi = \int_0^a \frac{F^2}{E} k^2(x) dx - \int_a^{a+l} \frac{1}{E} \left\{ \int_a^x [\sigma_{br}(\xi) k(x-\xi)]^2 d\xi \right\} dx \quad \text{E.1}$$

where $k(x) = \frac{2 \times 1.12}{\sqrt{2\pi x}}$ is the Green's function for the stress intensity factor of an edge crack in a semi-infinite plane. The crack driving force, i.e., the energy release rate (ERR), is derived by taking the derivative of Gibb's potential with respect to a , $\frac{d\Pi}{da}|_{(a+\ell)=const}$, such that

$$G_I = \frac{4\sigma_{br}(\ell)}{\pi E} \int_a^{a+\ell} \frac{1}{\sqrt{x-a}} \left[\frac{F}{\sqrt{x}} - \int_a^x \frac{\sigma_{br}(\xi)}{\sqrt{x-\xi}} d\xi \right] dx \quad \text{E.2}$$

It is obvious from the expression for the ERR that, provided $\sigma_{br}(\xi)$ is a non singular distribution of stresses along the damage zone, $G_I(a, \ell)$ will have the qualitative shape given in figure E.2.

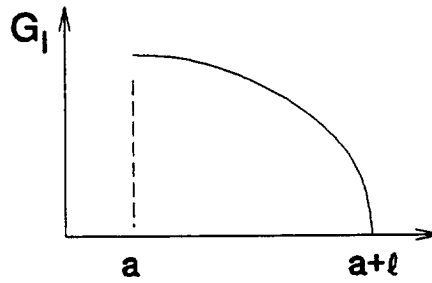


Figure E.2: Characteristic behavior in the apparent energy release rate for a crack face bridging stress.

REPORT DOCUMENTATION PAGE			Form Approved OMB No. 0704-0188	
Public reporting burden for this collection of information is estimated to average 1 hour per response, including the time for reviewing instructions, searching existing data sources, gathering and maintaining the data needed, and completing and reviewing the collection of information. Send comments regarding this burden estimate or any other aspect of this collection of information, including suggestions for reducing this burden, to Washington Headquarters Services, Directorate for Information Operations and Reports, 1215 Jefferson Davis Highway, Suite 1204, Arlington, VA 22202-4302, and to the Office of Management and Budget, Paperwork Reduction Project (0704-0188), Washington, DC 20503.				
1. AGENCY USE ONLY (Leave blank)		2. REPORT DATE May 1994	3. REPORT TYPE AND DATES COVERED Technical Memorandum	
4. TITLE AND SUBTITLE Damage Mechanisms and Controlled Crack Propagation in a Hot Pressed Silicon Nitride Ceramic			5. FUNDING NUMBERS WU-505-63-52	
6. AUTHOR(S) Anthony M. Calomino				
7. PERFORMING ORGANIZATION NAME(S) AND ADDRESS(ES) National Aeronautics and Space Administration Lewis Research Center Cleveland, Ohio 44135-3191			8. PERFORMING ORGANIZATION REPORT NUMBER E-8867	
9. SPONSORING/MONITORING AGENCY NAME(S) AND ADDRESS(ES) National Aeronautics and Space Administration Washington, D.C. 20546-0001			10. SPONSORING/MONITORING AGENCY REPORT NUMBER NASA TM-106595	
11. SUPPLEMENTARY NOTES This report was submitted as a dissertation in partial fulfillment of the requirements for the degree Doctor of Philosophy to Northwestern University, Evanston, Illinois, December 1993. Responsible person, Anthony M. Calomino, organization code 5220, (216) 433-3311.				
12a. DISTRIBUTION/AVAILABILITY STATEMENT Unclassified - Unlimited Subject Category 27			12b. DISTRIBUTION CODE	
13. ABSTRACT (Maximum 200 words) The subcritical growth of cracks from pre-existing flaws in ceramics can severely affect the structural reliability of a material. The ability to directly observe subcritical crack growth and rigorously analyze its influence on fracture behavior is important for an accurate assessment of material performance. A Mode I fracture specimen and loading method has been developed which permits the observation of stable, subcritical crack extension in monolithic and toughened ceramics. The test specimen and procedure has demonstrated its ability to generate and stably propagate sharp, through-thickness cracks in brittle high modulus materials. Crack growth for an aluminum oxide ceramic was observed to be continuously stable throughout testing. Conversely, the fracture behavior of a silicon nitride ceramic exhibited crack growth as a series of subcritical extensions which are interrupted by dynamic propagation. Dynamic initiation and arrest fracture resistance measurements for the silicon nitride averaged 67 and 48 J/m ² , respectively. The dynamic initiation event was observed to be sudden and explosive. Increments of subcritical crack growth contributed to an 40 percent increase in fracture resistance before dynamic initiation. Subcritical crack growth visibly marked the fracture surface with an increase in surface roughness. increments of subcritical crack growth loosen ceramic material near the fracture surface and the fracture debris is easily removed by a replication technique. Fracture debris is viewed as evidence that both crack bridging and subsurface microcracking may be some of the mechanisms contributing to the increase in fracture resistance. A Statistical Fracture Mechanics model specifically developed to address subcritical crack growth and fracture reliability is used together with a damaged zone of material at the crack tip to model experimental results. A Monte Carlo simulation of the actual experiments was used to establish a set of modeling input parameters. It was demonstrated that a single critical parameter does not characterize the conditions required for dynamic initiation. Experimental measurements for critical crack lengths, and the energy release rates exhibit significant scatter. The resulting output of the model produces good agreement with both the average values and scatter of experimental measurements.				
14. SUBJECT TERMS R-Curve; Fracture; Silicon nitride; Subcritical; Damage			15. NUMBER OF PAGES 194	
			16. PRICE CODE A09	
17. SECURITY CLASSIFICATION OF REPORT Unclassified	18. SECURITY CLASSIFICATION OF THIS PAGE Unclassified	19. SECURITY CLASSIFICATION OF ABSTRACT Unclassified	20. LIMITATION OF ABSTRACT	

**National Aeronautics and
Space Administration
Lewis Research Center
21000 Brookpark Rd.
Cleveland, OH 44135-3191**

**Official Business
Penalty for Private Use \$300**

POSTMASTER: If Undeliverable — Do Not Return

